

DEVELOPING ADVANCED METHODS FOR ANALYSIS AND
INVERSION OF MARINE ELECTROMAGNETIC DATA IN
OFF-SHORE EXPLORATION

by

Dae Ung Yoon

A dissertation submitted to the faculty of
The University of Utah
in partial fulfillment of the requirements for the degree of

Doctor of Philosophy

in

Geophysics

Department of Geology and Geophysics

The University of Utah

December 2016

Copyright © Dae Ung Yoon 2016

All Rights Reserved

ABSTRACT

Marine electromagnetic (EM) surveys have been extensively used for offshore hydrocarbon exploration over the last decade. One can consider two major types of marine EM surveys. One is aimed at conducting a reconnaissance study of the large survey area with the purpose of locating the prospective zones of hydrocarbons accumulation. Another type of the EM surveys is used for a detailed study of these prospective zones with the goal to determine a specific position of the potential HC reservoirs.

In this dissertation, I introduce two new techniques for solving these two important problems — optimal synthetic aperture method for analysis of the reconnaissance surveys and a hybrid finite difference and integral equation method for rigorous 3D inversion of the EM data collected by exploration surveys.

The optimal synthetic aperture method is a technique to find the optimal parameters of the synthetic aperture of the EM data acquisition system, which can steer the generated EM field toward the area of interest by combining the responses from multiple sources, so that it can enhance the anomaly from the potential HC target. With the application of the optimal synthetic aperture method to the conventional MCSEM data and the towed streamer EM data, I demonstrate that the method can be used for not only increasing the EM anomaly from the target, but also reducing the distorting airwave effect in the shallow marine environment. I also demonstrate that the method can be used for mapping

the electric anomalies over the true locations of the targets, which is important for the reconnaissance surveys.

The second technique that I have developed is the hybrid finite-difference and integral equation (FD-IE) method for 3D modeling and inversion of the EM data, which combines the advantages of conventional FD and IE methods. The hybrid FD-IE method makes it possible to provide a more accurate and efficient forward modeling solution than the conventional FD or IE methods for multisource data.

The developed new approaches to analysis and interpretation of the marine EM data have been carefully tested on a number of realistic synthetic models and a case study.

TABLE OF CONTENTS

ABSTRACT.....	iii
ACKNOWLEDGEMENTS.....	vii
Chapters	
1. GENERAL INTRODUCTION.....	1
1.1 History of Marine EM.....	1
1.2 Systems of Marine EM Surveys with the Controlled Source	2
1.3 Motivation.....	4
1.4 Thesis Structure	7
2. OPTIMAL SYNTHETIC APERTURE METHOD FOR MCSEM SURVEYS	9
2.1 Introduction.....	9
2.2 Synthetic Aperture Method.....	10
2.3 Definition of the Optimal Synthetic Aperture for MCSEM Survey.....	13
2.4 Numerical Model Study.....	17
2.4.1 Model 1	
2.4.2 Model 2	
2.5 Reduction of the Air Wave Effect in Shallow Water Using Optimal Synthetic Aperture Method.....	23
2.6 Application of the Optimal Synthetic Aperture Method to the Harding Field MCSEM Data.....	24
2.7 Conclusions.....	27
3. OPTIMAL SYNTHETIC APERTURE METHOD FOR TOWED STREAMER EM SURVEYS.....	45
3.1 Introduction.....	45
3.2 Virtual Receivers	47
3.3 Introducing Synthetic Aperture Data for Towed Streamer EM Survey	49
3.4 Definition of the Optimal Synthetic Aperture Method for Towed Streamer EM Survey	51
3.5 Synthetic Model Study.....	54
3.5.1 Selection of a Designed Normalized Synthetic Aperture Data	

3.5.2 Complex Model with Near-Seafloor Inhomogeneities	
3.6 Application of the Optimal Synthetic Aperture Method to the Towed Streamer EM Data Collected from the Troll West Oil and Gas Province	57
3.7 Conclusions.....	58
4. HYBRID FINITE DIFFERENCE AND INTEGRAL EQUATION METHOD FOR EM MODELING	68
4.1 Introduction.....	68
4.2 Finite Difference Modeling of the Anomalous Electric Field	70
4.3 Integral Equation Method for Computing the EM Field at the Receivers	72
4.4 Formulation of a Hybrid Finite Difference and Integral Equation Method.....	74
4.5 Verification of the Hybrid FD-IE Modeling Method	77
4.5.1 Comparison with a Semianalytical Solution.....	77
4.5.2 Comparison with a 3D Integral Equation Method.....	77
4.6 Conclusions.....	87
5. HYBRID FINITE DIFFERENCE AND INTEGRAL EQUATION METHOD FOR EM INVERSION.....	100
5.1 Introduction.....	100
5.2 Inversion Methodology.....	101
5.3 Synthetic Model Study of the Inversion Algorithm Based on the Hybrid FD-IE Method.....	104
5.3.1 Inversion of Synthetic MCSEM Data	
5.3.2 Inversion of Synthetic Towed Streamer EM Data	
5.4 Inversion of Towed Streamer EM Data Collected from the Troll West Oil Province	107
5.5. Conclusions.....	108
6. GENERAL CONCLUSIONS.....	116
Appendices	
A: WEIGHTED AVERAGING CONDUCTIVITY AND THE CORRESPONDING VOLUME	121
B: CALCULATION OF FRÉCHET DERIVATIVE	124
REFERENCES	127

ACKNOWLEDGEMENTS

This dissertation would not have been possible without the help of so many people in so many ways. First I would like to give a deepest gratitude to my advisor Professor Michael Zhdanov for his support and mentoring over six years of M.S. and Ph.D. research. His guidance and persistent help are the reason I have arrived to the position I am in currently. I also would like to thank Professor Alexander Gribenko for his guidance and leadership. Fruitful discussions during the student seminar hosted by him clarified geophysical research, and helped me to decide the topics of my research. I would also like to thank Dr. Masashi Endo for priceless discussions and practical advice. His insight and industry perspective have always enlightened me and helped me to develop a broad understanding about geophysical problems. I am grateful to my committee members, Professor Erich Petersen and Professor Michael Thorne for their valuable comments and lectures on related topics that helped me improve my knowledge in the area. I would like to thank Professor David Chapman who is one of the best teachers that I have had in my life. Not only his teaching skill but also his caring, patience, and humor let me know what a great teacher is.

I would like to thank all people in Consortium for Electromagnetic Modeling and Inversion (CEMI). Especially, I thank to Dr. Martin Cuma for sharing his knowledge about programming and setting up useful libraries including direct solvers on the clusters at Center for High Performance Computing, University of Utah. Also, I would like to

acknowledge the executive secretary, Kim Atwater for her kindness and caring. Thanks to her, I was able to focus only on my research without any worries about administrative problems. I would like to extend my gratitude to Dr. Hongzhu Cai and Dr. Yue Zhu for being best colleagues and friends during my journey of graduate study.

I would like to thank to my undergraduate advisors, Professor Joongmoo Byun and Professor Soon Jee Seol, and Dr. Seongkon Lee. Their thoughtful advice and encouragement helped me overcome difficult times and stay focused on my graduate study.

Most importantly, none of this would have been possible without the love, caring, and patience of my family. My wife has always supported me, sacrificed her life for me, and encouraged me to do my best. My parents and parents-in-law have always believed in me, and been proud of me. I love you all, and you are the most important people in my life. Thank you all for everything.

CHAPTER 1

GENERAL INTRODUCTION

Over the past 15 years marine controlled-source electromagnetic (MCSEM) method has been extensively used for hydrocarbon exploration. The fundamental fact which makes it very useful for offshore petroleum exploration is that oil- and gas-containing structures are characterized by very high resistivity, while the surrounding sea-bottom formations filled with salt water are very conductive, which makes an oil and gas reservoir a clear target for EM methods. Therefore, marine EM surveys have been considered a very powerful technique for off-shore hydrocarbon exploration, which, in combination with seismic surveys, helps to determine fluid properties of the reservoir.

1.1 History of Marine EM

A few review papers have been published to provide information about the history and the future direction of the MCSEM method (e.g., Zhdanov, 2010; Constable, 2010; MacGregor and Tomlinson, 2014), so only a short summary is provided here.

Geophysical EM methods originally had only been considered for land observations, and in the 1960s, geophysicists started showing an interest in the EM method in the marine environments (Novysh and Fonarev, 1966; Filloux, 1967; Trofimov and Fonarev, 1972). Marine EM methods have been researched academically since the 1960s, however,

commercial application of marine CSEM for hydrocarbon exploration took place in the late 1990s when MCSEM gained strong interest from oil and gas industries (Ellingsrud et al., 2002). Since then, a number of MCSEM surveys were conducted, and continuing developments in instrumentation, survey strategy and technique for interpreting EM data have led to the successful application of EM method for offshore hydrocarbon exploration.

1.2 Systems of Marine EM Surveys with the Controlled Source

The most commonly used marine CSEM survey consists of a transmitter towed by a vessel and receivers deployed on the seafloor. The system was originally developed by Charles Cox of Scripps Institution of Oceanography in the late 1970s (Cox, 1981). A high-powered horizontal electric dipole is used for the transmitter which generates a low-frequency EM signal, typically in the range 0.01-10 Hz, through the seafloor. The transmitter is towed at about 30 m above the seafloor which is close enough to maximize coupling with the earth and to minimize coupling with the air. The seafloor receivers are able to measure up to three components of the electric and three components of the magnetic fields, but usually horizontal components of them are recorded.

Alternatively, two different towed streamer systems have been also developed. The first system consists of a linked linear array of the transmitter and receivers, which are towed close to the seafloor in deep water to avoid coupling with the air (Yuan and Edwards, 2000). As the offsets between transmitter and receivers in the system are shorter (between 85 to 493 m) than those of surface-towed system of Anderson and Mattsson (2010) described below, the survey system has been applied for mapping of resistivity in the shallow subsurface such as gas hydrates.

Another towed streamer EM system has been introduced in Anderson and Mattsson (2010) and Mattsson et al. (2012), which is designed to acquire EM and seismic data simultaneously. Mattsson et al. (2012) have demonstrated that the EM source and receiver array can be much closer to the surface than those in the conventional systems, and still the shallow water noise issues can be overcome. The current generation of Towed Streamer EM systems consists of an 800 m long bipole source towed at a 10 m depth below the sea surface and multiple receivers towed at a 100 m depth. The streamer is loaded with 26 receivers with the longest at 7700 m, so it is designed to detect the shallow target at short source-receiver offsets with high frequencies and the deep targets at long offsets with low frequencies. Other benefits of the system are the denser sampling of the electric field, improved signal-to-noise ratio, and fast acquisition speed compared to the conventional seafloor node CSEM system.

A CSEM system consisting of vertical electric dipole source and receivers has also been developed, which is designed to improve lateral resolution of subseafloor resistivity structure (Holten et al., 2009).

Currently, only two systems among above survey configurations are widely used in industry: the conventional MCSEM survey based on the use of a set of fixed sea-bottom receivers and a towed electric bipole transmitter, and the Towed Streamer EM survey introduced in Mattsson et al. (2012). Therefore, I only consider those two survey systems in my dissertation.

1.3 Motivation

As the use of marine EM methods for offshore exploration has grown, techniques for interpreting the EM data have rapidly developed as well. However, interpretation of both

the MCSEM and Towed Streamer EM data is a very challenging problem because of the complex geoelectrical structures of the sea-bottom formations and a complex signature of the relatively weak response from the HC reservoir. Therefore, introducing new efficient techniques for interpreting the EM data is an important problem of marine EM geophysics. The solution of this problem represents the main focus of this thesis.

One can consider two major types of marine EM surveys. One is aimed in conducting a reconnaissance study of the large survey area with the purpose of locating the prospective zones of hydrocarbons (HC) accumulation. Another type of the EM surveys is used for a detailed study of these prospective zones with the goal to determine a specific position of the potential HC reservoirs. These two types of the marine EM surveys require different approaches to the analysis of the observed data. In the first case of the reconnaissance survey, the goal of interpretation is detection of the areas with the relatively strong EM anomalies, which can be associated with the HC prospective zones. The second case of detailed exploration of the oil and gas prospective zones requires a thorough inversion of the observed data, which can produce a full 3D geoelectrical image of the sea-bottom formations.

The synthetic aperture method is a good candidate for the analysis of the reconnaissance survey because this method is able to steer the generated fields toward the direction of interest area, so that I can increase the anomaly generated from prospective target such as HC reservoir. The synthetic aperture technique was originally introduced for increasing the resolution of radar imaging in the late 1980s, and its concept has been applied in many other fields such as sonar and medical imaging (Soumekh, 1999). The concept of the synthetic aperture was first applied to MCSEM data by Fan et al. (2010), where the authors created a long virtual bipole source with combination of weighted

sources, and successfully increased the EM anomaly by target. Knaak et al. (2013) also applied the synthetic aperture method to MCSEM data with multiple lines of transmitters and receivers. The authors of the cited papers successfully applied the synthetic aperture method to MCSEM data, however they found the optimal weights searching for all the possible combinations of the parameters within their given ranges. The questions then arise for me, "Is the synthetic aperture weight, that they found, the optimal parameters of the synthetic aperture method?," "If not, can I find an efficient optimization technique to determine the optimal parameters of the synthetic aperture method?" My first journey in this dissertation starts with answering those questions.

Once the strong EM anomaly has been detected over the survey area by the reconnaissance survey, the EM inversion can be applied to produce a geoelectrical image of the sea-bottom formations. The most common approach of the EM inversion can be categorized into deterministic and stochastic approach. The deterministic approach, also known as gradient-based inversion, has been more widely used for interpreting the EM data than the stochastic approach which requires much longer runtime for a large dimension of the model parameter. Therefore, the deterministic approach is only considered for the EM inversion in this thesis.

The 3D EM inversion is a very challenging problem because it requires large amount of computation time and memory. Especially, the forward modeling algorithms should be powerful and fast enough to be suitable for repeated use in tens or hundreds of iterations of the inversion.

There are several popular numerical approaches for 3D EM forward modeling: integral equation (IE), finite difference (FD), and finite element (FE) methods (e.g., Zhdanov and Keller, 1994; Zhdanov, 2002, 2009). However, none of these are perfect

because each method has its cons and pros. For example, one of the advantages of the differential equation (DE) methods such as FD and FE methods is the sparsity of their system matrices, which enables us to use a direct solver. The direct solver is well known for its efficiency for multisource data such as MCSEM (Chung et al., 2014). However, the DE methods require extensive mesh refinement in the vicinity of receiver and/or source positions to reduce numerical errors caused by the interpolation and numerical differentiation of the curl for electric and magnetic fields calculation in the receivers. On the other hand, the IE method does not require any discretization near receiver nor source positions because the electric and magnetic fields are calculated based on the Green's tensor approach. However, the system matrix of the IE method is dense, so usually iterative solvers can be used, which is less efficient than the direct solver in the case of multisource data.

As I listed above, there is no "best" modeling method because each method has its advantages and disadvantages. Then the next question arises, "Although there is no best solution, can I make a "better" solution if I combine the advantages of these methods?"

To address those questions above, I have developed two new techniques. The first one is the optimal synthetic aperture method which is an optimization technique to find the optimal parameters of the synthetic aperture method. This method can be used as a very efficient tool for the analysis of the reconnaissance surveys. The second one is a hybrid finite difference (FD) and integral equation (IE) modeling method, which combines the advantages of the FD and the IE method. The developed modeling algorithm is also implemented in a rigorous 3D inversion algorithm, which can be used for detailed exploration of the oil and gas prospective zones.

1.4 Thesis Structure

In this dissertation, I introduce two new techniques: optimal synthetic aperture method for analysis of the reconnaissance surveys and a hybrid finite difference (FD) and integral equation (IE) method for rigorous 3D inversion of the EM data collected by exploration surveys. These techniques are general, and I test these methods using two different configurations of marine EM surveys: the conventional MCSEM and the Towed Streamer EM survey.

In Chapter 2, I describe the optimal synthetic aperture method for the conventional MCSEM survey and demonstrate the effectiveness and efficiency of the developed method comparing the results with those in Fan et al. (2010) and Knaak et al. (2013). I also demonstrate that the optimal synthetic aperture method can be used for not only increasing the anomalous response from target but for also reducing a distorting airwave effect on MCSEM data collected in shallow water. At the end of this chapter, I introduce a scanning scheme for practical use of the optimal synthetic aperture method for analysis of the reconnaissance surveys, using the synthetic MCSEM data simulated from the real model of Harding oil and gas field in the North Sea. The scanning scheme using the optimal synthetic aperture method enables us to figure out the existence of the strong EM anomalies, which can be associated with the HC prospective zones, over the survey area very quickly and efficiently.

In Chapter 3, I expand the application of the optimal synthetic aperture method to the Towed Streamer EM survey. I modify the theory of the optimal synthetic aperture method introduced in Chapter 2, making it suitable for the Towed Streamer EM system. Using a field Towed Streamer EM data from North Sea, I demonstrate that the optimal synthetic aperture method can be used for mapping the horizontal locations of the oil and

gas reservoirs increasing the anomalies right above the target areas. The optimal synthetic aperture method is an innovative technique for analysis of the reconnaissance surveys before applying rigorous 3D EM inversion.

In Chapter 4, I introduce a novel 3D EM modeling algorithm based on hybrid finite difference (FD) and integral equation (IE) method. The developed method combines the advantages of the FD and IE method, which enables us to use the direct solver and to calculate the electric and magnetic fields at the receiver position based on Green's tensor approach, avoiding the need of mesh refinements near receiver positions. In this way, the hybrid FD-IE method provides more accurate solutions than the conventional FD method, and faster solutions than the conventional IE method in the case of the multisource data such as MCSEM and Towed Streamer EM data. Several numerical model studies are presented to demonstrate the efficiency and the accuracy of the developed method over the conventional FD and IE method.

In Chapter 5, the developed hybrid FD-IE modeling method is incorporated as the forward EM modeling engine in a general regularized inversion scheme, based on the reweighted conjugate gradient method. In order to make the inversion algorithm more efficient, I apply the quasi-Born approximation (Gribenko and Zhdanov, 2007; Zhdanov, 2009) on the staggered grid, and the concept of the moving sensitivity domain approach (Cox and Zhdanov, 2007; Zhdanov et al., 2014a, 2014b) to the inversion algorithm. I test the developed inversion code for Towed Streamer EM data collected by PGS over the Troll field in the North Sea.

CHAPTER 2

OPTIMAL SYNTHETIC APERTURE METHOD FOR MCSEM SURVEYS

2.1 Introduction

The synthetic aperture method is based on designing sources with specific radiation patterns, which would “steer” a generated field in the direction of an area of interest (DeGraaf, 1998; Cheney, 2001; Cetin and Karl, 2001; Korobov et al., 2010). A similar approach was recently discussed in Fan et al. (2010, 2012), where the authors applied a synthetic aperture method to the marine controlled-source electromagnetic (MCSEM) survey, formed by one line of transmitters and receivers. Knaak et al. (2013) applied a synthetic aperture method to MCSEM surveys with multiple lines of transmitters and receivers. The method uses the interference of the fields radiated by different sources to construct a virtual source with a specific radiation pattern, according to which the field is steered toward the target. In order to find the optimal parameters of the synthetic aperture that increases the EM anomaly, associated with the target, the authors of the cited papers searched for all the possible combinations of the parameters within the given ranges.

Another approach to achieving this goal is based on introducing data weights in order to increase the integrated sensitivity of a survey to a specific target area of subsurface

formation. For example, it was demonstrated in Kaputerko et al. (2007) that data weighting could dramatically affect the sensitivity distribution of a given survey. In Yoon and Zhdanov (2011) and Zhdanov (2013), the authors demonstrated how the sensitivity of the MCSEM survey could be “controlled” by selecting the appropriate data weights. The controlled sensitivity also results in an increase in the anomalous EM response from the target.

The goal of this chapter is to introduce a general optimization technique to find the optimal parameters of the synthetic aperture method for MCSEM survey. This approach makes it possible to increase the corresponding ratio between total and background fields within the area of expected target anomaly and, in this way, improve the resolution of the EM data with respect to potential subsurface targets. I also demonstrate that the optimal synthetic aperture method can be used for removal of a distorting airwave effect on MCSEM data collected in shallow water. As an illustration, I apply this method to the models exemplified by Fan et al. (2010) and Knaak et al. (2013) and to analysis of the synthetic MCSEM data computer simulated for the Harding oil and gas field in the North Sea.

2.2 Synthetic Aperture Method

Consider a typical marine controlled-source electromagnetic (MCSEM) geophysical survey, formed by a set of sea-bottom electric and magnetic field receivers, located at the points with coordinates $\mathbf{r}_l, l = 1, 2, \dots, L$. The transmitting horizontal electric bipole is towed behind the ship and sends a low-frequency EM field from the points with coordinates $\tilde{\mathbf{r}}_j, j = 1, 2, \dots, J$.

The main target of the MCSEM survey are resistive hydrocarbon (HC) reservoirs located within relatively conducted sea-bottom sedimental layers.

The receivers record the EM data, denoted by vector-column $\mathbf{d}^{(l)} = [d_1^{(l)}, d_2^{(l)}, \dots, d_j^{(l)}]^T$, where the upper index, l , corresponds to the position of the receiver at point \mathbf{r}_l , and the component $d_j^{(l)}$ describes the response recorded by receiver at point \mathbf{r}_l for transmitter located at the point $\tilde{\mathbf{r}}_j$.

Synthetic aperture method is based on constructing a synthetic aperture source, $G_A(\mathbf{r}; \omega)$, as a superposition of the spatially distributed sources, $g(\mathbf{r}, \tilde{\mathbf{r}}_j; \omega)$, located at the points $\tilde{\mathbf{r}}_j, j = 1, 2, \dots, J$:

$$G_A(\mathbf{r}; \omega) = \sum_{j=1}^J a_j \exp(i\varphi_j) g(\mathbf{r}, \tilde{\mathbf{r}}_j; \omega), \quad (2.1)$$

where a_j is an amplitude weighting, and φ_j is a phase shift (Fan et al., 2010).

I denote by $d_A^{(l)}$ the response recorded by receiver $\mathbf{r}_l, l = 1, 2, \dots, L$, for a synthetic aperture source, G_A . Due to superposition principle, this signal can be calculated as a linear combination of the responses for original transmitters:

$$d_A^{(l)} = \sum_{j=1}^J a_j \exp(i\varphi_j) d_j^{(l)}, l = 1, 2, \dots, L. \quad (2.2)$$

Note that, Fan et al. (2010, 2012) used the same amplitude weighting and phase shift for all positions of the receivers. In general case, one can use different synthetic aperture sources, $G_A^{(l)}$, for different positions of the receivers. Therefore, the corresponding

synthetic aperture data, $d_A^{(l)}$, would take the form:

$$d_A^{(l)} = \sum_{j=1}^J a_j \exp(i\varphi_j) d_j^{(l)} = \sum_{j=1}^J w_j^{(l)} d_j^{(l)} = \mathbf{w}^{(l)}[\mathbf{d}^{(l)}]^T, \quad (2.3)$$

where $\mathbf{w}^{(l)}[\mathbf{d}^{(l)}]^T$ is a $[J \times 1]$ vector-column of the data corresponded by receiver at point \mathbf{r}_l ,

$$\mathbf{d}^{(l)} = [d_1^{(l)}, d_2^{(l)}, \dots, d_J^{(l)}]; \quad (2.4)$$

$\mathbf{w}^{(l)}$ is a $[1 \times J]$ vector-row of the corresponding synthetic aperture weights, $w_j^{(l)}$,

$$\mathbf{w}^{(l)} = [w_1^{(l)}, w_2^{(l)}, \dots, w_J^{(l)}]; \quad (2.5)$$

and

$$w_j^{(l)} = a_j \exp(i\varphi_j). \quad (2.6)$$

Expression (2.3) can be written using matrix notations as follows:

$$\mathbf{d}_A = \mathbf{W}_A \mathbf{d}, \quad (2.7)$$

where \mathbf{d} is a $[JL \times 1]$ vector-column of the observed data,

$$\mathbf{d} = [\mathbf{d}^{(1)}, \mathbf{d}^{(2)}, \dots, \mathbf{d}^{(L)}], \quad (2.8)$$

\mathbf{d}_A is an $[L \times 1]$ vector-column of the synthetic aperture data,

$$\mathbf{d}_A = [d_A^{(1)}, d_A^{(2)}, \dots, d_A^{(L)}]^T, \quad (2.9)$$

and \mathbf{W}_A is a $[L \times JL]$ block-diagonal rectangular matrix of the weights,

$$\mathbf{W}_A = \begin{bmatrix} \mathbf{w}^{(1)} & 0 \dots & 0 \dots & 0 \dots \\ 0 \dots & \mathbf{w}^{(2)} & 0 \dots & 0 \dots \\ 0 \dots & 0 \dots & \ddots & 0 \dots \\ 0 \dots & 0 \dots & 0 \dots & \mathbf{w}^{(L)} \end{bmatrix}. \quad (2.10)$$

Application of the synthetic aperture weights, variable from the receiver to the receiver, is physically equivalent to "steering" the field generated from the transmitters in the different directions for different receivers. As a result, it is possible to obtain better "focusing" of the transmitting EM field on the geological target, e.g., the hydrocarbon (HC) reservoir.

2.3 Definition of the Optimal Synthetic Aperture for MCSEM Survey

For simplicity, I consider now the case of the weights, independent of the receiver positions. I also assume that the recorded data represent the inline component of electric field. In this case, matrix equation (2.7) can be simplified as follows:

$$\mathbf{d}_A = \begin{bmatrix} w_1 E_1^{(1)} + w_2 E_2^{(1)} + \dots + w_J E_J^{(1)} \\ w_1 E_1^{(2)} + w_2 E_2^{(2)} + \dots + w_J E_J^{(2)} \\ \vdots \\ w_1 E_1^{(L)} + w_2 E_2^{(L)} + \dots + w_J E_J^{(L)} \end{bmatrix}, \quad (2.11)$$

where $E_j^{(l)}$ describes the electric field recorded by receiver at point \mathbf{r}_l for the transmitter located at the point $\tilde{\mathbf{r}}_j$, and

$$w_j = a_j \exp(i\varphi_j), j = 1, 2, \dots, J \quad (2.12)$$

Equation (2.11) can be decomposed as follows:

$$\mathbf{d}_A = \begin{bmatrix} E_1^{(1)} & E_2^{(1)} & \dots & E_J^{(1)} \\ E_1^{(2)} & E_2^{(2)} & \dots & E_J^{(2)} \\ \vdots & \vdots & \ddots & \vdots \\ E_1^{(L)} & E_2^{(L)} & \dots & E_J^{(L)} \end{bmatrix} \begin{bmatrix} w_1 \\ w_2 \\ \vdots \\ w_J \end{bmatrix} = \mathbf{E}\mathbf{w}, \quad (2.13)$$

where \mathbf{E} is a $[L \times J]$ matrix of rearranged observed electric fields, and \mathbf{w} is a $[J \times 1]$ vector-column of the corresponding synthetic aperture weights, w_j ,

$$\mathbf{w} = [w_1, w_2, \dots, w_J]^T. \quad (2.14)$$

In the case of MCSEM survey, the measured electric field decays quickly with the increase of the distance (offset) between the transmitter and receivers, which makes it difficult to detect the anomaly related to the target reservoir. In order to overcome this problem, the observed electric field data are usually normalized by the amplitude of the background electric field, which is computed for the geoelectrical model with the known background conductivity according to the following formula:

$$E_j^{N(l)} = \frac{E_j^{(l)}}{|E_j^{b(l)}|}, \quad (2.15)$$

where $E_j^{b(l)}$ describes the inline component of the background electric field recorded by receiver at point \mathbf{r}_l for the transmitter located at the point $\tilde{\mathbf{r}}_j$.

In a similar way, one can enhance the effect of the resistivity anomaly (e.g.,

associated with the hydrocarbon reservoir) by computing the ratio of the electric field responses generated by the synthetic aperture source and synthetic aperture responses for the background geoelectrical model. The steps required for computing these ratio are described below.

By analogy with expression (2.3), I denote by $d_B^{(l)}$ the electric field response recorded by receiver $\mathbf{r}_l, l = 1, 2, \dots, L$, for a synthetic aperture source, G_A , computed for the geoelectrical model with the known background conductivity. Similar to formula (2.13), the synthetic aperture response for the background geoelectrical model, \mathbf{d}_B , can be expressed as follows:

$$\mathbf{d}_B = \begin{bmatrix} E_1^{b(1)} & E_2^{b(1)} & \dots & E_J^{b(1)} \\ E_1^{b(2)} & E_2^{b(2)} & \dots & E_J^{b(2)} \\ \vdots & \vdots & \ddots & \vdots \\ E_1^{b(L)} & E_2^{b(L)} & \dots & E_J^{b(L)} \end{bmatrix} \begin{bmatrix} w_1 \\ w_2 \\ \vdots \\ w_J \end{bmatrix} = \mathbf{E}^b \mathbf{w}, \quad (2.16)$$

where \mathbf{E}^b is an $[L \times J]$ matrix of rearranged background electric fields, and \mathbf{d}_B is an $[L \times 1]$ vector-column,

$$\mathbf{d}_B = \left[d_B^{(1)}, d_B^{(2)}, \dots, d_B^{(L)} \right]^T. \quad (2.17)$$

The vector-column, \mathbf{d}_R , of the ratio between the observed inline electric fields and background fields of the synthetic aperture can be expressed as:

$$\mathbf{d}_R = \left[d_A^{(1)}/d_B^{(1)}, d_A^{(2)}/d_B^{(2)}, \dots, d_A^{(L)}/d_B^{(L)} \right]^T = \mathbf{A}(\mathbf{w}), \quad (2.18)$$

where

$$\frac{d_A^{(l)}}{d_B^{(l)}} = \frac{\left[\sum_{j=1}^J E_j^{(l)} w_j \right]}{\left[\sum_{j=1}^J E_j^{b(l)} w_j \right]}, \quad (2.19)$$

and \mathbf{A} is a forward operator for the normalized synthetic aperture data \mathbf{d}_N , which is a function of the synthetic aperture weights, \mathbf{w} .

The fundamental concept of a synthetic aperture method is based on an assumption that one can design the synthetic aperture source which will steer the EM energy toward the target and in this way increase the ability to detect the target (Fan et al., 2010, 2012) by increasing the anomalous response from the target. This effect can be achieved automatically by selecting the synthetic aperture weights with the property that they magnify the normalized synthetic aperture data, \mathbf{d}_N , in the anticipated area of the location of potential target. For example, let me introduce a vector-column \mathbf{P} , describing a designed normalized synthetic aperture data, which have a maximum over a specific area of the survey where I would like to steer the EM energy from a synthetic aperture source.

The optimal synthetic aperture weights are determined by solving a minimization problem for the following objective functional:

$$\varphi(\mathbf{w}) = \|\mathbf{P} - \mathbf{A}(\mathbf{w})\|^2 + \alpha \|\mathbf{w} - \mathbf{w}_{\text{apr}}\|^2 = \min. \quad (2.20)$$

The minimization problem (2.20) is solved by using the regularized conjugate gradient method as follows (Zhdanov, 2002):

$$\mathbf{r}_n = \mathbf{A}(\mathbf{w}_n) - \mathbf{P}, \quad (2.21)$$

$$\mathbf{l}_n = \mathbf{F}_n^T \mathbf{r}_n + \alpha(\mathbf{w}_n - \mathbf{w}_{\text{apr}}), \quad (2.22)$$

$$\beta_n = \|\mathbf{l}_n\|^2 / \|\mathbf{l}_{n-1}\|^2, \quad (2.23)$$

$$\hat{\mathbf{I}}_n = \mathbf{I}_n + \beta_n \hat{\mathbf{I}}_{n-1}, \quad \hat{\mathbf{I}}_0 = \mathbf{I}_0, \quad (2.24)$$

$$k_n = (\hat{\mathbf{I}}_n^T \mathbf{I}_n) / (\|\mathbf{F}_n \hat{\mathbf{I}}_n\|^2 + \alpha \|\hat{\mathbf{I}}_n\|^2), \quad (2.25)$$

$$\mathbf{w}_{n+1} = \mathbf{w}_n - k_n \hat{\mathbf{I}}_n, \quad (2.26)$$

where \mathbf{F}_n is the Fréchet derivative matrix of the operator \mathbf{A} at iteration n , which can be calculated based on perturbation method, and \mathbf{w}_{apr} is some a priori estimate of the data weights.

Once the synthetic aperture weights, $\mathbf{w} = [w_1, w_2, \dots, w_J]^T$ are found, one can convert them into the synthetic aperture parameters as follows:

$$a_j = |w_j|; \quad \varphi_j^{(l)} = \arg(w_j). \quad (2.27)$$

2.4 Numerical Model Study

2.4.1 Model 1

For comparison, I first apply the optimal synthetic aperture method to one of the models exemplified in Fan et al. (2010). The model consists of 1 km deep seawater and the sea-bottom sediments with a resistivity of 1 ohm-m. A HC reservoir with a resistivity of 100 ohm-m is located 1 km below the seafloor with horizontal extent of 4 km in the x- and y- directions and a thickness of 100 m (Figure 2.1). The receivers are located at the seafloor from -10 km to 10 km. The EM field in this model is generated by a 100 m bipole source with a current of 100 A, which is towed 100 m above the receivers. The source current oscillates with a frequency of 0.25 Hz.

I construct a 5 km synthetic aperture source using the electric bipole transmitters

located from -9 km to -4 km. I consider two synthetic apertures. One is based on the coefficients developed in Fan et al. (2010) applying a linear phase shift to the sequential sources in order to steer the EM energy towards the reservoir. The other one is based on the optimal synthetic aperture method.

Figure 2.2 provides an illustration of the optimal synthetic aperture method. Panel a in Figure 2.2 shows the in-line electric field for the model with the HC reservoir (dashed-dotted line) and the corresponding background in-line electric field computed for the model without an HC reservoir (solid line) for a single 100 m bipole source. Panel b presents the in-line electric field for the model with the HC reservoir (bold solid line) and without reservoir (solid line) for a synthetic aperture source without steering. Panel c presents the in-line electric field for the model with the HC reservoir (dashed line) and the corresponding background in-line electric field computed for the model without a HC reservoir (solid line) for a synthetic aperture source introduced by Fan et al. (2010). Panel d shows the plots of the in-line electric field for the model with the HC reservoir (dotted line) and the corresponding background in-line electric field computed for the model without a HC reservoir (solid line) for the optimal synthetic aperture source. The bottom panel e presents the plots of the normalized data, computed as the ratio of the electric field responses generated for the model with HC reservoir and the corresponding background electric fields (without the HC reservoir). The dashed line in panel e shows the normalized synthetic aperture data based on the coefficients developed in Fan et al. (2010). The dotted line represents the similar data produced by the optimal synthetic aperture method, and the dashed-dotted line corresponds to the fields generated by a single 100 m bipole source. The bold dashed line in panel e indicates a designed

normalized synthetic aperture data \mathbf{P} , which are introduced by a boxcar function drawn over the area of the expected reservoir anomaly detected by a single 100 m bipole source. One can see that the developed method successfully finds the optimal synthetic aperture weights for this model which increases the ratio of the observed and background fields up to 60 times, while the highest ratio produced by Fan et al. (2010) is about 40.

Actually, the optimal synthetic aperture method makes it possible to obtain a higher ratio, if I increase the designed a priori normalized synthetic aperture data \mathbf{P} . Figure 2.3 shows the results with the higher a priori ratio. One can see that the ratio of the observed and background fields computed for the optimal synthetic aperture reaches up to 150, and the anomaly is getting sharper due to focusing the energy within the target reservoir.

I also investigate the effect of noise on synthetic aperture data. The synthetic observed data are contaminated with random Gaussian noise. The noise level increases linearly from 1 % at zero offset up to 7 % at 10,000 m offset to simulate the noise behavior typical in the field data. The typical normalized in-line electric field data generated by a single 100 m bipole source for the model with an HC reservoir are shown in panel a of Figure 2.4. Panel b presents the normalized in-line electric field for synthetic aperture source without steering. Panel c shows similar plots for the optimal synthetic aperture source. One can see that the optimal synthetic aperture method provides a stable increase in the ratio of the observed and background fields in the case of noisy data as well.

2.4.2 Model 2

Knaak et al. (2013) presented an example of the application of synthetic aperture method to a 3D synthetic CSEM data with a 2D source distribution. In this section, the same model is used to demonstrate the advantages of the developed optimal synthetic aperture method. The model consisted of 2 km deep seawater layer with a resistivity of 0.33 ohm-m, and anisotropic layered sea-bottom sediments (background model) (see Knaak et al., 2013). A 4 km x 4 km x 50 m reservoir structure is located at 3.5 km depth with an isotropic resistivity of 35 ohm-m (Figure 2.5). The receivers are located at the sea bottom and spanned from -7 km to 7 km in the in-line (x) direction and from -4 km to 4 km in the cross line (y) direction spaced every 250 m. The model contains seven towlines 2 km apart and 15 km long over a 4 km x 4 km x 50 m reservoir at a depth of 3.5 km. The source is a 300 m horizontal dipole with a frequency of 0.2 Hz. The outlines of the reservoir and source locations are shown by solid and dash line, respectively, in Figure 2.6.

First, I repeat the numerical experiments presented by Knaak et al. (2013), where the authors created a 2D synthetic aperture source which extended from -6.6 km to -1.8 km in the in-line direction and was 4 km wide in the cross-line direction. Panel a in Figure 2.6 presents the original plot of the normalized data, computed as the ratio of the in-line electric field responses generated by a single source for the model with HC reservoir and the corresponding background electric fields (without the HC reservoir). Panel b shows the normalized synthetic aperture data for synthetic aperture source without steering. Panel d presents the normalized data produced by the optimal synthetic aperture method. The designed normalized synthetic aperture data **P** are selected as a simple boxcar

function covering the area of the expected reservoir anomaly detected by a single 100 m bipole source, as shown in panel c of Figure 2.6. One can see that the optimal synthetic aperture method successfully found optimal synthetic aperture weights for this model which significantly increases the ratio of the observed and background fields.

I should note that, Knaak et al. (2013) have also determined the parameters of the synthetic aperture with the goal to maximize the normalized synthetic aperture data, which they called the detectability ratio. However, in order to reach this goal the authors of the cited paper applied the global search method by considering variable combinations of the parameters from a given sample set. Figure 2.7 shows the normalized synthetic aperture data computed for a synthetic aperture source without steering (panel a), for the best steered 2D synthetic aperture source, developed by Knaak et al. (2013), and the same plot produced by the optimal synthetic aperture source (panel c). For a better comparison, the profiles along a vertical dashed line shown in Figure 2.7 are plotted in Figure 2.8. One can see that the optimal synthetic aperture method provides stronger and more apparent anomaly of the normalized synthetic aperture data than the one used in Knaak et al. (2013). The reason can be explained by two factors: first, the optimal synthetic aperture method does not impose any limitations on the synthetic aperture weights, w_j , while Knaak et al. (2013) limited the weights within their given ranges; second, the weights in the optimal synthetic aperture method are determined from the optimization technique to provide the optimal set of the weights depending on the area where the user wants to focus the generated fields, while the method in Knaak et al. (2013) only steer the fields toward the direction of the area of interest.

I also examine the effect of the noise on the synthetic aperture data. The synthetic

observed data from Model 2 are contaminated with random Gaussian noise, which increased linearly from 1 % at zero offset up to 7 % at 10,000 m offset to simulate the noise behavior typical in the field data. Panels in Figure 2.9 show the maps of the fields generated from the noisy data for different synthetic aperture sources. Panel a presents the normalized synthetic aperture data computed for a synthetic aperture source without steering. Panel b shows the same data for the best steered 2D synthetic aperture source, developed by Knaak et al. (2013). Panel c presents the same data for the optimal synthetic aperture source. Figure 2.10 presents the profiles of the same data along the vertical dashed line shown in Figure 2.9. One can see that the synthetic aperture methods provide very stable results for noisy data and, especially, the optimal synthetic aperture method increases the anomaly due to HC reservoir more significantly than the method by Knaak et al. (2013), for the noisy data as well.

The question may arise if the developed algorithm could generate a false anomaly in the area, where there is no HC reservoir present? In order to address this question, I consider the same deep water model (Model 2) as above, except that there is no reservoir in this model below the seawater layer. I also assume that the background conductivity in the new model is slightly different from the original background model, e.g., by 3%, and the synthetic observed data in a new model without an HC reservoir are contaminated with noise, as was done above. Figure 2.11(a) shows the synthetic aperture data without steering normalized by new background field and noise added. Figure 2.11(b) shows the same data for the best steered 2-D synthetic aperture source, developed by Knaak et al. (2013). Figure 2.11(c) presents the same data for the optimal synthetic aperture source. One can see that in the case without an HC reservoir, the developed algorithm does not

produce any anomaly even if the selected background model is different from the true background.

2.5 Reduction of the Air Wave Effect in Shallow Water

Using Optimal Synthetic Aperture Method

One of the problems for interpreting MCSEM data in shallow water is the effect of the so-called air wave, which represents that part of an EM signal from the transmitter propagating over the sea surface. This phenomenon was discussed in Zhdanov and Keller (1994), in context of the analysis of the field of the electric dipole source in horizontally layered earth. One can think of the EM field of an electric bipole source as consisting of two parts; the first part propagates in the upper half-space (in the insulating atmosphere) with virtually no attenuation, and then permeates into the seawater, passing through the water layer and reaching the sea-bottom receivers, and the second part propagates directly to the receivers through the conductive layers of the seawater and sea-bottom sediments. The former part of EM field, propagating in the air over the sea surface, is called an air wave. It should be apparent that, in deep water areas with the depth greater than a wave length, only the second part of the field is recorded in the receivers, and the first part is almost completely attenuated. However, in shallow water, the air wave becomes a dominant part of the observed field, which may completely distort the response from the sea-bottom target. Analysis and removal of the airwave effect has been a subject of a number of publications (e.g., Amundsen et al., 2006; Constable and Weiss, 2006; Um and Alumbaugh, 2007; Andreis and MacGregor, 2007). In this section, I demonstrate that the optimal synthetic aperture method can solve this problem.

Model 2 consists of deep water layer with a depth of 2 km, where the airwave is negligible at the acquisition level (sea bottom). I design a new model (Model 3), which is similar to Model 2, but the water depth is 200 m (see Figure 2.12). In this case one should expect a strong air wave effect in the observed data.

Panel a of Figure 2.13 shows the original normalized data for Model 3, computed as the ratio of the in-line electric field responses generated by synthetic aperture source for the model with HC reservoir and corresponding background electric fields (without the HC reservoir). By comparison of this plot with the one in the deep water model (Figure 2.6, panel b), one can see that the anomaly response in the shallow water is dramatically distorted by the effect of the air wave. In order to remove this distorting effect, I have designed a synthetic aperture data in a form of a boxcar function covering the area of the expected reservoir anomaly (Figure 2.13, panel b). Finally, panel c presents the normalized synthetic aperture data produced by the optimal synthetic aperture method based on the designed boxcar function response. One can see that the plot of the normalized synthetic aperture data in Figure 2.13 (panel b) has a regular shaped oval structure, similar to the one shown in Figure 2.6, panel d, for a deep-water anomaly. This observation confirms that the optimal synthetic aperture method can remove the distorting effect of the air wave from the observed shallow water data.

2.6 Application of the Optimal Synthetic Aperture Method to the Harding Field MCSEM Data

I have applied the developed optimal synthetic aperture method to synthetic MCSEM data computer-simulated for a Harding oil and gas field located in the UK sector of the

North Sea, about 320 km northeast of Aberdeen (Figure 2.14). The field has a high net-to-gross, high quality, Eocene Balder sandstone reservoir about 1,700 m below the seafloor in a 110 m water column. Production commenced in 1996 from the Harding central and south reservoirs with 300 Mboe initially in place. Since then, two further reservoirs have been developed: Harding south east, and by extended reach drilling, Harding North. The reservoirs contain gas, and this has been injected back into a gas cap for later production. Oil production is now in decline, with current production of approximately 10,000 bpd with increasing water cut. The remaining hydrocarbon column consists of a gas cap about 100 m thick, and a thin oil rim about 20 m thick (Ziolkowski et al., 2010; Zhdandov et al., 2012).

The Harding field porosity and fluid saturation models were obtained from history-matched reservoir simulations constructed from production data, well logs, and 3D seismic interpretations (Ziolkowski et al., 2010; Zhdandov et al., 2012). The corresponding 3D resistivity model consists of a 110 m sea water column with a resistivity of 0.3 Ohm-m overlying a homogeneous half-space of 1.0 Ohm-m in which the Harding reservoir model is embedded (Figure 2.15).

The source is a 200 m long horizontal electric dipole with a frequency of 0.25 Hz. I construct a synthetic aperture source using three towlines spaced 1 km apart with 39 source locations as shown by red lines in Figure 2.16. The receivers are located at the sea bottom and spanned from -7 km to 7 km spaced 500 m apart in x and y directions. The MCSEM data are then simulated for the model and contaminated with random Gaussian noise, which increases linearly from 1 % at zero offset up to 7 % at 10,000 m offset. Figure 2.16 presents the synthetic aperture data without steering for the Harding field

model. One can see that the effect of the HC reservoir is very weak and distorted in this image not only because of the noise, but also the effect of the air wave.

In order to remove the distorting effect and find the anomaly from the reservoir, I apply the optimal synthetic aperture method using a designed synthetic aperture data in the form of a boxcar function. In this example, it is not ambiguous where the area of the expected electric field anomaly is, but let me assume that I do not know where to apply the box (window) of the designed synthetic aperture data. In this case, one can scan all over the survey area with moving the window to find the most increased anomaly.

Figure 2.17 shows the results of the optimal synthetic aperture method with the scanning scheme and the blue windows indicate the box areas of the designed synthetic aperture data. As one can see if the window is placed far from the true anomaly (panel a, b, c), the optimal synthetic aperture method does not generate any false anomalies. But if the window gets closer to the area of true anomaly, the anomalous response becomes stronger. Finally, when the window fully cover the area of the true anomaly as shown in panel e, it provides the strongest and apparent anomaly.

The optimal synthetic aperture methods on this model were ran using a PC with Intel Core i7, 32 GB, and 2.5 GHz, and the computation time for one searching scheme was few seconds.

The synthetic MCSEM data simulated from the Harding field is used to demonstrate a capability of the developed method for removing the air wave effect from the observed shallow-water data. Also this method enables us to find out whether the HC reservoir is present or not over the survey area.

2.7 Conclusions

The synthetic aperture method, introduced for the marine CSEM method in Fan et al. (2010, 2012) and Knaak et al. (2013), uses an integrated source as a combination of multiple individual sources, in order to increase the detectability of hydrocarbon reservoirs. I have demonstrated that this method can be mathematically described as the data weighting with a special way of selecting the data weights in order to construct the synthetic aperture source. The special data weights, called the synthetic aperture weights, is physically equivalent to "steering" the generated field, so that one can increase the EM anomaly from the geological target, e.g., the HC reservoir. I have developed a general optimization technique to find the optimal parameters (the synthetic aperture weights) of the synthetic aperture method. This approach makes it possible to increase the corresponding ratio between total and background fields within the area of an expected reservoir anomaly and, in this way, improve the resolution of the EM data with respect to potential subsurface targets. I have also demonstrated that the optimal synthetic aperture method can be used for a removal of the distorting airwave effect from the MCSEM data collected in shallow water. Lastly, using the MCSEM data computer-simulated for the Harding oil and gas field in the North Sea, I have shown how to find the strongest electric anomaly from HC reservoir using the scanning scheme with moving window.

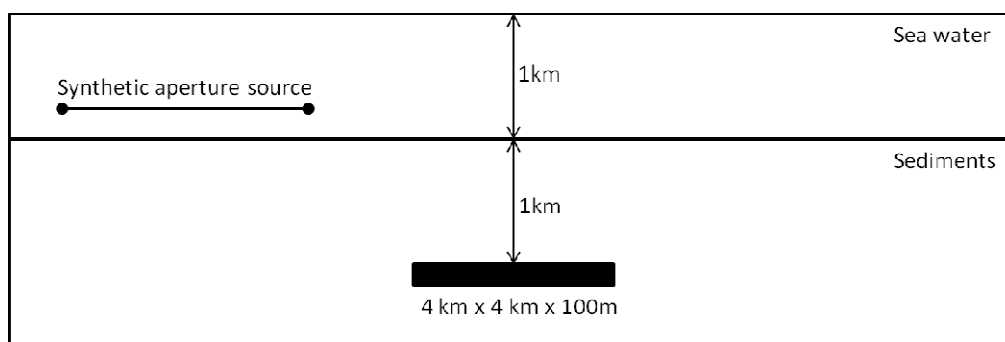


Figure 2.1. Sketch of Model 1

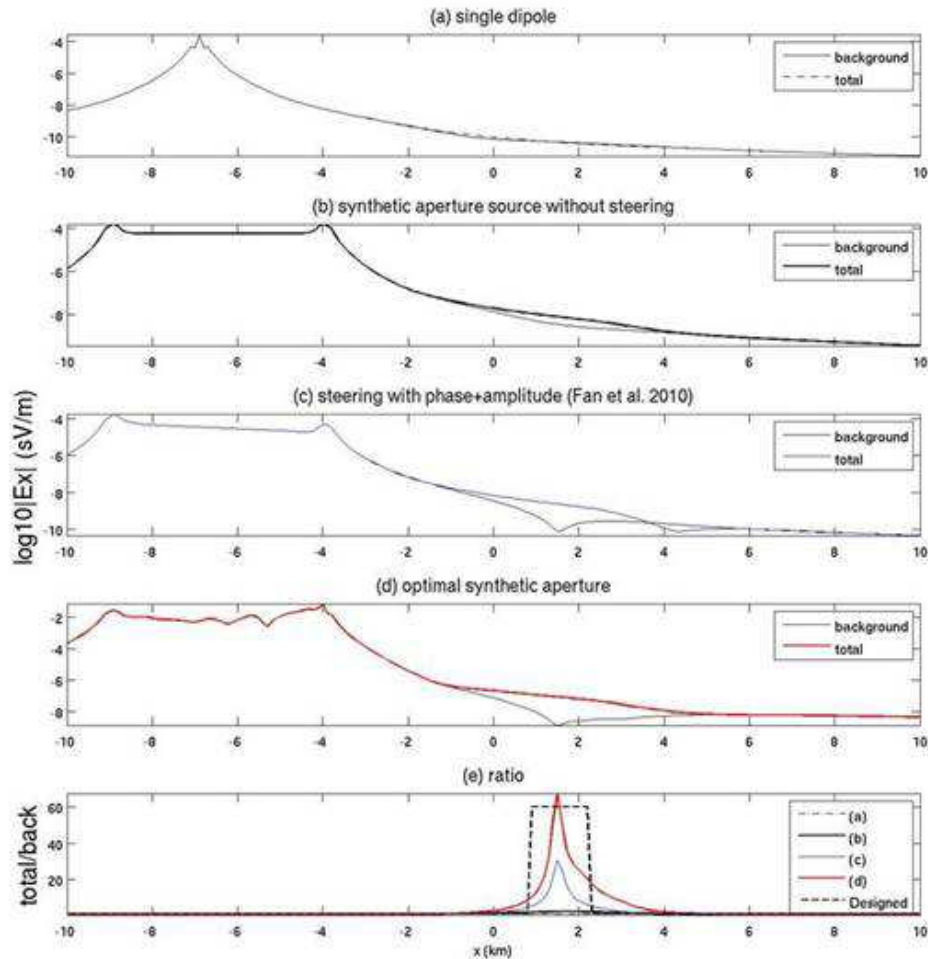


Figure 2.2. Model 1. Panel a shows the in-line electric field for a model with an HC reservoir (dashed-dotted line) and the corresponding background in-line electric field computed for a model without an HC reservoir (solid line) for a single 100 m bipole source. Panel b presents the in-line electric field for the model with the HC reservoir (bold solid line) and without reservoir (solid line) for a synthetic aperture source without steering. Panels c and d present the inline observed and background electric fields for synthetic aperture sources constructed by Fan et al. (2010) and by the optimal synthetic aperture method, respectively. The corresponding ratios between the observed and background fields are shown in panel e. The designed a priori ratio is presented as a bold dashed line in panel e.

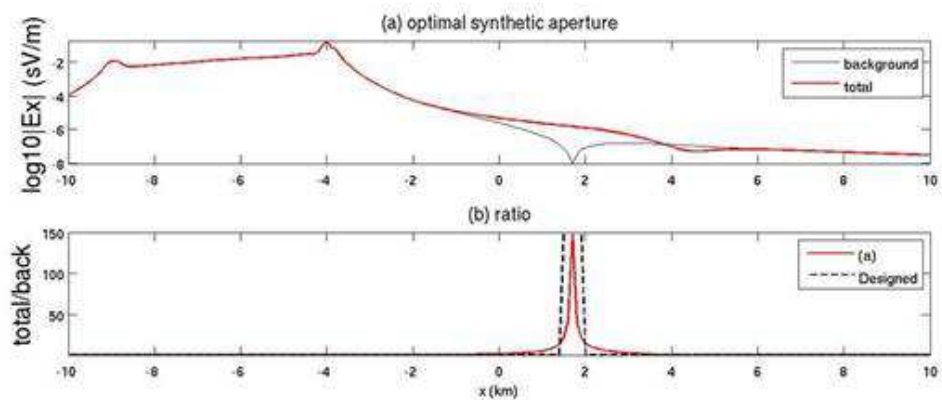


Figure 2.3. Model 1. In-line total and background electric fields with applied optimal synthetic aperture weights (top panel) using a higher a priori ratio (dotted line in bottom panel). The corresponding ratios between the total and background fields in the top panel is shown in dotted line in the bottom panel.

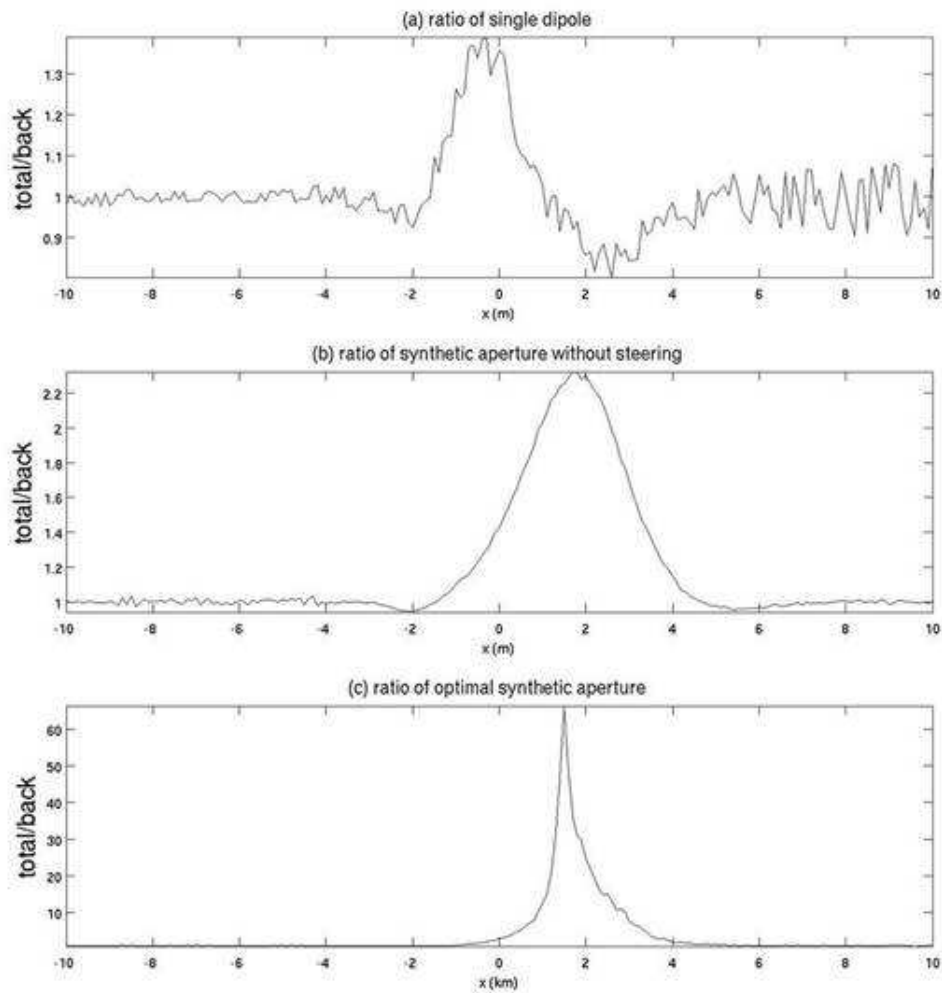


Figure 2.4. Model 1. Panel a shows the normalized in-line electric field data generated by a single 100 m bipole source for the model with the HC reservoir. Panel b presents the corresponding field generated from the noisy data for a synthetic aperture source without steering. Panel c shows similar plot for the optimal synthetic aperture source.

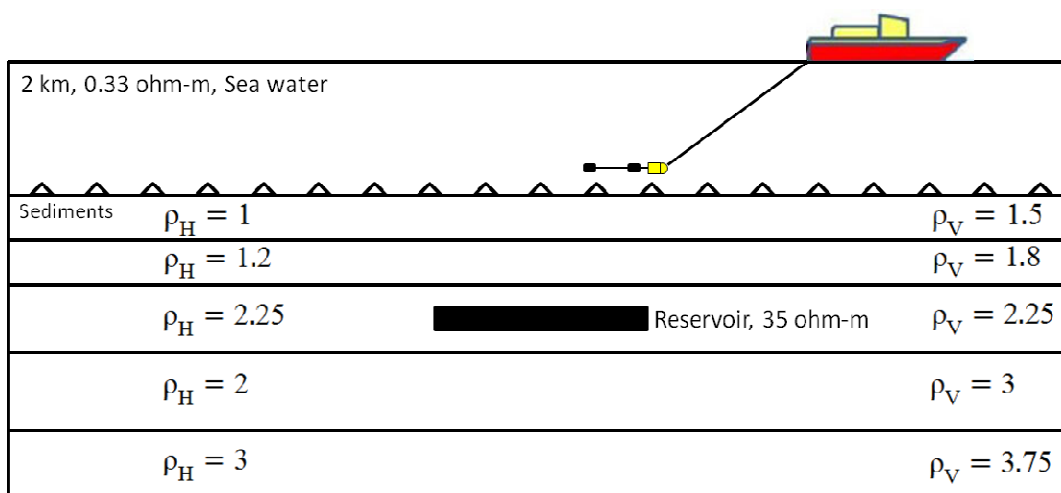


Figure 2.5. Sketch of Model 2.

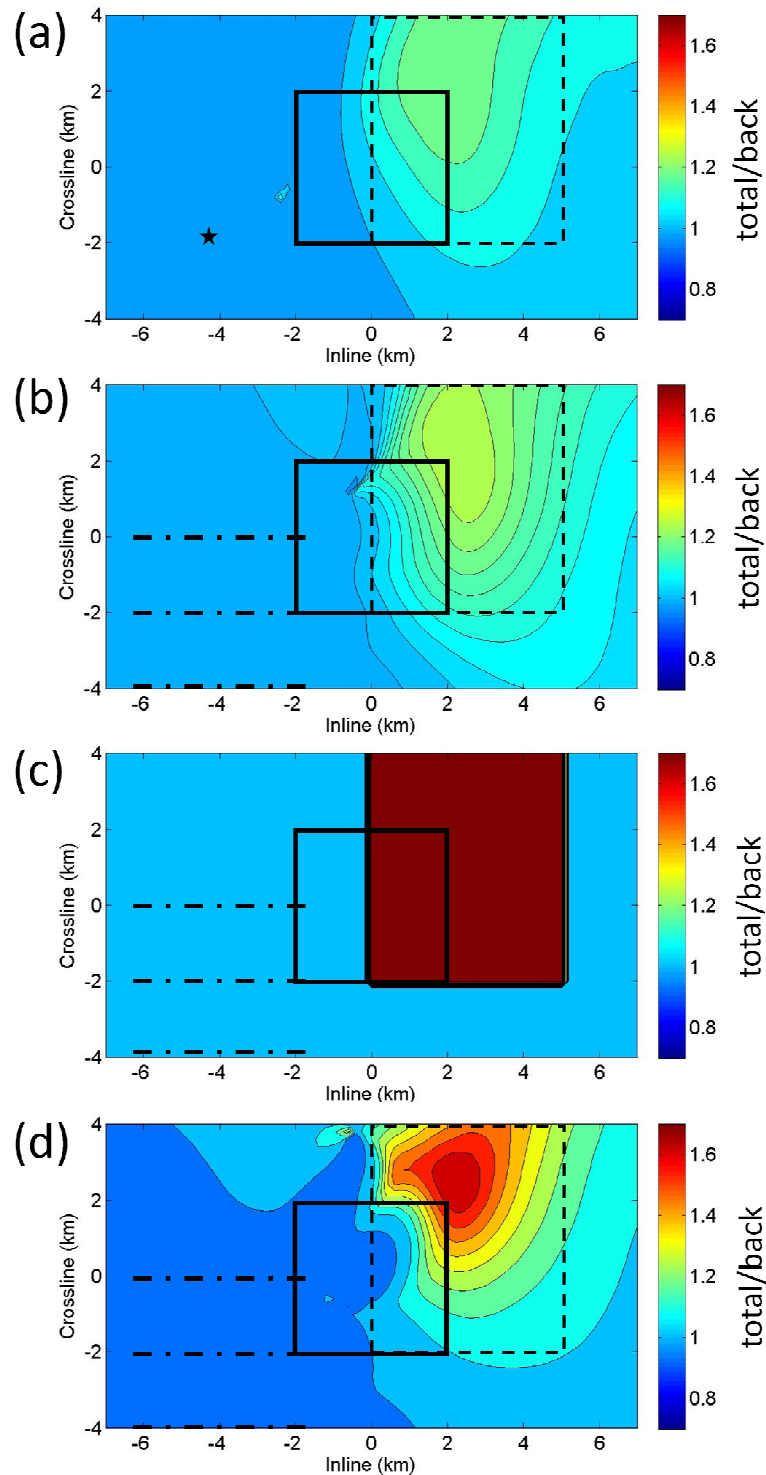


Figure 2.6. Model 2. Panel a shows the original plot of the normalized data by a single source. Panel b presents the normalized synthetic aperture data without steering. Panel c shows the plot of the designed normalized synthetic aperture in a form of boxcar function covering the area of the expected reservoir anomaly. Panel d presents the similar data produced by the optimal synthetic aperture method.

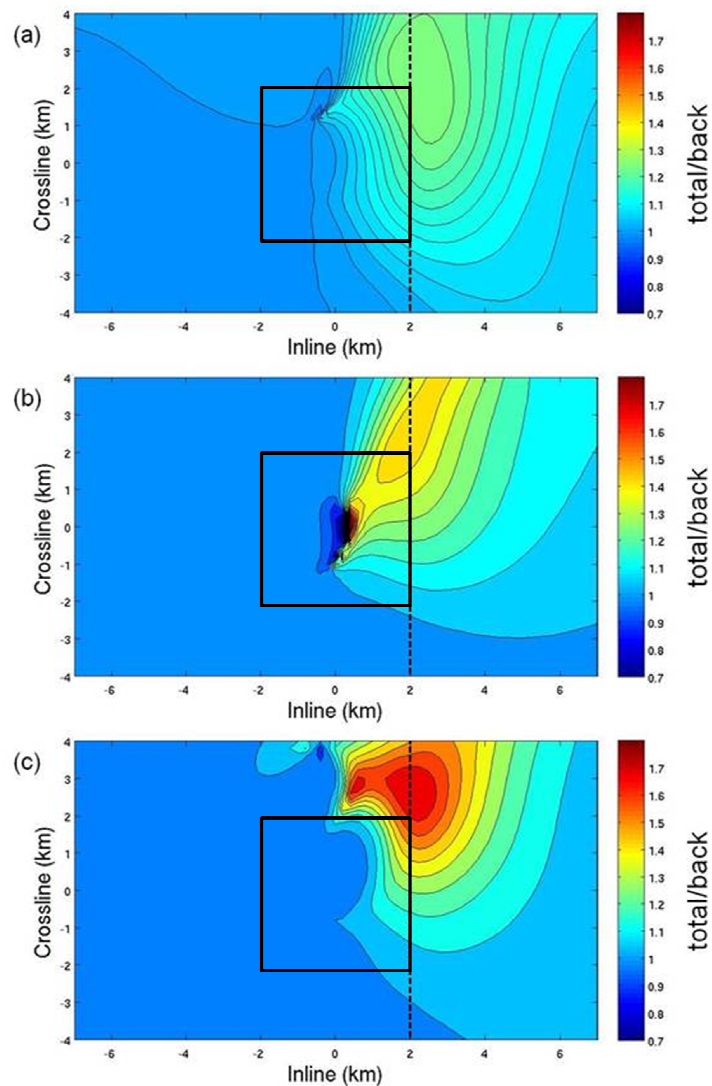


Figure 2.7. Model 2. Maps of the normalized synthetic aperture data computed for a synthetic aperture source without steering (panel a), for the best steered 2D synthetic aperture source, developed by Knaak et al. (2013) (panel b), and for the optimal synthetic aperture source (panel c).

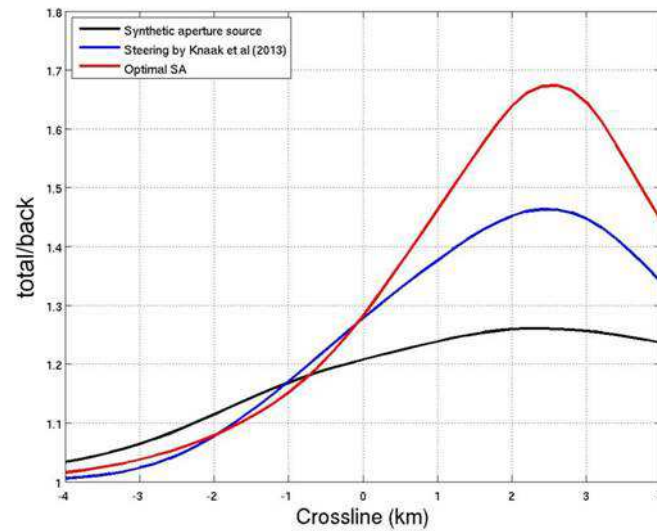


Figure 2.8. Model 2. Profiles of the normalized synthetic aperture data computed for different synthetic aperture sources: the black line represents the normalized synthetic aperture data computed for a synthetic aperture source without steering; the blue line shows the same data for the best steered 2D synthetic aperture source, developed by Knaak et al. (2013); and the red line presents the same data for the optimal synthetic aperture source.

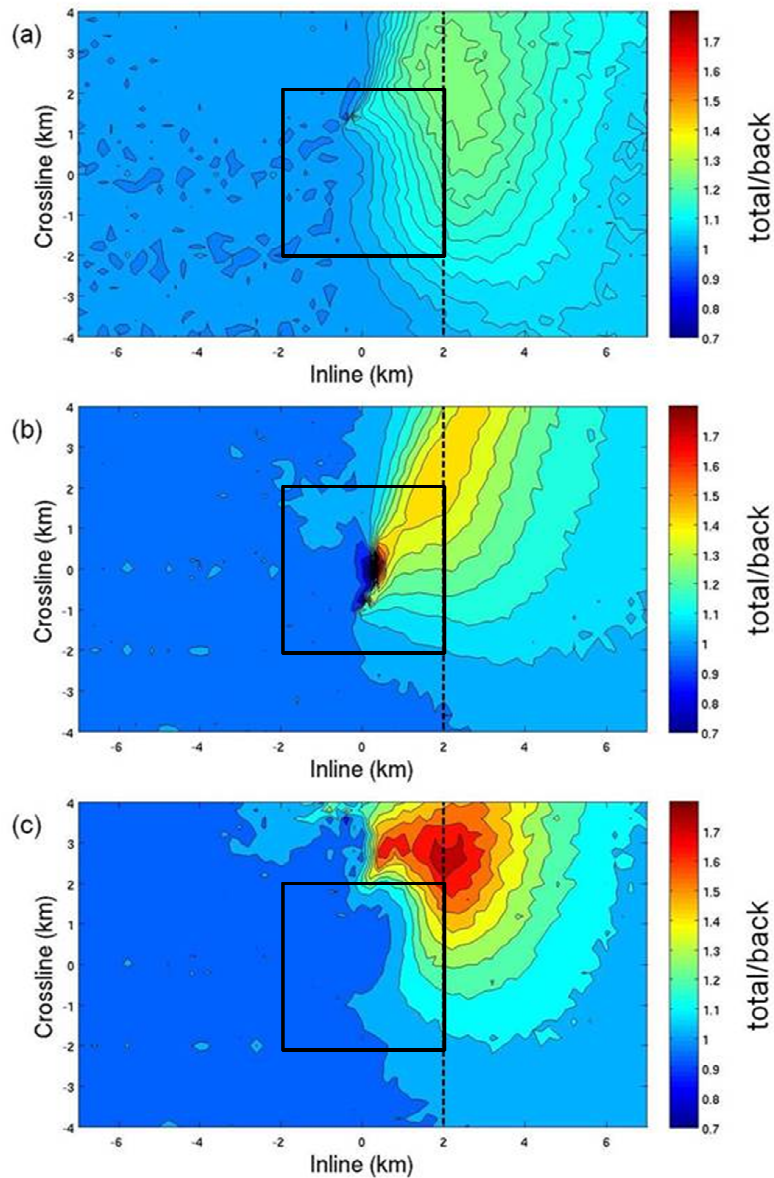


Figure 2.9. Maps of the fields generated from noisy data for different synthetic aperture sources. Panel a presents normalized synthetic aperture data computed for a synthetic aperture source without steering. Panel b shows the same data for the best steered 2D synthetic aperture source, developed by Knaak et al. (2013). Panel c, presents the same data for the optimal synthetic aperture source.

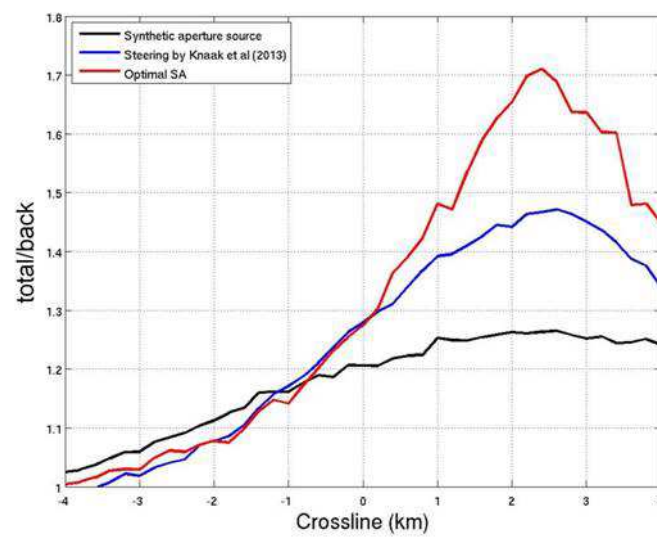


Figure 2.10. Profiles of fields generated from noisy data for different synthetic aperture sources: the black line represents the normalized synthetic aperture data computed for a synthetic aperture source without steering; the blue line shows the same data for the best steered 2D synthetic aperture source, developed by Knaak et al. (2013); and the red line represents the same data for the optimal synthetic aperture source.

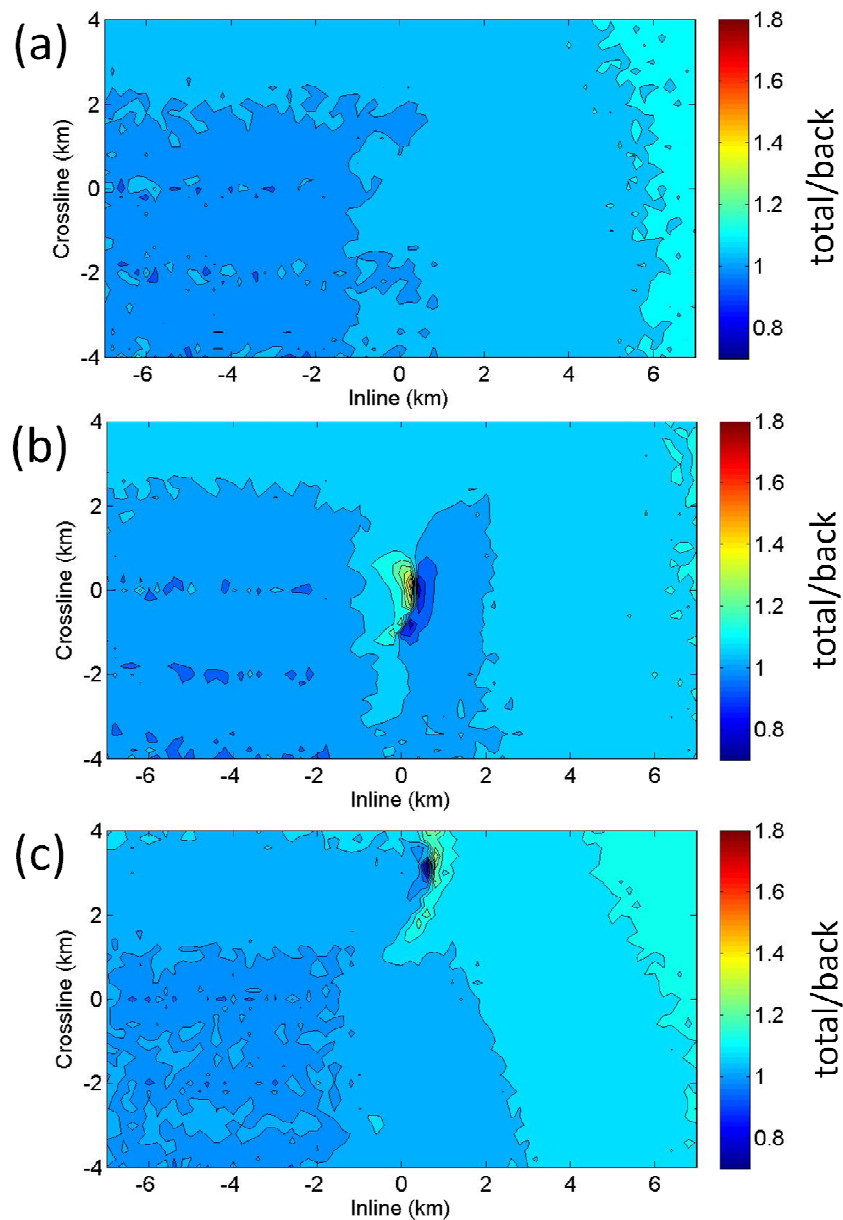


Figure 2.11. Model 2 without the HC reservoir. Maps of the fields generated from noisy data for different synthetic aperture sources. (a) Normalized synthetic aperture data computed for a synthetic aperture source without steering. (b) Same data for the best steered 2-D synthetic aperture source, developed by Knaak et al. (2013). (c) Same data for the optimal synthetic aperture source.

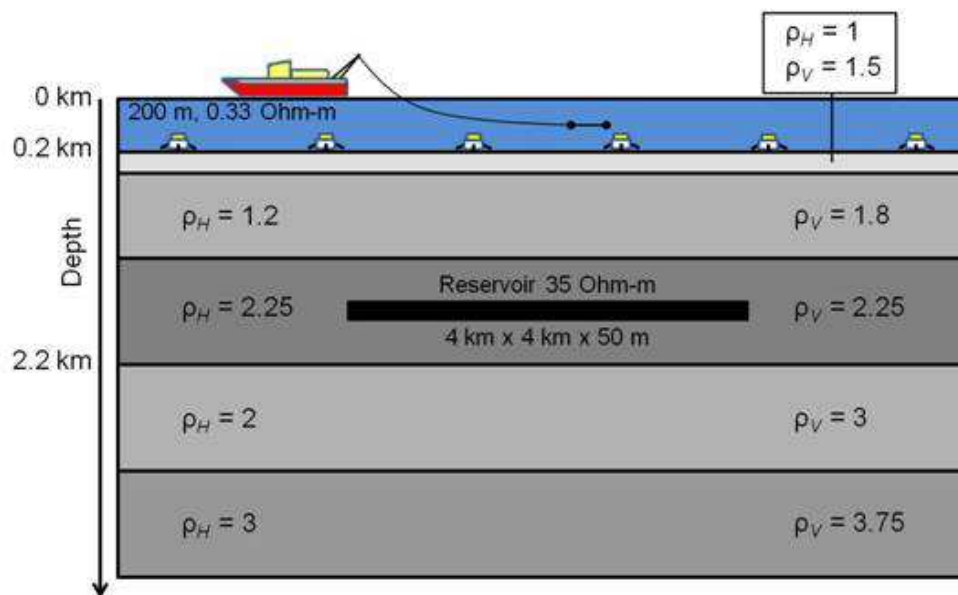


Figure 2.12. Model 3 consisting of 200 m shallow sea water layer with a resistivity of 0.33 ohm-m, and anisotropic layered sea-bottom sediments.

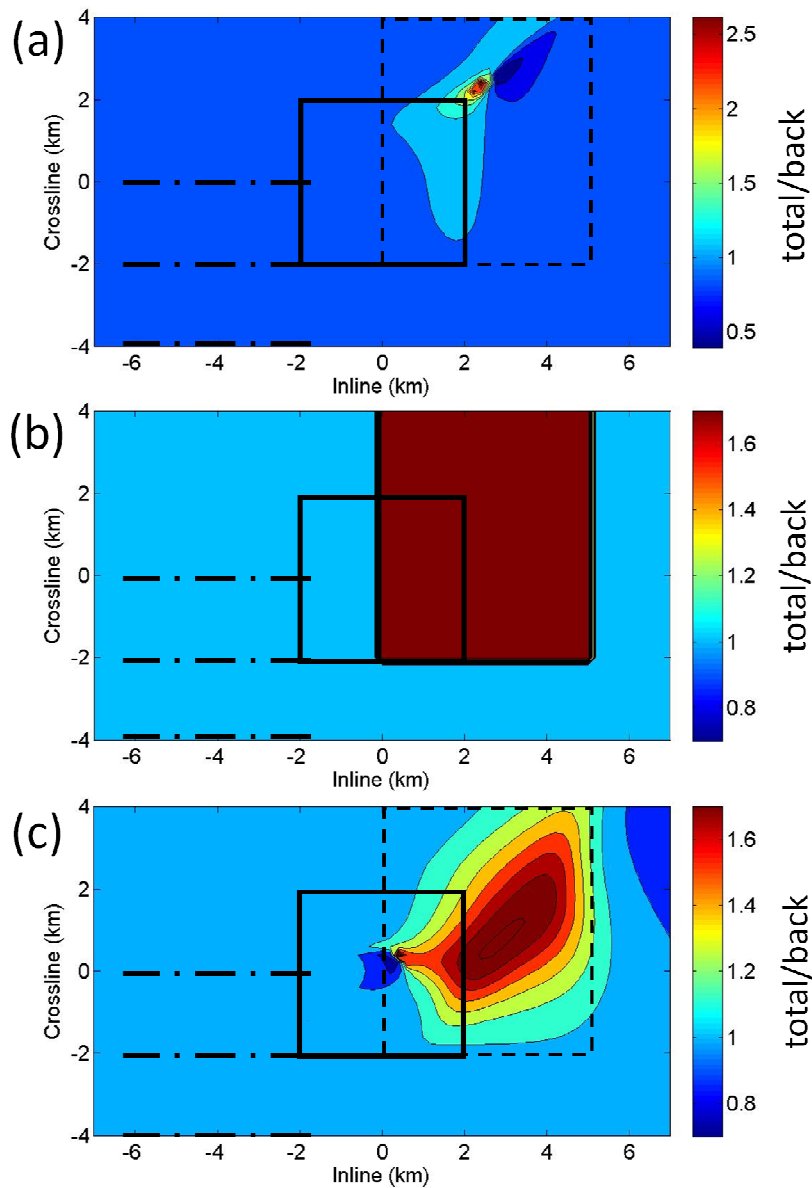


Figure 2.13. Panel a presents the plot of the original normalized data for Model 3. Panel b shows the plot of the designed normalized synthetic aperture in a form of a boxcar function covering the area of the expected reservoir anomaly. Panel c presents the normalized synthetic aperture data produced by the optimal synthetic aperture method.



Figure 2.14. The Harding oil and gas field is located in the UK sector of the North Sea, about 320 km northeast of Aberdeen.

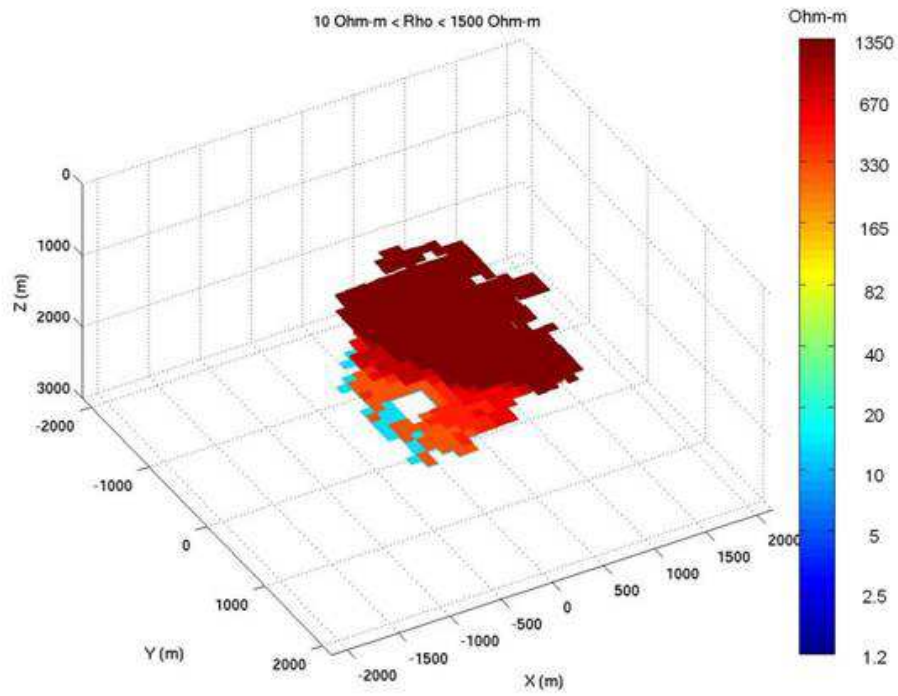


Figure 2.15. 3D resistivity model of the Harding oil and gas field.

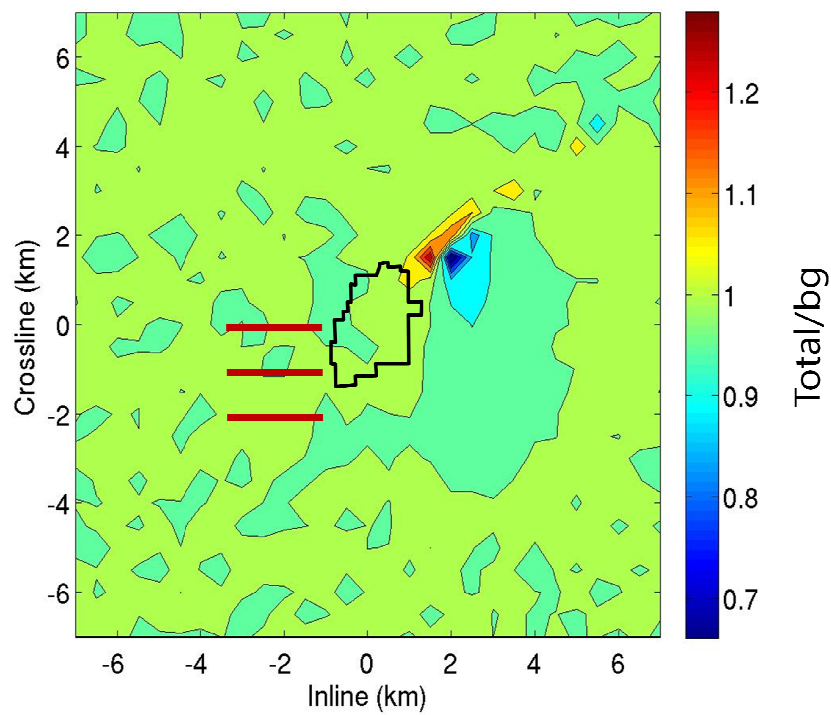


Figure 2.16. The plot of the original normalized data for Harding field model. Red lines indicate a synthetic aperture source and black line present the footprint of the HC reservoir.

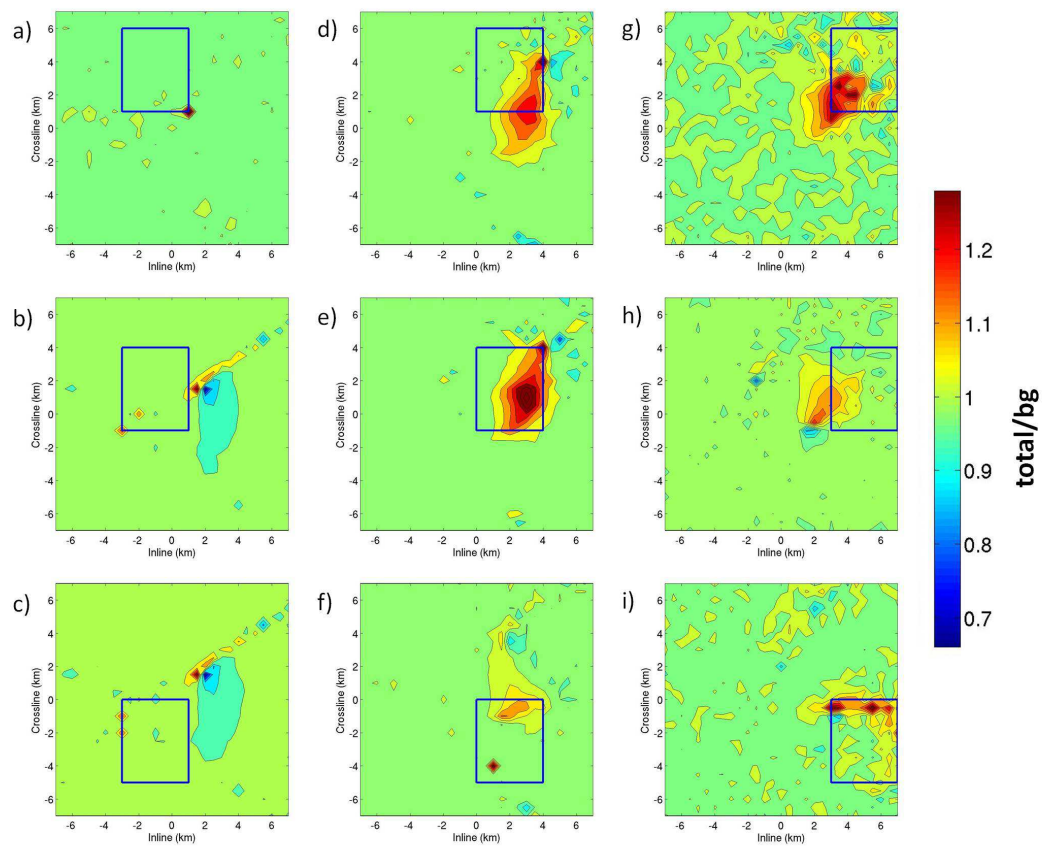


Figure 2.17. Optimal synthetic aperture results by scanning scheme with moving window.

CHAPTER 3

OPTIMAL SYNTHETIC APERTURE METHOD FOR TOWED STREAMER EM SURVEYS

3.1 Introduction

Marine electromagnetic (EM) methods have found wide application in off-shore hydrocarbon (HC) exploration because of their sensitivity to the resistive targets associated with the HC reservoirs (e.g., Constable, 2010; Hesthammer et al., 2010). With the recent development of the towed streamer EM technique by PGS, the marine EM surveys can be applied to rapidly explore large areas to study the sea-bottom resistivity (e.g., Engelmark et al., 2012; Mckay et al., 2015). However, the interpretation of the multitransmitter and multireceiver EM data typical for the towed streamer surveys is a very challenging problem, which usually requires a large scale inversion of the observed data. In this situation, it is desirable to develop a rapid imaging technique of the towed streamer EM data for reconnaissance surveying of vast areas of the shelf. I propose using for this purpose a concept of synthetic aperture (SA) which has been widely used for processing and imaging the radiofrequency electromagnetic and acoustic waves recorded by radars and sonars. It is based on the idea that a virtual source constructed by different actual sources with specific radiation patterns can steer the interfered fields to

the direction of an area of interest (DeGraaf, 1998; Cheney, 2001; Cetin and Karl, 2001; Korobov et al., 2010). A similar approach has been introduced to diffusive EM fields (Fan et al., 2010, 2012, Knaak et al., 2013), where the authors applied the SA method to MCSEM surveys by constructing a SA source with different transmitters to steer the generated fields toward the direction of the target, so that it can enhance the EM anomaly caused by the target.

Another approach to achieving this goal has been introduced in Yoon and Zhdanov (2011) and Zhdanov (2013), where the authors increased the sensitivity of the EM response to the target using the concept of focusing controlled sensitivity by selecting the appropriate combination of the data weights.

In papers by Yoon and Zhdanov (2014, 2015), the authors have demonstrated that the sensitivity of the MCSEM survey to a specific geological target could be enhanced by selecting the appropriate amplitude and phase coefficients of the corresponding synthetic aperture. A concept of optimal SA was introduced based on finding the optimal data weights of the SA for the MCSEM data, which enhance the EM anomaly from a target in the deep or shallow marine environment.

I should note that, all previous development of the SA method for marine EM data was focused on the conventional MCSEM survey configuration with the fixed nodes sea-bottom receivers and moving transmitters. In this chapter, I develop the optimal SA method for the towed streamer EM survey data. With the synthetic and case studies, I demonstrate that this method increases the EM response from the potential sea-bottom targets significantly, which can be effectively used in the reconnaissance surveys for finding the horizontal locations of the HC reservoirs.

3.2 Virtual Receivers

The towed streamer EM surveys are conceptually similar to marine CSEM surveys in the sense of the towing transmitter in the marine system. However, the former consists of a set of receivers towed by a vessel while the latter deploys receivers at the sea floor. It means, in the latter system, the receiver positions are the same for all the different transmitter shots, but in the former system, the receiver positions by one transmitter shot are different from those by the other shots. The fundamental idea of the SA method is that the signals generated at different source positions are measured at the same receiver positions, so that they can be integrated to increase the potential anomaly. Unlike the conventional MCSEM system, the towed streamer system consists of a set of towed receivers which can measure a signal generated at a certain transmitter position only. In order to integrate the signals generated by different sources at the same receiver positions in the towed streamer EM system, I have to interpolate the fields from each source to the virtual receiver positions, which can be shared by all the transmitter shots.

Consider a typical Towed Streamer EM survey, formed by a set of towed receivers with transmitter-receiver offset index, $s = 1, 2, \dots, S$. A long bipole transmitter generates a low-frequency EM field from the points with coordinates $\tilde{\mathbf{r}}_j, j = 1, 2, \dots, J$. The data recorded at the receivers by a transmitter at point $\tilde{\mathbf{r}}_j$ can be denoted by a vector-column,

$$\mathbf{d}_j = \left[d_j^{(1)}, d_j^{(2)}, \dots, d_j^{(S)} \right]^T \quad (3.1)$$

where $d_j^{(s)}$ is the datum observed at offset, s , from the transmitter located at point $\tilde{\mathbf{r}}_j$.

In marine environment, the measured electric field decays quickly with the increase of the distance (offset) between the transmitter and the receiver, which makes it difficult

to detect the anomaly related to the target reservoir. In order to overcome this problem, the observed data are usually normalized by the amplitude of the background field data as follows:

$$d_j^{N(s)} = d_j^{(s)} / |d_j^{b(s)}|, \quad (3.2)$$

where $d_j^{(s)}$ and $d_j^{b(s)}$ describe the total and background field data, respectively, recorded at offset, s , from the transmitter located at point $\tilde{\mathbf{r}}_j$.

The background field is determined as a field generated by a given transmitter in some background geoelectrical model, which is usually selected as a horizontally layered model (Zhdanov, 2009). There are different ways to determine the background field. One can be based on 1D inversion of the observed data. Another one uses the reference field in the observation point far enough from the prospective reservoir. Indeed, if one knows that some measurements are made outside the location of the expected target, these data can be considered as a background (reference) field,

$$\mathbf{d}^b = [d_j^{(1)}, d_j^{(2)}, \dots, d_j^{(s)}]^T = [d_{ref}^{(1)}, d_{ref}^{(2)}, \dots, d_{ref}^{(s)}]^T, \text{ref} \in j = 1, 2, \dots, J. \quad (3.3)$$

Then equation (3.2) can be represented as follows:

$$d_j^{N(s)} = d_j^{(s)} / |d_{ref}^{(s)}|. \quad (3.4)$$

The normalized data recorded at the receivers by a transmitter at point $\tilde{\mathbf{r}}_j$ can be denoted by a vector-column,

$$\mathbf{d}_j^N = [d_j^{N(1)}, d_j^{N(2)}, \dots, d_j^{N(S)}]^T. \quad (3.5)$$

3.3 Introducing Synthetic Aperture Data for Towed Streamer EM survey

In order to apply the optimal SA method, I first determine the positions of the virtual receivers to be shared by all the transmitters. For simplicity, consider all actual receiver positions for all transmitters as the virtual receiver positions. If I assume there are no exactly overlapped receiver positions by different sources in the original data, The coordinates of the virtual receiver positions are denoted as follows: \mathbf{r}_l , $l = 1, 2, \dots, L$, where $L = JS$. The normalized observed data are then interpolated into the virtual receiver positions, forming a $[L \times 1]$ vector-column,

$$\mathbf{d}_j^N = [d_j^{N(1)}, d_j^{N(2)}, \dots, d_j^{N(L)}]^T. \quad (3.6)$$

Note that, the values $d_j^{N(l)}$ corresponding to the range exceeding the maximum offset from the corresponding transmitter, $\tilde{\mathbf{r}}_j$, are set to be 1 (a unit) because the normalized data are equal 1 everywhere outside the anomaly.

Combining all the normalized data for all transmitters, I obtain a $[JL \times 1]$ vector-column of the data recorded in both the actual and virtual receivers,

$$\mathbf{d}^N = [\mathbf{d}^{N(1)}, \mathbf{d}^{N(2)}, \mathbf{d}^{N(3)}, \dots, \mathbf{d}^{N(L)}]^T, \quad (3.7)$$

where $\mathbf{d}^{N(l)}$ is a $[J \times 1]$ vector-column of the normalized data set at the receiver position,

\mathbf{r}_l ,

$$\mathbf{d}^{N(l)} = [d_1^{N(l)}, d_2^{N(l)}, \dots, d_J^{N(l)}]^T. \quad (3.8)$$

As shown in Chapter 2, the SA data can be calculated as a linear combination of the responses for all the transmitters:

$$\mathbf{d}_A = \mathbf{W}_A \mathbf{d}^N, \quad (3.9)$$

where \mathbf{d}_A is an $[L \times 1]$ vector-column of the SA data based on the normalized observed data,

$$\mathbf{d}_A = [d_A^{(1)}, d_A^{(2)}, d_A^{(3)}, \dots, d_A^{(L)}]^T, \quad (3.10)$$

and \mathbf{W}_A is a $[L \times JL]$ block-diagonal rectangular matrix of the weights,

$$\mathbf{W}_A = \begin{bmatrix} \mathbf{w}^T & 0 \dots & 0 \dots & 0 \dots \\ 0 \dots & \mathbf{w}^T & 0 \dots & 0 \dots \\ 0 \dots & 0 \dots & \ddots & 0 \dots \\ 0 \dots & 0 \dots & 0 \dots & \mathbf{w}^T \end{bmatrix}. \quad (3.11)$$

In the last formula, \mathbf{w} is a $[J \times 1]$ vector-column of the corresponding synthetic aperture weights, w_j ,

$$\mathbf{w} = [w_1, w_2, \dots, w_J]^T. \quad (3.12)$$

The goal is to find the optimal values of the weights, w_j , and would enhance the EM anomalies from the targets.

3.4 Definition of the Optimal Synthetic Aperture Method for Towed Streamer EM Survey

The towed streamer EM system measures the in-line component of the electric field, E , (Engelmark et al., 2012; McKay et al., 2015). In this case, following Yoon and Zhdanov (2015), I can write equation (3.7) as follows:

$$\mathbf{d}_A = \begin{bmatrix} E_1^{N(1)} & E_2^{N(1)} & \dots & E_J^{N(1)} \\ E_1^{N(2)} & E_2^{N(2)} & \dots & E_J^{N(2)} \\ \vdots & \vdots & \ddots & \vdots \\ E_1^{N(L)} & E_2^{N(L)} & \dots & E_J^{N(L)} \end{bmatrix} \begin{bmatrix} w_1 \\ w_2 \\ \vdots \\ w_J \end{bmatrix} = \mathbf{E}^N \mathbf{w}, \quad (3.13)$$

where

$$E_j^{N(l)} = E_j^{(l)} / |E_j^{b(l)}|, \quad (3.14)$$

and $E_j^{b(l)}$ is the background electric field and \mathbf{E}^N is a $[L \times J]$ matrix of rearranged normalized observed in-line components of electric fields, $E_j^{N(l)}$, recorded by a virtual receiver at point \mathbf{r}_l for a transmitter, $\tilde{\mathbf{r}}_j$, and \mathbf{w} is the synthetic aperture weights in equation (3.12), and \mathbf{d}_A is an $[L \times 1]$ vector-column,

$$\mathbf{d}_A = [d_A^{(1)}, d_A^{(2)}, d_A^{(3)}, \dots, d_A^{(L)}]^T. \quad (3.15)$$

By analogy with (3.13), the synthetic aperture response for the normalized background electric field can be expressed as follows:

$$\mathbf{d}_B = \begin{bmatrix} E_1^{Nb(1)} & E_2^{Nb(1)} & \dots & E_J^{Nb(1)} \\ E_1^{Nb(2)} & E_2^{Nb(2)} & \dots & E_J^{Nb(2)} \\ \vdots & \vdots & \ddots & \vdots \\ E_1^{Nb(L)} & E_2^{Nb(L)} & \dots & E_J^{Nb(L)} \end{bmatrix} \begin{bmatrix} w_1 \\ w_2 \\ \vdots \\ w_J \end{bmatrix} = \mathbf{E}^{Nb} \mathbf{w}, \quad (3.16)$$

where

$$E_j^{Nb(l)} = E_j^{b(l)} / |E_j^{b(l)}|, \quad (3.17)$$

and \mathbf{E}^{Nb} is an $[L \times J]$ matrix of rearranged normalized background electric fields, and \mathbf{d}_B is an $[L \times 1]$ vector-column,

$$\mathbf{d}_B = [d_B^{(1)}, d_B^{(2)}, d_B^{(3)}, \dots, d_B^{(L)}]^T. \quad (3.18)$$

I also introduce vector-column, \mathbf{d}_R of the ratio between the SA data and the SA response for the normalized background electric field:

$$\mathbf{d}_R = \left[\frac{d_A^{(1)}}{d_B^{(1)}}, \frac{d_A^{(2)}}{d_B^{(2)}}, \dots, \frac{d_A^{(L)}}{d_B^{(L)}} \right]^T = \mathbf{A}(\mathbf{w}), \quad (3.19)$$

where

$$d_A^{(l)} / d_B^{(l)} = \left[\sum_{j=1}^J E_j^{N(l)} w_j \right] / \left[\sum_{j=1}^J E_j^{Nb(l)} w_j \right]. \quad (3.20)$$

and \mathbf{A} is a forward operator for the normalized synthetic aperture data \mathbf{d}_R , which is a function of the synthetic aperture weights \mathbf{w} . Note that, if all the SA weights \mathbf{w} are equal to 1, then according to Yoon and Zhdanov (2015), the corresponding data \mathbf{d}_R are called

the *SA data without steering*. The \mathbf{d}_R computed based on the optimal SA weights, are called *optimal SA data*.

Based on the system equation (3.19), I determine the optimal synthetic aperture weights by solving minimization problem for the following objective functional:

$$P(\mathbf{w}) = \|\mathbf{D} - \mathbf{A}(\mathbf{w})\|^2 + \alpha \|\mathbf{w} - \mathbf{w}_{\text{apr}}\|^2 = \min, \quad (3.21)$$

where \mathbf{D} is a so-called *designed synthetic aperture (DSA)*, α is a regularization parameter, and \mathbf{w}_{apr} is an a priori vector-column of the data weights, which, for simplicity, can be selected as follows: $\mathbf{w}_{\text{apr}} = [1, 1, \dots, 1]^T$. The selection of the DSA (\mathbf{D}) is discussed in the next section. The minimization problem of equation (3.21) is solved based on regularized conjugate gradient method as follows (Zhdanov, 2002):

$$\mathbf{r}_n = \mathbf{A}(\mathbf{w}_n) - \mathbf{D}, \quad (3.22)$$

$$\mathbf{l}_n = \mathbf{F}_n^T \mathbf{r}_n + \alpha(\mathbf{w}_n - \mathbf{w}_{\text{apr}}), \quad (3.23)$$

$$\beta_n = \|\mathbf{l}_n\|^2 / \|\mathbf{l}_{n-1}\|^2, \quad (3.24)$$

$$\hat{\mathbf{l}}_n = \mathbf{l}_n + \beta_n \hat{\mathbf{l}}_{n-1}, \quad \hat{\mathbf{l}}_0 = \mathbf{l}_0, \quad (3.25)$$

$$k_n = (\hat{\mathbf{l}}_n^T \mathbf{l}_n) / (\|\mathbf{F}_n \hat{\mathbf{l}}_n\|^2 + \alpha \|\hat{\mathbf{l}}_n\|^2), \quad (3.26)$$

$$\mathbf{w}_{n+1} = \mathbf{w}_n - k_n \hat{\mathbf{l}}_n, \quad (3.27)$$

where \mathbf{F}_n is the Fréchet derivative matrix of the operator \mathbf{A} at iteration n , which is calculated based on perturbation method, and \mathbf{w}_{apr} is some a priori estimate of the data weights.

3.5 Synthetic Model Study

3.5.1 Selection of a Designed Normalized Synthetic Aperture Data

The designed synthetic aperture, DSA, according to its name, is selected (designed) with the purpose of enhancing the EM anomalies from the potential targets. I should note that different selections of the DSA for the optimal SA method can result in different optimal SA weights. In this section, I discuss how the different DSAs affect the results and make the recommendations on their selections.

Consider a geoelectrical model consisting of 300 m seawater layer with a resistivity of 0.33 Ohm-m, and 1 Ohm-m half space of sediment. A reservoir with sizes of 4 km x 4 km x 200 m is located at a depth of 800 m below the sea floor, and the resistivity of the reservoir is 100 Ohm-m (Figure 3.1). The towed streamer EM survey consists of one survey line, running in the x direction at $y = 0$. The horizontal electric dipole transmitter oriented in the x direction with a moment of 1 Am is towed from 20 km to -20 km in the x direction at a depth of 10 m below the sea surface. Sixty receivers with offsets between 900 m and 7720 m are towed at a depth of 100 m and measure inline electric fields at a frequency of 0.4 Hz.

In order to apply the optimal SA method, I construct a SA source using all the transmitter points on the survey line, and select the background (reference) field as the observed data generated by the very first transmitter located at $x=20$ km. Figure 3.2 shows the plots of the normalized SA data without steering (black lines). I have considered four different designed synthetic apertures in order to demonstrate how they affect the optimal SA data. I first select a boxcar function as the designed SA, setting the maximum value equal to 1.3 within the area of the expected reservoir anomaly and to 1

outside of the targeted zone. Then I move the boxcar function along the axis x , as shown in panels a-c of Figure 3.2. Panel a demonstrates that if there is no anomalous field within the area of the maximum of the boxcar function, the optimal SA method does not generate any false anomaly. Panels b and c indicate that the boxcar function has to fully cover the area of the anomalous field, otherwise only the anomalous fields inside of the boxcar area increase. Lastly, I use a constant value for the designed synthetic aperture. As demonstrated in Chapter 2, the optimal SA method increases or decreases the SA data only within the area where the true anomaly exists. Therefore, one can simply use a constant value for the designed synthetic aperture in order to enhance the responses from all potential targets. Panel d presents a plot of the optimal SA data (red line) obtained using a uniform synthetic aperture (blue line). One can see that the optimal SA data shown in panels c and d are practically identical. This result illustrates the fact that the uniform SA can be successfully used in the reconnaissance towed streamer EM survey, where the location of the potential target is not a priori known.

3.5.2 A Model with Near-Sea-floor Inhomogeneities

In this section, I consider a complex model, which consists of two thin reservoirs and near-sea-floor inhomogeneities. Model 2 consists of 300 m seawater with a resistivity of 0.33 Ohm-m, and five conductive sediment layers as shown in Figure 3.3. The first top sediment layer with a thickness of 200 m represents the near-sea-floor inhomogeneities, with resistivities varying randomly from 1 to 4 Ohm-m. The resistivities of the second sediment layer and below including the bottom half space are 3, 2, 5, and 4 Ohm-m, respectively. The reservoirs have the same size of 4 km x 4 km x 200 m but they are

located at different depths of 1100 m (the left reservoir) and 800 m (the right reservoir) below the sea surface, with resistivities of 50 Ohm-m and 100 Ohm-m, respectively, as shown in Figure 3.3. The separation between the reservoirs is 4 km in the x direction. The EM survey configuration is the same as that considered in Model 2. The data were contaminated with the random 5 % Gaussian noise.

As was done above for Model 1, I first construct a SA source using all the transmitters in the survey line, and select the background (reference) field as the observed data generated by the very first transmitter located at $x=20$ km. Then, I plot the normalized SA data without steering as shown by the black line in panel a of Figure 3.4. In this complex model, the SA data without steering are distorted due to the near-surface inhomogeneities and the noise in the observed data, which makes it difficult to determine the locations of the targets from the anomalous responses in the plot of the SA data without steering.

As discussed in the previous section, I select a uniform designed synthetic aperture shown by a blue line in panel a of Figure 3.4. After applying the optimal SA method to the observed data, I have generated optimal SA data shown by the red line. One can see that the anomalies of the SA data increased over the reservoirs, while the magnitude of the data elsewhere remains practically the same as for the SA data without steering. Lastly, to clearly see the increased anomalies only, I plot the ratio between the optimal SA data and the SA data without steering in panel b of Figure 3.4. As one can see the areas of the increased anomalies agree well with the true horizontal locations of the targets (black bars in panel b of Figure 3.4).

3.6 Application of the Optimal Synthetic Aperture Method to the Towed Streamer EM Data Collected in the Troll West Oil and Gas Province

I have applied the optimal SA method to the towed streamer EM data collected in the Troll West Oil and Gas Provinces. These data were studied in papers Zhdanov et al. (2014a), Zhdanov et al. (2014b), where a rigorous 3D inversion was conducted for these data, which makes them a suitable dataset for testing the optimal SA method.

The towed streamer EM data used in the numerical study were collected at seven survey lines at a frequency of 0.496 Hz. Figure 3.5 shows the seven survey lines over the true locations of Troll West Oil Province (TWOP) and Troll West Gas Province (TWGP). The 8700 m long EM streamer was towed at a depth of 10 m below the sea surface. Eleven receivers with offsets between 1860 and 7554 m were selected, which were towed at 100 m below the sea surface.

I have applied the optimal SA method to the data collected along each line. The reference field was selected using a set of the observed data generated by the first transmitter located on the left of line #1, assuming that field was less affected by the anomalous resistivity of the Troll oil and gas fields. This reference field was used as the background fields for all the towed streamer EM data collected at all seven lines. Then I calculated the normalized SA data without steering. As an example, Figure 3.6 shows the SA data without steering along line #1. As one can see, it is not trivial to distinguish the anomalous responses from the targets in this plot.

To apply the optimal SA method to the Troll data, I first selected the uniform designed synthetic aperture with a constant value of 1.5. Figure 3.6 shows the plots of the

normalized SA data without steering (black lines) and the optimal SA data (red lines) along the different lines of the towed streamer survey. As one can see, the optimal SA method increases the observed anomalies of the SA data significantly. Figure 3.7, panel a, represents a map of the ratio between the optimal and the normalized SA data without steering. Panel b in the same figure shows a horizontal section of 3D inversion of the same data (but recorded at five different frequencies) at a depth of 1475 m (panel b in Figure 3.8). As one can see, this map agrees very well with the true horizontal locations of hydrocarbon (HC) reservoirs of the TWOP and TWGP. This case study demonstrates a remarkable effectiveness of the optimal SA method to find the horizontal locations of the targets without any inversion. Another advantage of this method is a very short computation time. I have computed the optimal SA data using a PC with Intel Core i7, 32 GB, and 2.5 GHz, and the computation time was less than a few seconds, while a rigorous 3D inversion requires several hours or even days of computation on a PC cluster. Note that the computation time mostly depends on the number of data point, which was about 40,000 in this case. Thus, the optimal SA method can be considered as an effective technique for real time scanning of the survey area for potential HC reservoirs using the EM data.

3.7 Conclusions

I have introduced a novel method of fast imaging the towed streamer EM data based on the concept of optimal synthetic aperture. It has been shown that this method increases the EM response from the potential sea-bottom HC reservoirs significantly. Two numerical studies and a case study have demonstrated the effectiveness of the optimal SA

method in mapping the sea-bottom resistive targets (e.g., HC reservoirs). The method is extremely fast with the computational time on a standard PC of less than a few seconds for large survey data (up to 40,000 observation points). The developed innovative technique can be used as a fast data processing technique for real time evaluation of the data collected by a reconnaissance towed streamer EM survey with the goal of scanning vast area of marine shelf.

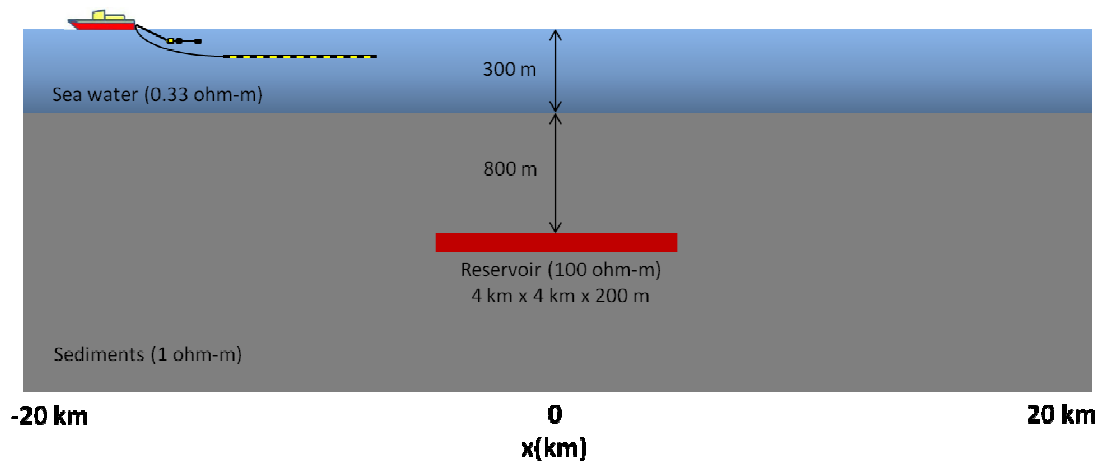


Figure 3.1. Sketch of Model 1

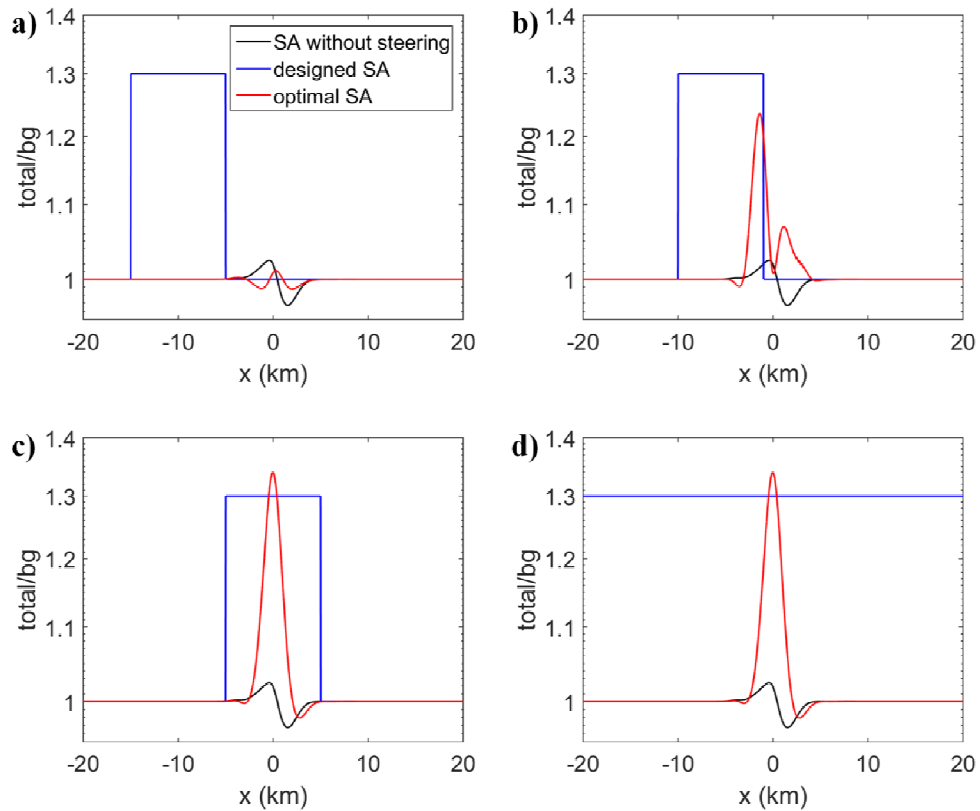


Figure 3.2. Model 1. The results of optimal SA method for different selections of the designed synthetic apertures. Panels a, b, and c present the plots of the conventional, without steering SA data (black lines) and optimal SA data (red lines) obtained using a boxcar function with different locations (blue lines) as a designed synthetic aperture. Panel d shows a plot of the optimal SA data (red line) obtained using a uniform synthetic aperture (blue line).

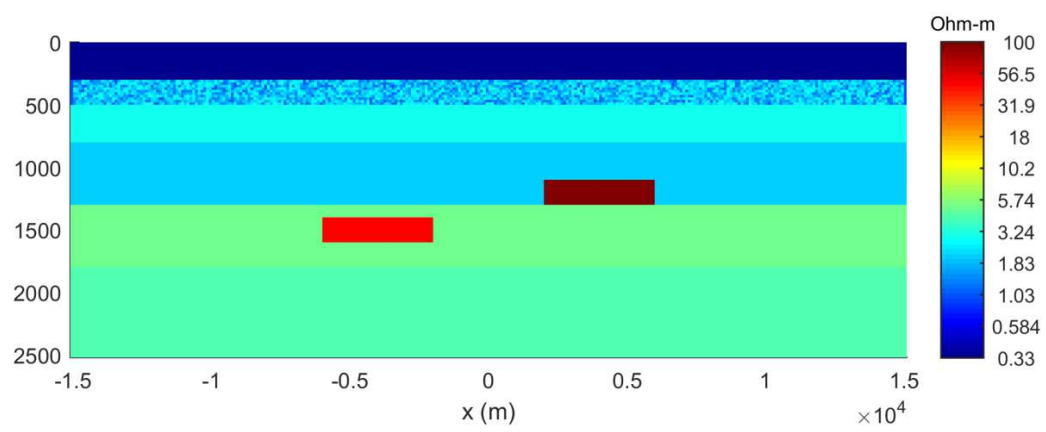


Figure 3.3. Sketch of Model 2

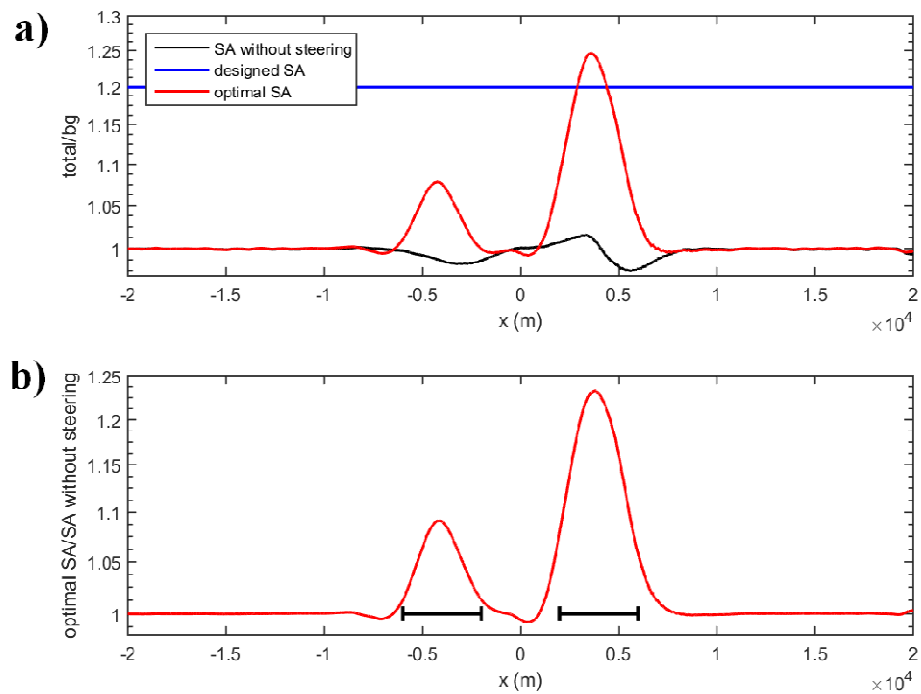


Figure 3.4. Model 2. Panel a shows the normalized SA data without steering (black line), designed synthetic aperture (blue line), and optimal SA data (red line). Panel b presents the plot of the ratio between the optimal SA data and that without steering (red line); the horizontal locations of the reservoirs are shown by the black segments.

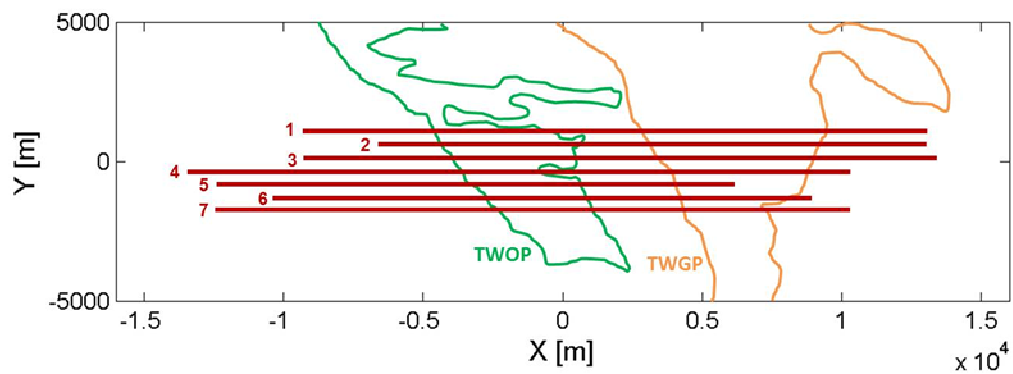


Figure 3.5. The configuration of the towed streamer EM survey conducted in the Troll West Oil and Gas Provinces. The red lines show the locations of the seven survey lines.

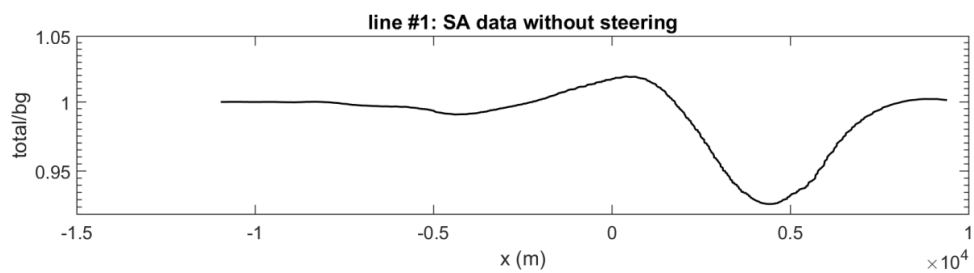


Figure 3.6. The normalized synthetic aperture data without steering of line #1.

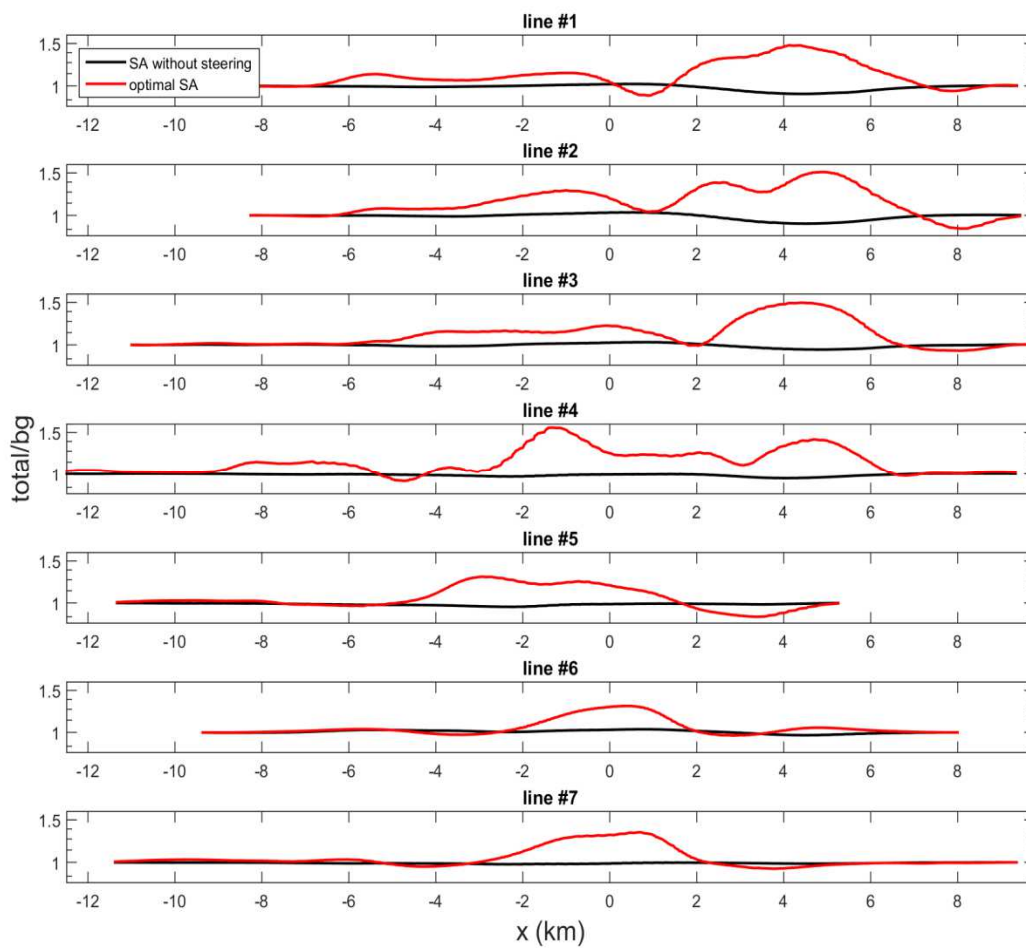


Figure 3.7. Plots of the normalized synthetic aperture data without steering (black) and the results of optimal synthetic aperture method (red) from line #1 to line #7.

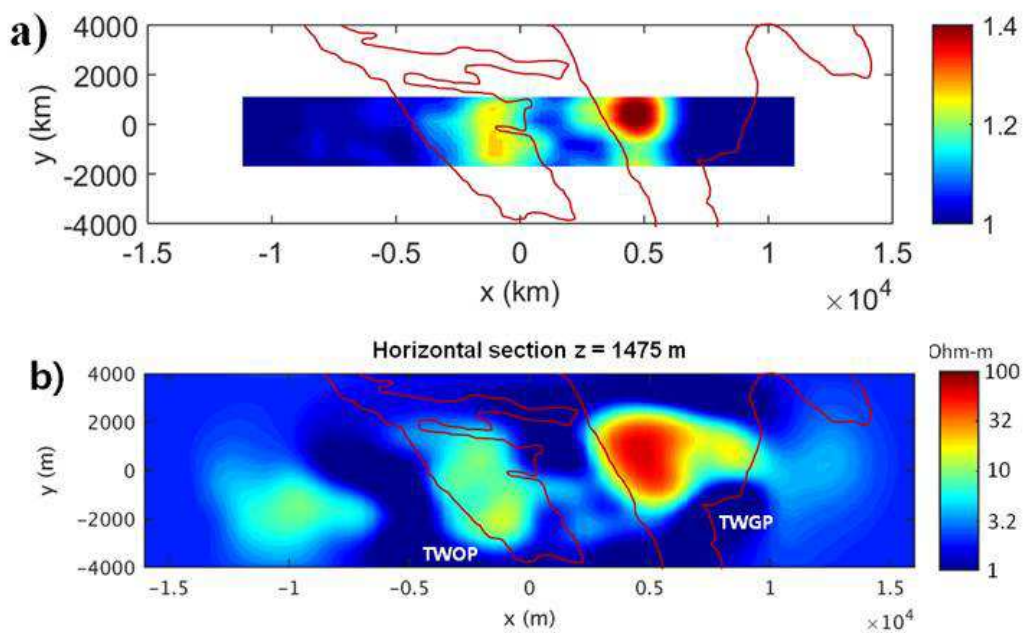


Figure 3.8. Panel a shows a map of the ratio between the optimal and the normalized SA data without steering. Panel b shows a horizontal section of 3D inversion of the same data (but recorded at five different frequencies) at a depth of 1475 m presented in Chapter 5.

CHAPTER 4

HYBRID FINITE DIFFERENCE AND INTEGRAL EQUATION METHOD FOR EM MODELING

4.1 Introduction

The main engine for improvement in the interpretation of geophysical electromagnetic (EM) survey data is the continuing development of efficient algorithms for 3D EM modeling. There are several popular numerical approaches for 3D EM modeling: integral equation (IE), finite difference (FD), and finite element (FE) methods (Zhdanov, 2002, 2009, 2015; Avdeev, 2005).

The IE method represents one of the most effective numerical solvers for localized anomalous structures embedded in a layered earth. One of the advantages of the IE method is that it only requires a solution within the anomalous domain, and the electric and magnetic fields at the receivers are calculated based on the Green's tensor approach. The IE modeling domain includes inhomogeneous geoelectrical structures only and it is typically very small compared to the modeling domains of the differential equation (DE) methods, which require a large computational domain to satisfy to the corresponding boundary conditions. At the same time, the system matrix of the IE method is dense, so if the complexity of the model grows, the IE method requires significantly larger amount of computational memory and time. I should note, however, that many novel approaches

have been applied to the conventional IE method to overcome those computational difficulties, including the contraction IE method, variable background conductivity, and efficient Green's tensor calculations (e.g., Hursán and Zhdanov, 2002; Zhdanov et al., 2006; Endo et al., 2008; Zhdanov, 2009; Avdeev and Knizhnik, 2009).

The advantage of the DE method is the sparsity of the system matrices, which improves the condition number and enables us to use a direct solver very efficiently. Direct solvers have traditionally been considered to be computationally too demanding for 3D problems compared to iterative solvers. However, gradual advancement of direct-solution algorithms, along with the availability of resources for parallel computation makes it possible to apply these algorithms for solving large-scale 3D problems very efficiently (Streich, 2009; da Silva et al., 2012; Yang and Oldenburg, 2012; Grayver et al., 2013; Schwarzbach and Haber, 2013; Jaysaval et al., 2014). Especially, in the case of multisource problem such as marine CSEM, the direct solvers may perform more efficiently than the iterative solvers because the direct solvers reuse the decomposed system matrix for multiple sources whereas the iterative solvers need to solve the problem for each source separately (Chung et al., 2014). However, the DE methods require a very large computational domain and extensive mesh refinement in the vicinity of the receivers and/or sources to reduce errors caused by the interpolation and numerical differentiation required to calculate the electric and magnetic fields in the receivers. To avoid mesh refinement and/or numerical errors, Cox and Zhdanov (2014a) applied the Green's tensor approach to the finite element (FE) method to calculate magnetic fields and their sensitivities at the receivers, and developed a 3D airborne EM inversion based on their hybrid FE-IE method. In this chapter, I use a concept similar to the Green's

tensor approach, and apply it to the FD method.

I have developed a hybrid FD-IE method, which combines the advantages of those two methods. In the framework of this approach, the FD modeling algorithm is based on the staggered grid (Yee, 1966) and follows the approach outlined in Newman and Alumbaugh (1995). Once the unknown electric fields in the computation domain of the FD method are computed, the electric and magnetic fields at the receivers are calculated using the IE method with the corresponding Green's tensor for the background conductivity model. This approach makes it possible to compute the fields at the receivers accurately without the need of very fine FD discretization in the vicinity of the receivers and transmitters and without the need for numerical differentiation and interpolation.

To verify the accuracy and the efficiency of the developed method, I compare the fields computed by the hybrid FD-IE method with those computed by the conventional FD method, the 1D semianalytical solution, and the 3D IE method.

4.2 Finite Difference Modeling of the Anomalous Electric Field

The implementation of the FD method developed in this paper follows that of Newman and Alumbaugh (1995) and Alumbaugh et al. (1996). The method solves Maxwell's equations in the frequency domain based on a finite-difference scheme on a staggered grid and uses the anomalous field formulation with the total field being decomposed into background, \mathbf{E}^b , and anomalous, \mathbf{E}^a , fields. The calculation of the anomalous field with an equivalent source makes it possible to avoid the discretization problems associated with discrete sources. This approach has been widely used in the EM

modeling literature, whether with FD, finite-volume, finite-element, or IE methods (e.g., Zhdanov, 2002, 2009).

For the low frequency EM fields, considered in geophysical applications, the displacement currents can be ignored in Maxwell's equations, which results in the second-order differential equation for the anomalous electric field, \mathbf{E}^a :

$$\nabla \times \nabla \times \mathbf{E}^a + i\omega\mu_0\boldsymbol{\sigma}\mathbf{E}^a = -i\omega\mu_0(\boldsymbol{\sigma} - \boldsymbol{\sigma}^b)\mathbf{E}^b. \quad (4.1)$$

The magnetic permeability within the earth, μ , is assumed to be constant, $\mu_0 = 4\pi \times 10^{-7}$ H/m, and the total, $\boldsymbol{\sigma}$, and background, $\boldsymbol{\sigma}^b$, conductivity tensors are considered to be diagonal, composed of the principal components of the conductivity tensor. The electric fields are assigned to the edges of the cells in the staggered grid. For simplicity, I use the Dirichlet boundary condition, i.e., the anomalous electric field is set to zero at all sides of the computational domain.

A finite-difference representation of equation (4.1) on a staggered grid can be written as a linear system of equations as follows:

$$\mathbf{K}\mathbf{e} = \mathbf{R}, \quad (4.2)$$

where \mathbf{e} is the unknown vector of the anomalous electric field, and \mathbf{R} is a vector containing the source terms. The matrix \mathbf{K} is a sparse and symmetric complex matrix composed of real numbers except for the diagonal elements. I use multifrontal massively parallel sparse direct solver, MUMPS (Amestoy et al., 2001, 2006), to solve the system of equation (4.2), which enables an efficient solution of large-scale problems with

multiple sources.

4.3 Integral Equation Method for Computing the EM Field at the Receivers

In the integral equation method, the electric and magnetic fields at the receiver positions are computed based on the Green's tensor approach, which does not require any meshes near receiver positions. The anomalous electric and magnetic fields at the receiver position, $\mathbf{r}_l, l = 1, 2, \dots, L$, can be expressed as an integral over the excess currents in the inhomogeneous domain D :

$$\mathbf{E}^a(\mathbf{r}_l) = \iiint_D \widehat{\mathbf{G}}_E(\mathbf{r}_l | \mathbf{r}) \Delta \boldsymbol{\sigma}(\mathbf{r}) \cdot [\mathbf{E}^b(\mathbf{r}) + \mathbf{E}^a(\mathbf{r})] dV \quad (4.3)$$

$$\mathbf{H}^a(\mathbf{r}_l) = \iiint_D \widehat{\mathbf{G}}_H(\mathbf{r}_l | \mathbf{r}) \Delta \boldsymbol{\sigma}(\mathbf{r}) \cdot [\mathbf{E}^b(\mathbf{r}) + \mathbf{E}^a(\mathbf{r})] dV \quad (4.4)$$

where $\widehat{\mathbf{G}}_E(\mathbf{r}_l | \mathbf{r})$ and $\widehat{\mathbf{G}}_H(\mathbf{r}_l | \mathbf{r})$ are the electric and magnetic Green's tensors defined for an unbounded conductive medium with the background (horizontally layered) anisotropic conductivity, $\boldsymbol{\sigma}^b$; the anomalous domain D represents a volume with the anisotropic anomalous conductivity distribution, $\Delta \boldsymbol{\sigma}(\mathbf{r}) = \boldsymbol{\sigma}(\mathbf{r}) - \boldsymbol{\sigma}^b(\mathbf{r})$.

In the case of three-directional anisotropic conductivity, equation (4.3) can be simplified using matrix notations as follows (Hursán and Zhdanov, 2002):

$$\mathbf{E}^a = \widehat{\mathbf{G}}^E \Delta \boldsymbol{\sigma} \mathbf{E} \quad (4.5)$$

where \mathbf{E}^a is a $3L \times 1$ vector-column of x , y , and z components of anomalous electric fields

at the receiver positions, $r_l, l = 1, 2, \dots, L$,

$$\mathbf{E}^a = \left[E_{x,1}^a, \dots, E_{x,L}^a, E_{y,1}^a, \dots, E_{y,L}^a, E_{z,1}^a, \dots, E_{z,L}^a \right]^T, \quad (4.6)$$

and \mathbf{E} is a $3N \times 1$ vector-column of electric fields at the centers of the cells within the inhomogeneous domain, D :

$$\mathbf{E} = \left[E_{x(1,1,1)}, \dots, E_{x(N_x, N_y, N_z)}, E_{y(1,1,1)}, \dots, E_{y(N_x, N_y, N_z)}, E_{z(1,1,1)}, \dots, E_{z(N_x, N_y, N_z)} \right]^T \quad (4.7)$$

where the main node (i, j, k) is defined as a location of the center of the cells in the inhomogeneous domain, D , and the total number of cells in domain D is denoted as $N = N_x \times N_y \times N_z$.

Matrix $\widehat{\mathbf{G}}^E$ is a $3L \times 3N$ rectangular matrix containing the integrals of the electric Green's tensors,

$$\widehat{\mathbf{G}}^E = \begin{bmatrix} \mathbf{G}_{xx}^E & \mathbf{G}_{xy}^E & \mathbf{G}_{xz}^E \\ \mathbf{G}_{yx}^E & \mathbf{G}_{yy}^E & \mathbf{G}_{yz}^E \\ \mathbf{G}_{zx}^E & \mathbf{G}_{zy}^E & \mathbf{G}_{zz}^E \end{bmatrix}, \quad (4.8)$$

$$\mathbf{G}_{\alpha\beta}^E = \begin{bmatrix} \Gamma_{\alpha\beta}^{1(1,1,1)} & \dots & \Gamma_{\alpha\beta}^{1(N_x, N_y, N_z)} \\ \vdots & \ddots & \vdots \\ \Gamma_{\alpha\beta}^{L(1,1,1)} & \dots & \Gamma_{\alpha\beta}^{L(N_x, N_y, N_z)} \end{bmatrix}, \alpha, \beta = x, y, z, \quad (4.9)$$

$$\Gamma_{\alpha\beta}^{l(i,j,k)} = \iiint_{D(i,j,k)} G_{\alpha\beta}^E(r_l | r_{(i,j,k)}) dv, \quad (4.10)$$

where $G_{\alpha\beta}^E(r_l | r_{(i,j,k)})$, $\alpha = x, y, z$, are the components of an electric Green's tensors; $\Delta\sigma$ is a $3N \times 3N$ diagonal matrix with anomalous conductivities,

$$\Delta\sigma = \text{diag}([\Delta\sigma_{x(1,1,1)}, \dots, \Delta\sigma_{x(N_x, N_y, N_z)}, \Delta\sigma_{y(1,1,1)}, \dots, \Delta\sigma_{y(N_x, N_y, N_z)}, \Delta\sigma_{z(1,1,1)}, \dots, \Delta\sigma_{z(N_x, N_y, N_z)}]). \quad (4.11)$$

4.4 Formulation of a Hybrid Finite Difference and Integral Equation

Method

The conventional FD method requires an interpolation to calculate the electric fields at the receivers, a numerical approximation of the curl of the electric field, and an interpolation to calculate the magnetic fields at the receivers. Such numerical differentiations and interpolations can cause some numerical errors, and require mesh refinement in the vicinity of the receivers to reduce the errors. In order to avoid those problems, I use an IE approach, described in the previous section, to calculate the electric and magnetic fields at the receivers.

In the Green's tensor approach described in the previous section, vector $r_{(i,j,k)}$ in equation (4.10) is located at the center of the cell where the electric field is computed using the IE method. However, in the framework of the FD scheme based on the staggered grid, the electric fields are calculated at the edges of the cells. Therefore, in order to apply the IE formulation in equation (4.3) to the FD scheme on the staggered grid, equation (4.5) should be modified accordingly as follows:

$$\mathbf{E}^a = \widehat{\mathbf{G}}^E [\Delta\boldsymbol{\sigma}' \mathbf{E}'] \quad (4.12)$$

where "prime" indicates that the components of all matrices in equation (4.12) are given at the midpoints of the edges of the corresponding staggered grid.

In discrete form, I define the main node (i, j, k) to be located at the center of the cells in the inhomogeneous domain, D , and denote the total number of cells in domain D as follows: $N = N_x \times N_y \times N_z$. The total number of edges of the cells is calculated as follows: $N^e = N_x^e + N_y^e + N_z^e$, where $N_x^e = N_x \times (N_y + 1) \times (N_z + 1)$, $N_y^e = (N_x + 1) \times N_y \times (N_z + 1)$, and $N_z^e = (N_x + 1) \times (N_y + 1) \times N_z$.

Matrix $\Delta\boldsymbol{\sigma}'$ in equation (4.12) is a $N^e \times N^e$ diagonal matrix of the weighted averaging anomalous conductivities, defined in Appendix A,

$$\Delta\boldsymbol{\sigma}' = \text{diag}([\Delta\boldsymbol{\sigma}_{x(1, \frac{1}{2}, \frac{1}{2})}, \dots, \Delta\boldsymbol{\sigma}_{x(N_x, N_y + \frac{1}{2}, N_z + \frac{1}{2})}, \Delta\boldsymbol{\sigma}_{y(\frac{1}{2}, 1, \frac{1}{2})}, \dots, \Delta\boldsymbol{\sigma}_{y(N_x + \frac{1}{2}, N_y, N_z + \frac{1}{2})}, \Delta\boldsymbol{\sigma}_{z(\frac{1}{2}, \frac{1}{2}, 1)}, \dots, \Delta\boldsymbol{\sigma}_{z(N_x + \frac{1}{2}, N_y + \frac{1}{2}, N_z)}]). \quad (4.13)$$

Vector \mathbf{E}' is a $N^e \times 1$ vector-column of electric fields within the inhomogeneous domain, D ,

$$\mathbf{E}' = [\mathbf{E}_{x(1, \frac{1}{2}, \frac{1}{2})}, \dots, \mathbf{E}_{x(N_x, N_y + \frac{1}{2}, N_z + \frac{1}{2})}, \mathbf{E}_{y(\frac{1}{2}, 1, \frac{1}{2})}, \dots, \mathbf{E}_{y(N_x + \frac{1}{2}, N_y, N_z + \frac{1}{2})}, \mathbf{E}_{z(\frac{1}{2}, \frac{1}{2}, 1)}, \dots, \mathbf{E}_{z(N_x + \frac{1}{2}, N_y + \frac{1}{2}, N_z)}]^T. \quad (4.14)$$

Matrix $\widehat{\mathbf{G}}^E$ is a $3L \times N^e$ rectangular matrix containing the integrals of the electric Green's tensors, defined according to the following formula:

$$\widehat{\mathbf{G}}^E = \begin{bmatrix} \mathbf{G}_{xx}^E & \mathbf{G}_{xy}^E & \mathbf{G}_{xz}^E \\ \mathbf{G}_{yx}^E & \mathbf{G}_{yy}^E & \mathbf{G}_{yz}^E \\ \mathbf{G}_{zx}^E & \mathbf{G}_{zy}^E & \mathbf{G}_{zz}^E \end{bmatrix}. \quad (4.15)$$

In the last formula $\mathbf{G}_{\alpha x}^E$ is a $L \times N_x^e$ matrix,

$$\mathbf{G}_{\alpha x}^E = \begin{bmatrix} \Gamma_{\alpha x}^{l\left(\frac{1}{2}, \frac{1}{2}\right)} & \dots & \Gamma_{\alpha x}^{l\left(N_x, N_y + \frac{1}{2}, N_z + \frac{1}{2}\right)} \\ \vdots & \ddots & \vdots \\ \Gamma_{\alpha x}^{L\left(\frac{1}{2}, \frac{1}{2}\right)} & \dots & \Gamma_{\alpha x}^{L\left(N_x, N_y + \frac{1}{2}, N_z + \frac{1}{2}\right)} \end{bmatrix}, \quad (4.16)$$

$\mathbf{G}_{\alpha y}^E$ is a $L \times N_y^e$ matrix,

$$\mathbf{G}_{\alpha y}^E = \begin{bmatrix} \Gamma_{\alpha y}^{l\left(\frac{1}{2}, 1, \frac{1}{2}\right)} & \dots & \Gamma_{\alpha y}^{l\left(N_x + \frac{1}{2}, N_y, N_z + \frac{1}{2}\right)} \\ \vdots & \ddots & \vdots \\ \Gamma_{\alpha y}^{L\left(\frac{1}{2}, 1, \frac{1}{2}\right)} & \dots & \Gamma_{\alpha y}^{L\left(N_x + \frac{1}{2}, N_y, N_z + \frac{1}{2}\right)} \end{bmatrix}, \quad (4.17)$$

and $\mathbf{G}_{\alpha z}^E$ is a $L \times N_z^e$ matrix,

$$\mathbf{G}_{\alpha z}^E = \begin{bmatrix} \Gamma_{\alpha z}^{l\left(\frac{1}{2}, \frac{1}{2}, 1\right)} & \dots & \Gamma_{\alpha z}^{l\left(N_x + \frac{1}{2}, N_y + \frac{1}{2}, N_z\right)} \\ \vdots & \ddots & \vdots \\ \Gamma_{\alpha z}^{L\left(\frac{1}{2}, \frac{1}{2}, 1\right)} & \dots & \Gamma_{\alpha z}^{L\left(N_x + \frac{1}{2}, N_y + \frac{1}{2}, N_z\right)} \end{bmatrix}. \quad (4.18)$$

where

$$\Gamma_{\alpha\beta}^{l(i,j,k)} = \iiint_{D_{(i,j,k)}} G_{\alpha\beta}^E(r_l | r_{(i,j,k)}) d\mathbf{v}, \quad (4.19)$$

Magnetic fields at the receiver positions can be calculated in a similar way, by replacing the magnetic Green's tensors in equation (4.19) for the electric Green's tensors.

The hybrid FD-IE method makes it possible to avoid the interpolation and differentiation errors and/or refinement of the grid in the vicinity of the receivers in order to improve the accuracy of the field calculation. Also, the discretization grid outside the inhomogeneous domain can be coarser than for the conventional FD method because the hybrid method requires an accurate solution within the inhomogeneous domain only.

Obviously, the hybrid FD-IE modeling method requires an additional computation of the Green's tensors in comparison with the conventional FD modeling method. However, the Green's tensors used for the field calculation at the receivers are the same as those used for the Fréchet derivative calculation for the EM inversion, which will be described in Chapter 5. Therefore, the precomputed Green's tensor for the field calculation in the receivers can be reused for the Fréchet derivative calculation with practically no extra computation required.

4.5 Verification of the Hybrid FD-IE Modeling Method

In order to verify the accuracy and the efficiency of the hybrid FD-IE forward modeling method, I present several model studies and compare the results by the hybrid FD-IE method with those by three other techniques: a 1D semianalytical solution, a conventional FD method, and a 3D IE method.

4.5.1 Comparison with a Semianalytical Solution

4.5.1.1 Model 1

Model 1 is a horizontally layered geoelectrical model with an isotropic resistive rectangular reservoir (Figure 4.1). The background is a seawater-sediment model with air-earth interface at $z = 0$ m and a seawater depth of 1000 m. The resistivities of air, seawater, and sediments are 10^6 ohm-m, 0.3 ohm-m, and 1 ohm-m, respectively. The electromagnetic field is excited by a horizontal electric dipole oriented in the x direction with a moment of 1 Am and located in the seawater with coordinates (0, 0, 950 m), which is 50 m above the sea floor. The frequency of the current in the transmitting dipole is 1 Hz. The receivers are located 5 m above the sea floor from -3 km to 3 km with 200 m spacing in the x direction and shifted by 50 m in the y direction ($y = -50$ m). An isotropic 3D resistive rectangular reservoir with a resistivity of 100 ohm-m is embedded in the sediments from a depth of 1400 m to 1500 m and with a size of $3 \text{ km} \times 3 \text{ km} \times 100 \text{ m}$ in the x , y , and z directions, respectively, which makes it possible, based on the skin depth for this model, to approximate this reservoir accurately enough by an infinite horizontal resistive layer. The volume of the 3D resistive reservoir is considered as a domain with anomalous conductivity.

To demonstrate the accuracy and efficiency of the developed hybrid FD-IE method over the conventional FD method, I first calculated the EM responses for Model 1 using two different grids (coarse and fine), and the responses were then compared with the 1D semianalytical solution. For both grids, the FD modeling domains were selected as $\{-4\text{km} \leq x, y \leq 4\text{km}; -0.5\text{km} \leq z \leq 3\text{km}\}$, based on the skin depth. The coarse grid consisted of $41 \times 41 \times 25 = 31,775$ cells, with uniform cells of 200 m by 200 m in the x

and y directions, and with logarithmically increasing cell size from the boundaries of the reservoir (anomalous domain) to the boundaries of the FD domain in z direction as shown in the left panel of Figure 4.2. The anomalous domain is discretized using a 200 m x 200 m x 10 m uniform grid. In Figure 4.3 and Figure 4.4 the anomalous electric and magnetic fields computed by the hybrid FD-IE method and FD method are compared to the 1D semianalytical solution based on the Hankel transform (Ward and Hohmann, 1988; Zhdanov and Keller, 1994).

I have calculated the relative errors, e , of the FD modeling results using the following formula:

$$e = \frac{\|\mathbf{E}_{san}^a - \mathbf{E}^a\|}{\|\mathbf{E}_{san}^a\|} \times 100, \quad (4.20)$$

where \mathbf{E}_{san}^a is anomalous electric field based on semianalytical solution, and \mathbf{E}^a is anomalous electric field based on FD and/or hybrid FD-IE solutions.

On this coarse grid, the hybrid FD-IE responses were in a good agreement with the semianalytical solution, showing less than 3% relative errors, whereas the FD responses exhibited large discrepancies.

Next, I gradually increased the number of cells within the same FD modeling domain from the coarse grid, and the grids surrounding the receivers were refined as well, until a grid was found for which the FD response was characterized by relative errors similar to those produced by the hybrid FDIE method on the coarse grid. The fine grid, which was finally determined by this process, consisted of $81 \times 61 \times 52 = 256,932$ cells, with 100 m x 100 m uniform grid in the x and y directions, a minimum cell size of 5 m near the receiver positions, and a maximum cell size of 250 m in the z direction, as shown in the

right panel of Figure 4.2. Note that, in order to have the level of errors for the FD responses similar to those for the hybrids FD-IE responses on the coarse grid, I had to refine not only the grid in the vicinity of the receivers, but also the entire grid within the FD domain. I ran the code using 1 node of a cluster with 20 Intel Xeon processors, 64Gbytes, and 2.5GHz. The computation time for the FD method on the coarse grid was approximately 10 s. The hybrid FD-IE method required an additional time for the Green's tensor calculation, and it was approximately 6 s for each components of the electric or magnetic fields. The FD method on the fine grid took approximately 196 s. Therefore, the hybrid FD-IE method is about 10 times faster than the FD method to obtain the responses with a similar error level for this horizontally layered model. I have also computed the fields using the hybrid FD-IE on the fine grid. The corresponding computational time and the relative errors are listed in Table 4.1. One can see that, if the grids are the same, the hybrid FD-IE methods shows smaller relative errors than the FD method.

Next, I calculated the EM responses for Model 1 using several different grids from the coarsest to the finest and with and without the refined meshes near receiver positions. I started with a coarsest grid, discretized with uniform cells of 250 m x 250 m x 125 m. Then, I gradually reduced the cell size to 100 m x 100 m x 50 m. The vertical size of the cells within the anomalous domain was fixed at 25 m for all of the grids. In the case of the refined mesh near receiver positions, the vertical size of the cells equaled 5 m near the receiver positions within a depth interval from 980 m to 1020 m. The anomalous electric and magnetic fields were computed by the conventional FD and hybrid FD-IE methods on different grids with and without mesh refinement near the receiver positions, and the results were compared with the 1D semianalytical solutions. Figure 4.5 presents the plots

of the relative errors versus the total cell numbers for the x and z components of the anomalous electric fields (E_x^a and E_z^a) and the y component of the anomalous magnetic field (H_y^a). As one can see, the hybrid FD-IE method always provides the smaller errors than the conventional FD method for the same discretization grids. Also, the hybrid method provides practically the same responses both with and without the mesh refinement near the receivers, whereas the results of the conventional FD method strongly depend on the mesh refinement, especially for the E_z^a and H_y^a fields.

4.5.1.2 Model 2

Model 2 represents a horizontally layered model with an anisotropic resistive reservoir layer embedded in it. The background model and the survey configurations are the same as in Model 1, but the 3D resistive reservoir embedded in the sediment is transversely isotropic with a horizontal resistivity of 10 Ohm-m and a vertical resistivity of 100 Ohm-m. Figure 4.6 and Figure 4.7 present a comparison between the hybrid FD-IE responses for this model and those computed by the 1D semianalytical solution. For all the scalar components of the electromagnetic field, the comparisons between the hybrid FD-IE responses and the 1D semianalytic responses are excellent.

4.5.2 Comparison with a 3D Integral Equation Method

In the next model study, I have simulated the MCSEM response of a 3D reservoir using the hybrid FD-IE scheme and compared the results to those produced by a conventional 3D IE method (Zhdanov et al., 2006).

I first consider a 3D model with an isotropic background and isotropic rectangular

reservoir. The background is the horizontally layered seawater-sediments model, the same as was used in the previous Models 1 and 2. The 3D isotropic reservoir with a resistivity of 100 ohm-m is located 400 m below the sea floor and is centered horizontally at the origin of the Cartesian coordinate system, with horizontal extent of 2 km in the x and y directions, and a thickness of 100 m. The survey configuration is the same as in Models 1 and 2. The FD modeling domain was selected as $[-3 \text{ km} \leq x, y \leq 3 \text{ km}, -500 \text{ m} \leq z \leq 3 \text{ km}]$ based on the skin depth, and it was discretized with nonuniform grid, refined near the reservoir. The reservoir (anomalous domain) was discretized using $100 \text{ m} \times 100 \text{ m} \times 10 \text{ m}$ uniform grid (Figure 4.8 and Figure 4.9).

Figure 4.10 shows a comparisons of the anomalous electric fields computed using the developed hybrid FD-IE method and the conventional IE method. One can see that the hybrid FD-IE method produces practically the same results as those obtained by the IE method.

I consider a 3D model with an anisotropic background and anisotropic 3D rectangular reservoir. The background is a seawater-sediments model consisting of three transverse anisotropic layers. From the first top sediment layer to the bottom half-space, the horizontal resistivities are 1 ohm-m, 2 ohm-m, and 4 ohm-m, and the vertical resistivities are 5 ohm-m, 10 ohm-m, and 7 ohm-m, respectively. The anisotropic resistive reservoir is embedded in the second sediment layer, with a horizontal resistivity of 10 ohm-m and a vertical resistivity of 100 ohm-m (Figure 4.11). The electric dipole oriented in the x direction is located in the seawater with coordinates (0, 0, 950 m), which is 50 m above the sea floor, and the frequency is 1 Hz. The receivers are located 5 m above the sea floor from -3 km to 3 km with 200 m spacing in the x direction. In order to have nonzero

values of all of the scalar components of the electromagnetic field, I have placed the receivers along a profile parallel to the transmitter profile, but shifted them 50 m in the y direction (at $y = -50$ m).

The FD modeling domain was selected as $\{-3\text{km} \leq x, y \leq 3\text{km}; -0.5\text{km} \leq z \leq 3\text{km}\}$ based on the skin depth, and it was discretized with a nonuniform grid, refined near the reservoir only, not near the receivers. The reservoir (anomalous domain) was discretized using a 100 m x 100 m x 10 m uniform grid.

In order to demonstrate the accuracy and efficiency of the developed hybrid FD-IE method for 3D forward modeling, I have compared the FD-IE results with those calculated using a 3D IE method (Zhdanov et al., 2006). The PIE3D IE code is based on the parallel implementation of the contraction integral equation (CIE) method, and the system of the CIE equations is solved using an iterative solver, the complex generalized minimal residual (CGMRES) method (Zhdanov, 2002, 2009).

In the framework of the IE method, I discretized the anomalous domain using the same cell size as those used within the anomalous domain in the hybrid FD-IE method. Both the IE and hybrid FD-IE codes were run on one node of a cluster with 20 Intel Xeon processors, 64 Gbytes, and 2.5 GHz. Figure 4.12 shows a comparison between the anomalous electric fields computed using the developed hybrid FD-IE method and the original IE method. One can see that the hybrid FD-IE method produces practically the same results as those obtained by the IE method.

I have also compared the computation times for both methods. The computations required by the both methods can be divided into two stages: 1) electric field calculation within the anomalous domain by solving the corresponding systems of linear equations,

and 2) calculation of the electric field at the receiver positions using the integral formulas in equation 3. Note that stage 2 is similar for the both methods. Therefore, I have only compared the computation times required for the first stage, which involves solving the corresponding systems of linear equations for the electric field within the anomalous domain. The RMS misfits for both methods were set equal to 1^{-10} .

Figure 4.13 shows computation times of solving the corresponding systems of equations for both methods as a function of increasing number of the sources. As one can see, the IE method demonstrates an excellent performance if the number of the sources is relatively small (less than 25). Indeed, for a single source, the iterative solver CGMRES of the IE method took approximately 1.5 sec only, while the direct solver MUMPS of the hybrid FD-IE method required approximately 6.17 sec. However, if the number of sources increases, the computational time of the IE method increases linearly as well. At the same time, the runtime of the hybrid FD-IE method, practically, is not affected by the number of the sources. The reason is that the FD system of equations is solved using a multifrontal massively parallel sparse direct solver, MUMPS. This solver requires most of the computation time for numerical factorization and much less time for the forward and backward substitution, which depends on the number of sources (Chung et al., 2014).

These tests demonstrate that the developed hybrid FD-IE method provides a more accurate solution than the conventional FD method, and, at the same time, is characterized by a better performance than the convention IE method for the multisource data.

4.6 Conclusions

I have developed a novel 3D modeling approach, which combines the advantages of the finite difference (FD) and integral equation (IE) methods. In the framework of this approach, Maxwell's equations for anomalous electric fields are solved using the FD method on a staggered grid. The corresponding system of linear FD equations is solved using a direct solver, MUMPS, which is based on a multifrontal method for LU factorization. After the unknown electric fields are determined in the modeling domain using the FD method, the electric and magnetic fields at the receiver are computed based on the Green's tensor approach. This approach makes it possible to compute the fields at the receivers accurately without the need of very fine FD discretization in the vicinity of the receivers and without the need for numerical differentiation and interpolation. The hybrid FD-IE modeling method was carefully validated by comparing the results with a 1D semianalytical solution, the conventional FD solution and the 3D IE solution. The model studies demonstrate that the hybrid FD-IE modeling method is advantageous over the conventional FD and the IE methods. Comparing with semianalytical solution, it has been verified that the hybrid FD-IE method always provides more accurate solutions than the conventional FD method if the grids are the same for the both methods. Also it has been shown that the hybrid FD-IE method does not require mesh refinements near receiver positions for the accurate solutions. The comparison with the 3D IE methods demonstrates that the hybrid FD-IE method performs better than 3D IE method in the case of multisource data because the hybrid FD-IE method uses a direct solver to solve the FD system, whereas the IE method uses iterative solver.

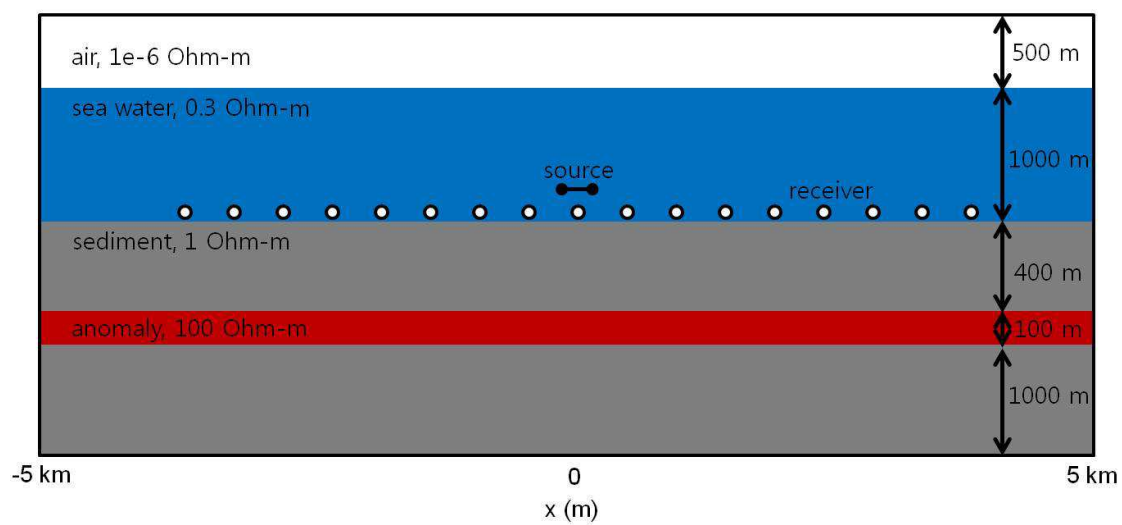


Figure 4.1. Horizontally layered geoelectrical Model 1 with an isotropic reservoir approximated by an infinite horizontal resistive layer.

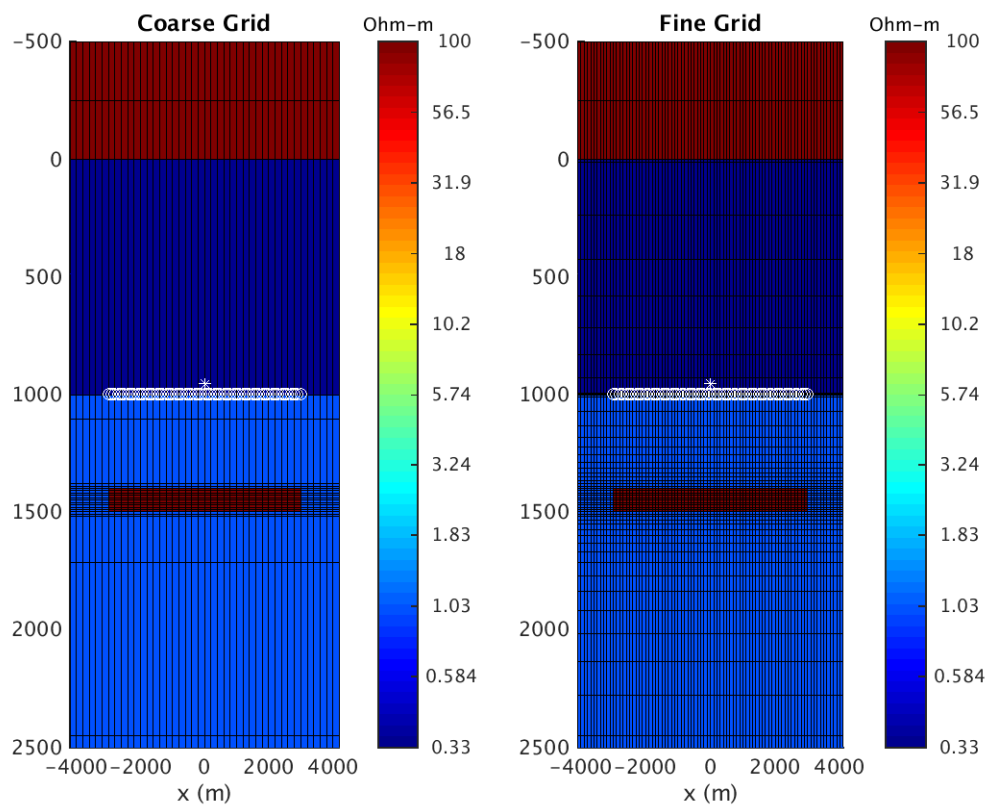


Figure 4.2. Model 1. A horizontally layered geoelectrical model with a coarse grid (left panel) and a fine grid (right panel). The isotropic resistive reservoir layer with a resistivity of 100 ohm-m is embedded in the sediments below the seawater layer. The white star indicates the position of the electrical dipole source, and the white circles denote the receiver positions.

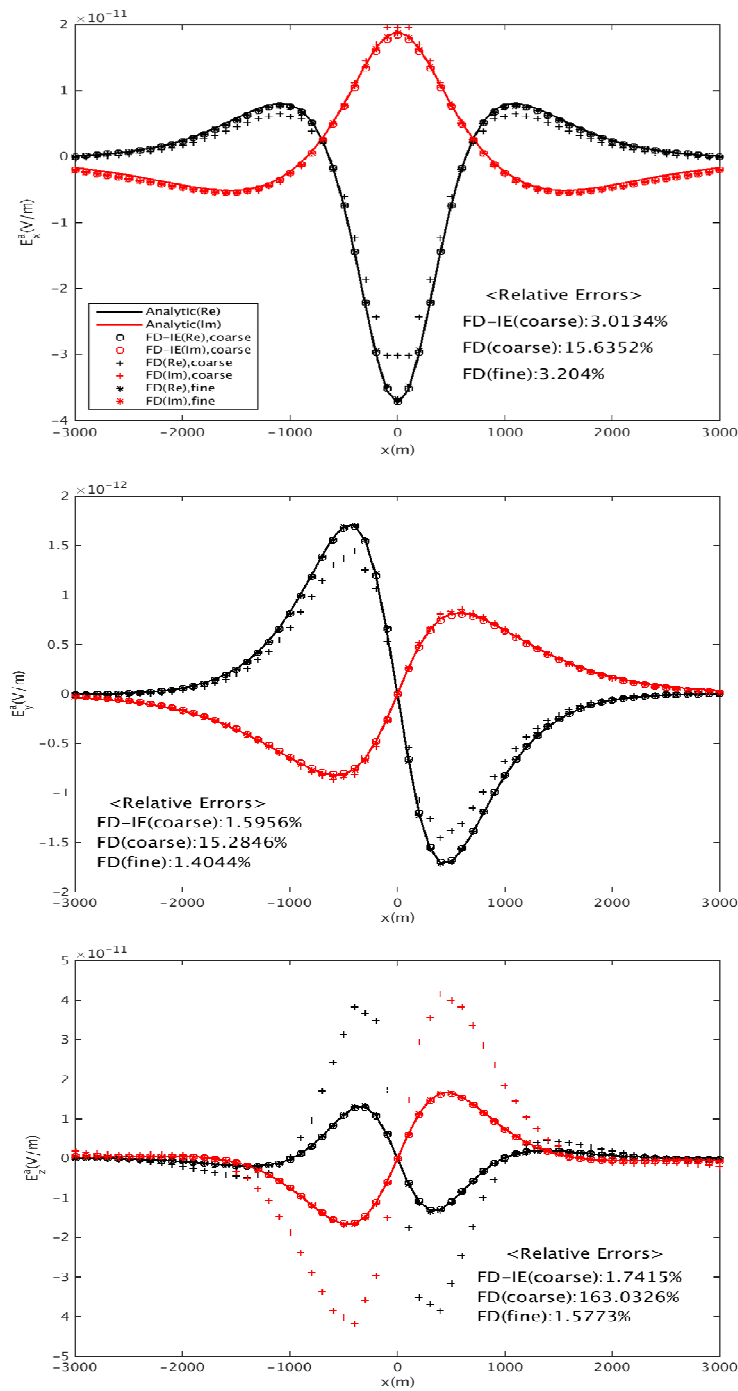


Figure 4.3. Model 1: a comparison of anomalous electric fields computed using the hybrid FD-IE method, the FD method, and an 1D semianalytical solution based on the horizontally layered model with an isotropic resistive reservoir layer. The hybrid FD-IE responses were computed for the model with the coarse grid, while the FD responses were calculated using both the coarse and fine grids. The top, middle, and bottom panels present the x, y, and z components of the anomalous electric field, respectively.

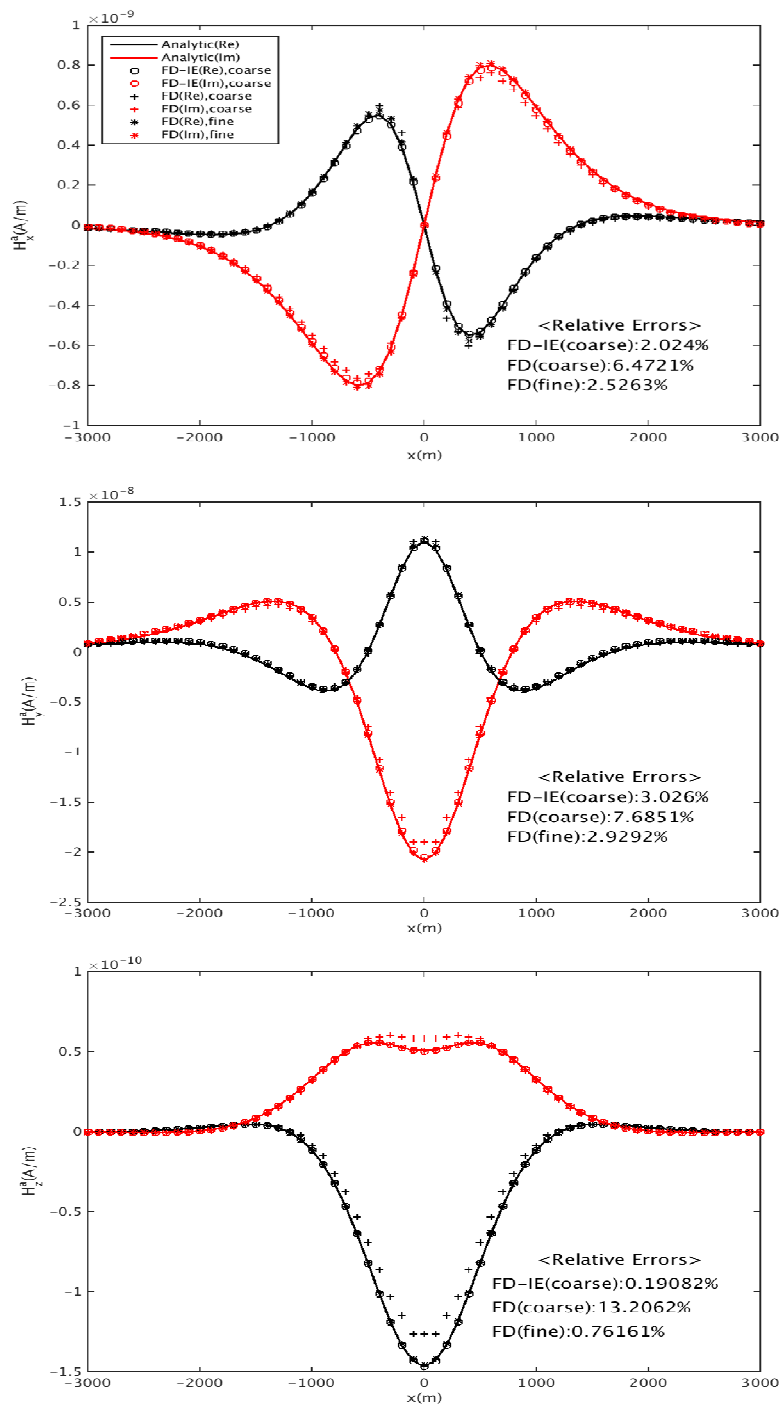


Figure 4.4. Model 1: A comparison of anomalous magnetic fields computed using the hybrid FD-IE method, the FD method, and an 1D semianalytical solution based on the horizontally layered model with an isotropic resistive reservoir layer. The hybrid FD-IE responses were computed for the model with the coarse grid, while the FD responses were calculated using both the coarse and fine grids. The top, middle, and bottom panels present the x, y, and z components of the anomalous magnetic field, respectively.

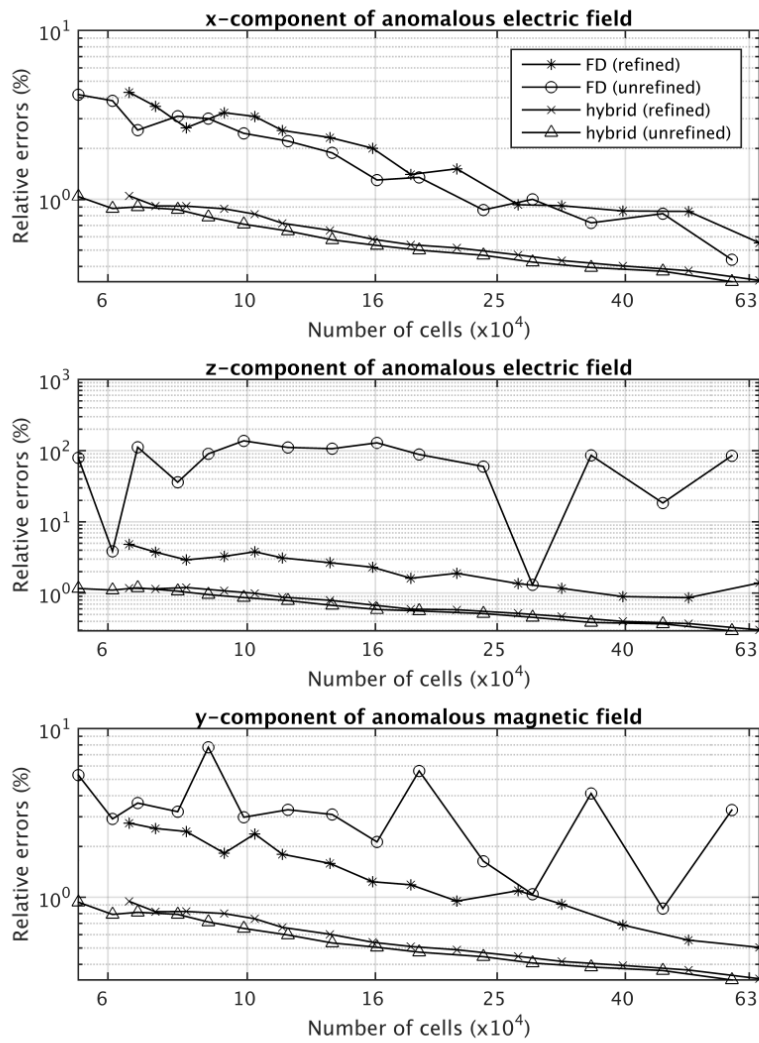


Figure 4.5. Plots of the relative errors vs. the total number of discretization cells between the responses computed using the conventional FD method, hybrid FD-IE method and those obtained by the 1D semianalytical solution. The top, middle, and bottom panels show the relative errors for the x and z components of the anomalous electric field and the y component of the magnetic field, respectively.

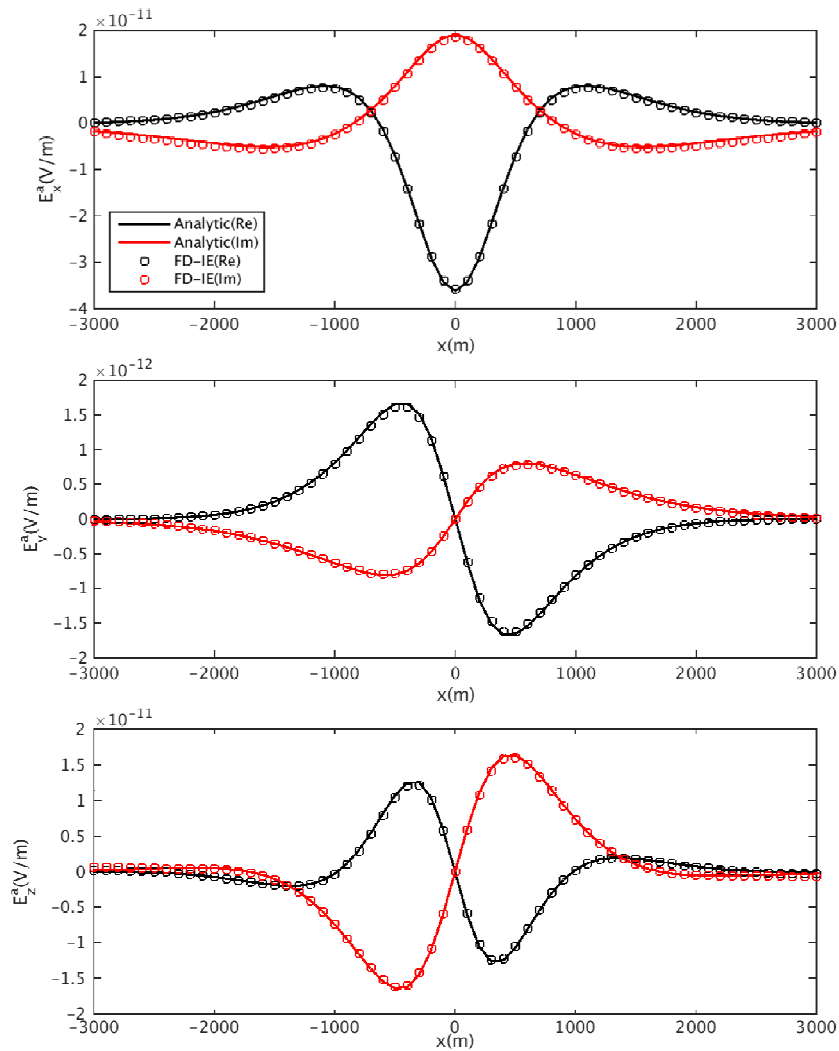


Figure 4.6. Model 2: a comparison of anomalous electric fields computed using the hybrid FD-IE method and an 1D semianalytical solution based on the horizontally layered model with anisotropic resistive reservoir layer. The top, middle, and bottom panels present the x , y , and z components of the anomalous electric field, respectively.

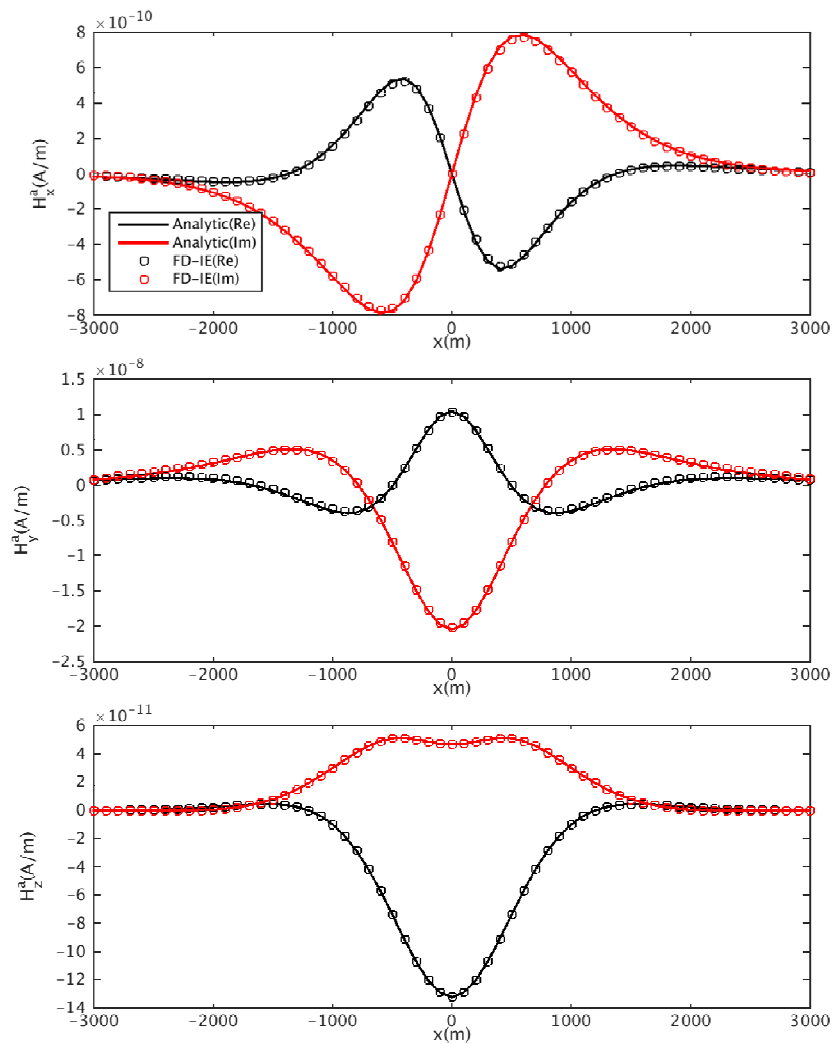


Figure 4.7. Model 2: a comparison of anomalous magnetic fields computed using the hybrid FD-IE method and an 1D semianalytical solution based on the horizontally layered model with anisotropic resistive reservoir layer. The top, middle, and bottom panels present the x, y, and z components of the anomalous magnetic field, respectively.

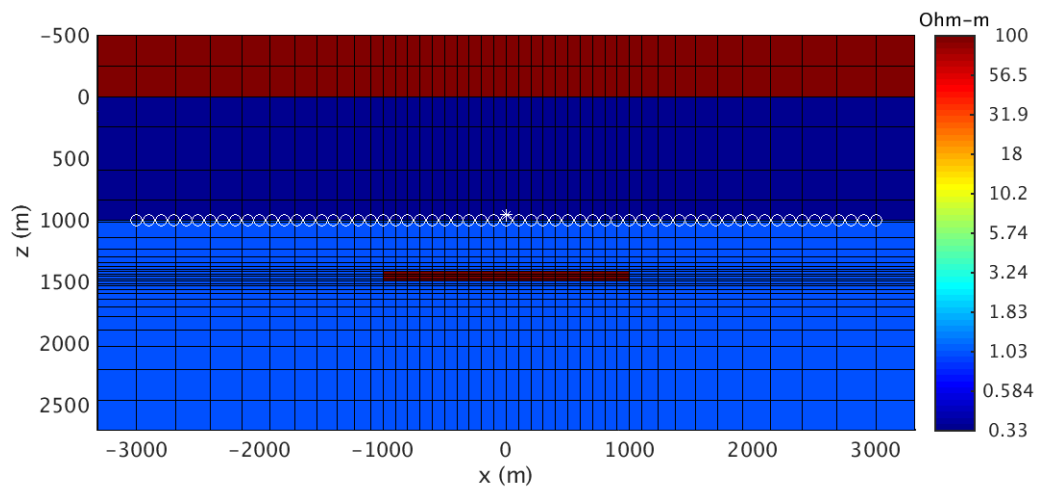


Figure 4.8. Model 3: a vertical section of the resistivity distribution. The white star indicates the electric dipole source position, while the white circles represent the receivers positions.

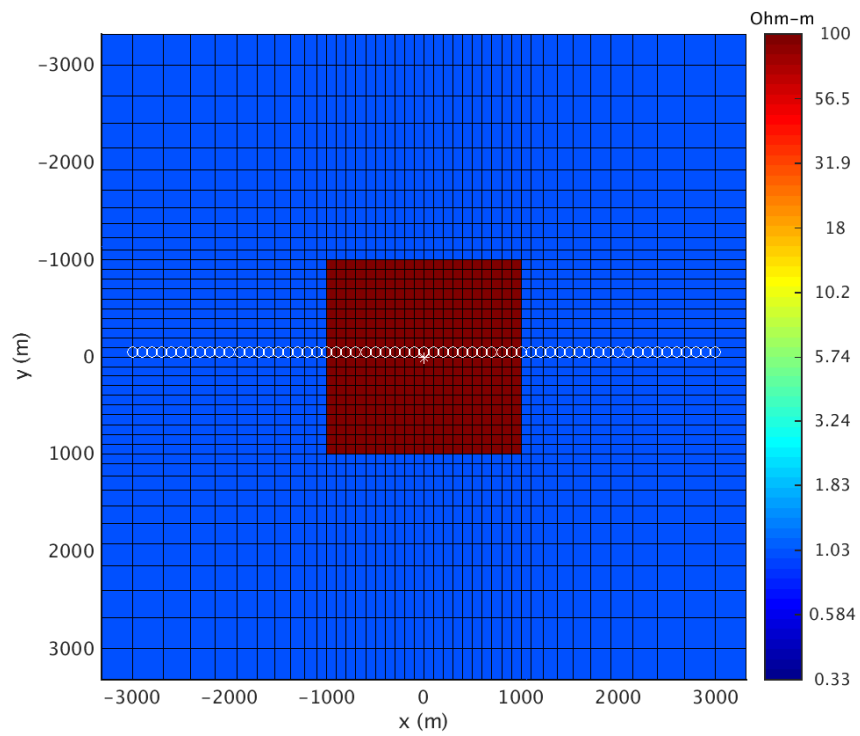


Figure 4.9. Model 3: A horizontal section of the resistivity distribution. The white star indicates the electric dipole source position, while the white circles represent the receivers positions.

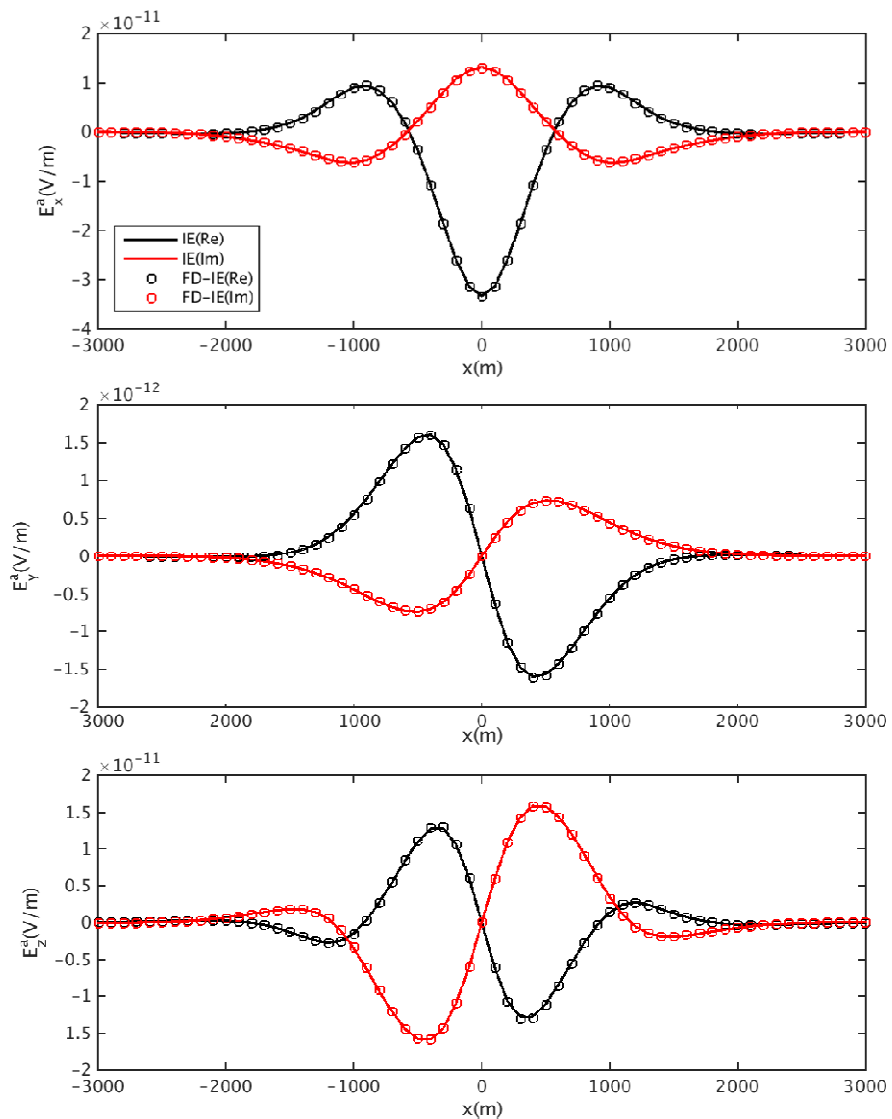


Figure 4.10. Model 3: A comparison of anomalous electric fields computed using the hybrid FD-IE method (solid lines) and the conventional IE method (circles). The top, middle, and bottom panels present the x, y, and z components of the anomalous electric field, respectively.

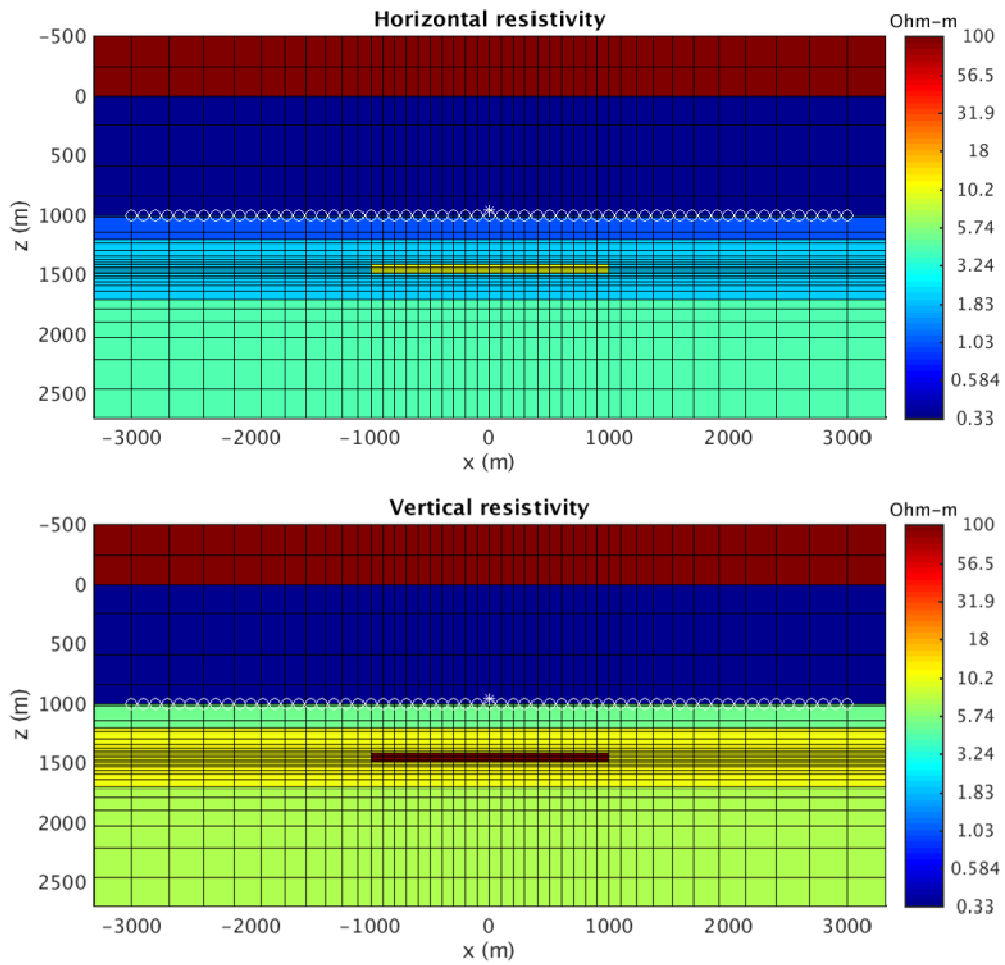


Figure 4.11. Model 2. Vertical sections of the horizontal (top) and the vertical (bottom) resistivity distributions. The white star indicates the electric dipole source position, while the white circles represent the receiver positions.

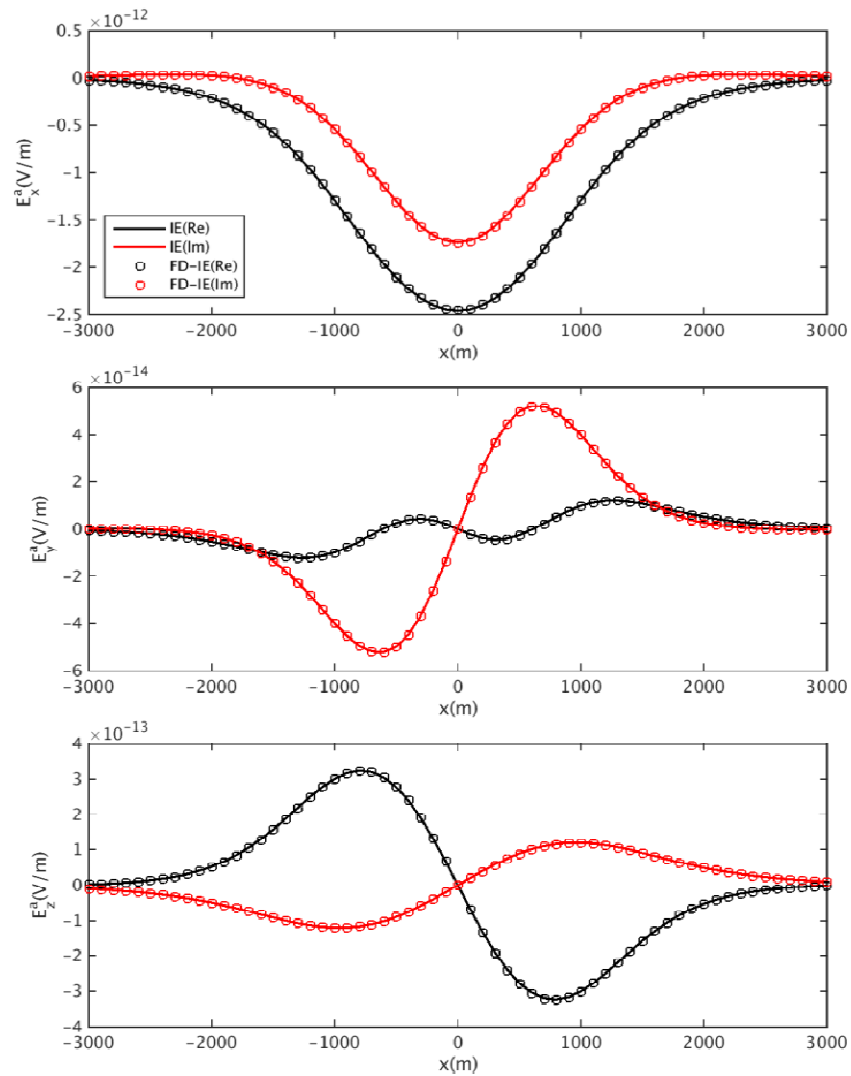


Figure 4.12. Model 2. A comparison of anomalous electric fields computed using the hybrid FD-IE method (circles) and the conventional IE method (solid lines). The top, middle, and bottom panels present the x , y , and z components of the anomalous electric field, respectively.

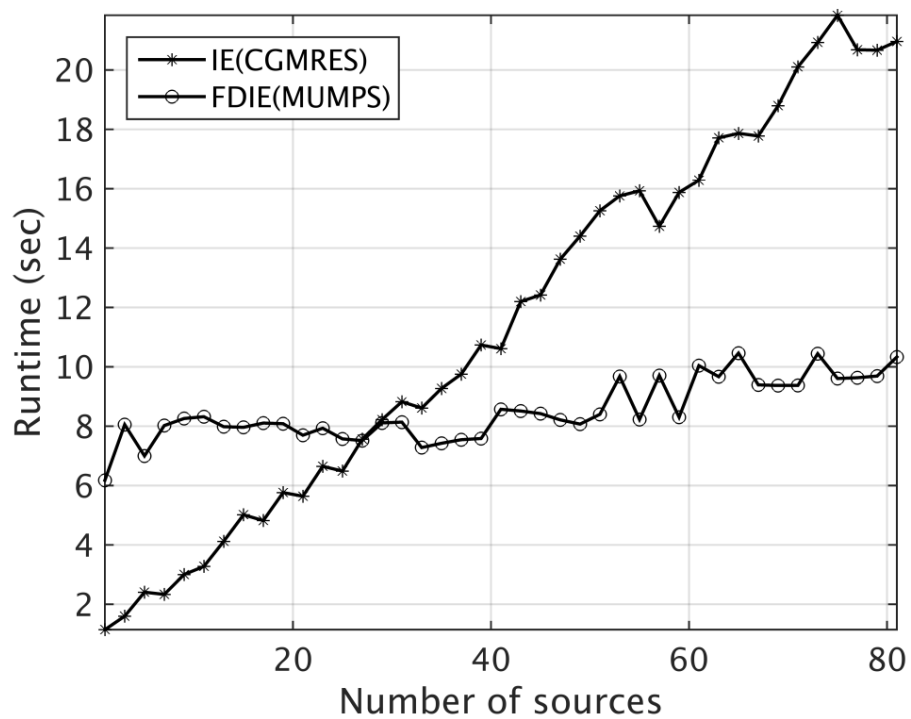


Figure 4.13. Model 2. Computation time of solving the corresponding systems of linear equations for the electric field within the anomalous domain for IE and hybrid FD-IE methods as a function of increasing number of the sources.

	Coarse grid			Fine grid		
	Time (s)	Relative error (%)		Time (s)	Relative error (%)	
FD	10.28	Ex	15.63	196.19	Ex	3.20
		Ey	15.28		Ey	1.40
		Ez	163.03		Ez	1.57
		Hx	6.47		Hx	2.52
		Hy	7.69		Hy	2.93
		Hz	13.21		Hz	0.76
Hybrid FD-IE	10.28 + 5.6	Ex	3.01	196.19 + 20.82	Ex	2.84
		Ey	1.59		Ey	0.83
		Ez	1.74		Ez	0.95
		Hx	2.02		Hx	0.83
		Hy	3.02		Hy	2.86
		Hz	0.19		Hz	0.21

Table 4.1. Model 1: computational times and relative errors of the FD and Hybrid FD-IE method for the horizontally layered model with coarse and fine grids.

CHAPTER 5

HYBRID FINITE DIFFERENCE AND INTEGRAL EQUATION METHOD FOR EM INVERSION

5.1 Introduction

I have introduced the hybrid finite-difference (FD) and integral equation (IE) modeling method in Chapter 4, which combines the advantages of the FD and the IE methods (Yoon et al., 2015). In this chapter, the developed hybrid algorithm was incorporated as the forward EM modeling engine in a general regularized inversion scheme, based on the reweighted conjugate gradient method. Direct computation of the Fréchet derivative is very time consuming, and at least one extra forward modeling is required to find it at every iteration. Also, the calculation of the Fréchet matrix requires very large computer memory for its storage. To avoid those problems, I calculate the Fréchet derivative matrix using a quasi-Born (QB) approximation (Gribenko and Zhdanov, 2007; Zhdanov, 2009) on the staggered grid, which does not require any extra forward modeling, and apply the concept of the moving sensitivity domain (MSD) approach (Cox and Zhdanov, 2007; Zhdanov et al., 2014a, 2014b), which can reduce the memory requirement for its storage.

There are four advantages of the developed inversion scheme. 1) The data predicted by the hybrid FD-IE method provide a more accurate solution than the conventional FD

method, even without the mesh refinement near the receiver and source positions. 2) The direct solver in the framework of hybrid FD-IE modeling method enables us to calculate the predicted data more efficiently than conventional IE method in the case of multisource data 3) The QB approximation enables us to calculate the Fréchet derivative matrix very efficiently without any extra forward modeling; the Green's tensors used for the EM field calculation in the forward modeling are reused for the Fréchet derivative calculation, so no extra computation of the Green's tensors is required. 4) The memory requirements for storing the intermediate forward modeling results and the Fréchet derivative matrix are reduced due to the application of the MSD approach.

Although the inversion algorithm is general, this paper presents an application of this method specifically to the 3D inversion of MCSEM data and Towed Streamer EM data. Model studies of the 3D inversion of synthetic MCSEM and Towed Streamer EM data are presented to demonstrate the effectiveness of the developed hybrid method. I have also applied the novel 3D inversion method to the MCSEM data collected in the Nordkapp Basin in Barents Sea and the Towed Streamer EM data collected by PGS in the Troll West Oil Province.

5.2 Inversion Methodology

I have implemented the developed hybrid FD-IE modeling method in the algorithm of inversion following the paper by Gribenko and Zhdanov (2007). The regularized inversion algorithm is based on minimization of the Tikhonov parametric functional, (Tikhonov and Arsenin, 1977; Zhdanov, 2002):

$$P(\Delta\sigma) = \|\mathbf{W}_d(\mathbf{A}_h(\Delta\sigma) - \mathbf{d})\|^2 + \alpha s(\Delta\sigma) = \min \quad (5.1)$$

where \mathbf{d} is the vector of the observed data; $\mathbf{A}_h(\Delta\sigma)$ is the forward modeling operator for computing the predicted data based on the hybrid FD-IE method; α is the regularization parameter; \mathbf{W}_d is the diagonal data weighting matrix formed by the inverse amplitudes of the background electric field. The first term of the parametric functional in equation 20 represents the weighted misfit functional, and the second term, $s(\Delta\sigma)$, is the stabilizer. There are several possible choices for the stabilizer such as minimum norm, minimum support, minimum gradient support, and minimum vertical support stabilizers (Portniaguine and Zhdanov, 1999; Zhdanov, 2002; Zhdanov et al., 2007). In numerical examples we use the minimum norm and the minimum vertical support stabilizing functionals.

I apply the regularized conjugate gradient (RCG) algorithm of the parametric functional minimization, summarized as follows (Zhdanov, 2002):

$$\begin{aligned} \mathbf{r}^{(n)} &= \mathbf{A}_h(\Delta\sigma^{(n)}) - \mathbf{d} \\ \mathbf{I}^{(n)} &= \mathbf{F}^{(n)*} \mathbf{W}_d^* \mathbf{W}_d \mathbf{r}^{(n)} + \alpha \mathbf{W}_m^* \mathbf{W}_m (\Delta\sigma^{(n)} - \Delta\sigma_{appr}) \\ \beta^{(n)} &= \|\mathbf{I}^{(n)}\|^2 / \|\mathbf{I}^{(n-1)}\|^2 \\ \tilde{\mathbf{I}}^{(n)} &= \mathbf{I}^{(n)} + \beta_n \tilde{\mathbf{I}}^{(n-1)}, \tilde{\mathbf{I}}^{(0)} = \mathbf{I}^{(0)}, \\ k^{(n)} &= (\tilde{\mathbf{I}}^{(n)}, \mathbf{I}^{(n)}) / \left(\|\mathbf{W}_d \mathbf{F}^{(n)} \tilde{\mathbf{I}}^{(n)}\|^2 + \alpha \|\mathbf{W}_m \tilde{\mathbf{I}}^{(n)}\|^2 \right) \\ \Delta\sigma^{(n+1)} &= \Delta\sigma^{(n)} - k^{(n)} \tilde{\mathbf{I}}^{(n)}, \end{aligned} \quad (5.2)$$

where $\mathbf{r}^{(n)}$ is a residual at the iteration step n , $\mathbf{I}^{(n)}$ is the gradient direction, $\tilde{\mathbf{I}}^{(n)}$ is the conjugate direction, $\mathbf{F}^{(n)}$ is a Fréchet derivative matrix, \mathbf{W}_d is a data weighting matrix,

α is a regularization parameter, $k^{(n)}$ is a length of the iteration step, and \mathbf{W}_m is the weighting matrix of the model parameters determined based on the weighted Fréchet derivative matrix (sensitivities):

$$\mathbf{W}_m = \text{diag}(\mathbf{F}^* \mathbf{W}_d^* \mathbf{W}_d \mathbf{F})^{1/4} \quad (5.3)$$

Direct computation of the Fréchet derivative is very time consuming, and at least one extra forward modeling is required to find it at every iteration. I calculate the Fréchet derivatives based on quasi-Born (QB) approximation (Gribenko and Zhdanov, 2007), which does not require any extra forward modeling, so that it results in a very efficient inversion method. Note that, in the inversion algorithm, the electric fields are computed by hybrid FD-IE modeling at the centers of the edges of the cells, whereas the model parameters are assigned to the centers of the cells. Therefore, I derive a discrete form of the QB approximation of the Fréchet derivatives on the edges of the cells of the staggered grid (see Appendix B). The advantage of computing the Fréchet derivatives on the staggered grid is that the Green's tensors I used in the field calculation are the same as those for the Fréchet calculation. Therefore, any extra computation of the Green's tensors for the Fréchet derivative computation is not required. The Green's tensors can be computed only once and are reused for the Fréchet and field calculations at every iteration of the inversion method.

Another difficulty in computing the Fréchet derivative matrix is related to the size of computer memory required for its storage. The size of the Fréchet derivative matrix is proportional to the number of EM data points times the number of the cells in the inversion domain. If the numbers of data points and cells in the inversion domain are

large, the computer memory requirements may exceed the available storage size. To reduce these requirements, I apply the moving sensitivity domain (MSD) approach to the inversion algorithm (Cox et al., 2010; Zhandov and Cox, 2012; Zhdanov et al., 2013, 2014a, 2014b).

In the framework of the MSD approach, for a given transmitter-receiver pair, the responses and Fréchet derivatives are computed from a subdomain that encapsulates the towed EM system's sensitivity domain. The Fréchet matrix for the entire inversion domain is then constructed as the superposition of the Fréchet derivatives from all transmitter-receiver pairs over the entire inverse model (Cox and Zhdanov, 2007; Zhdanov et al., 2014a, 2014b). This makes the originally dense matrix of the Fréchet derivative a sparse one. In this way, I can reduce the memory requirement for the Fréchet derivative calculation while retaining maximum accuracy.

5.3 Synthetic Model Study of the Inversion Algorithm

Based on the Hybrid FD-IE Method

5.3.1 Inversion of Synthetic MCSEM Data

To test the developed inversion algorithm, I have first considered a typical MCSEM survey with a salt dome structure within the sea-bottom sediments. Model 1 consists of a 300 m seawater layer with a resistivity of 0.3 Ohm-m, and a 10 Ohm-m half-space of sediments. A salt dome structure is embedded in the sediments, and it is located at a depth from 700 m below the sea floor down to 5000 m with a resistivity of 300 Ohm-m as shown in Figure 5.1. The synthetic in-line electric field data at frequencies of 1, 2, and 3 Hz were computed in 14 receivers from -7 km to 7 km in the x direction located 5 m

above the seafloor. The transmitter line was positioned 45 m above the receiver line from -17 km to 17 km in the x direction. The synthetic observed MCSEM data were generated using the 3D IE forward modeling code (Hursán and Zhdanov, 2002), and they were contaminated with random Gaussian noise having source-moment-normalized amplitude up to 10^{-14} V/Am².

The inversion domain was discretized using uniform rectangular grid with the cell size of 200 m x 500 m in the x and y directions, respectively. This grid has 30 layers in the z direction with the thickness logarithmically increasing from 20 m to 500 m down until 5000 m depth below the sea bottom. The FD modeling domain was designed by padding all sides of the inversion domain with 8 more layers logarithmically increasing in size, as shown in the top panel of Figure 5.2. The inversion was terminated when the weighted misfit reached to the noise level in the synthetic data. Figure 5.3 shows an example of the observed and predicted data at the misfit level. One can see that the predicted data fit the observed data pretty well even though the strong noise at the far offset in the observed data. Figure 5.3 presents the inversion result at the misfit level. As one can see, the upper part of the salt dome is very well recovered, but its bottom part cannot be recovered because the depth of the bottom (approximately 3000 m) is beyond the sensitivity of the data.

5.3.2 Inversion of Synthetic Towed Streamer EM Data

I have also applied the inversion algorithm to synthetic Towed Streamer EM data computer simulated for a typical sea-bottom geoelectrical model. Model 3 consists of two thin hydrocarbon reservoirs embedded in a conductive layer of the sea-bottom sediments

as shown in Figure 5.4. The bodies on the left- and right-hand sides in Figure 5.4 represent oil and gas reservoirs with resistivities of 50 ohm-m and 100 ohm-m, respectively. The background consists of a 320 m seawater layer with a resistivity of 0.3 ohm-m, and 1 ohm-m half-space representing the sea-bottom sediments. The oil and gas reservoirs are located 1100 m and 1200 m below the sea surface, with thicknesses of 200 m for both of them.

The synthetic observed Towed Streamer EM data were generated using the 3D IE forward modeling code (Hursán and Zhdanov, 2002). The EM survey consists of 5 survey lines running in the x direction, with distances of 1 km between the lines as shown in panel b of Figure 5.4. The electromagnetic field is excited at every 500 m by a horizontal electric dipole oriented in the x direction with a moment of 1 Am, which is towed at a depth of 10 m below the sea surface. Five receivers with offsets between 2400 m and 5400 m are towed at a depth of 100 m and measure inline electric fields at three frequencies between 0.1 and 2.75 Hz. The data were contaminated with random Gaussian noise of 2% of the total electric fields.

The dimension of the inversion domain is 18 km x 8 km x 1.6 km. The inversion domain is discretized into 250 m x 250 m x 100 m uniform cells, from a depth of 400 to 2000 m. The FD modeling domain was designed by padding all sides of the inversion domain with 4 more layers with logarithmically increasing size. The inversions were run on one node of a cluster with 20 Intel Xeon processors, 64 Gbytes, and 2.5 GHz, and it required a few hours until the misfit between the observed and predicted data reached the noise level of 2%. Figure 5.5 presents the inversion results. As one can see from the results, the inversion recovered well the shapes and depths of the reservoirs.

5.4 Inversion of Towed Streamer EM data Collected from the Troll West Oil Province

I have applied the 3D inversion based on the hybrid FD-IE method to Towed Streamer EM data collected in the Troll West Oil Province. The Troll field is located in the Norwegian sector in the northern part of the North Sea. The field is separated into three parts: The Troll West Oil Province (TWOP), the Troll West Gas Province (TWGP), and the Troll East Gas Province (TEGP). The Towed Streamer EM data were acquired by PGS over the Troll field in 2010 and 2012, and the data were inverted successfully based on the IE method (Zhdanov et al., 2014a, 2014b). In the current paper, I present the results of the isotropic inversion only using the data acquired in 2012. However, the hybrid FD-IE could be applied for an anisotropic inversion as well. For more information about the data, geological setting and exploration history, I refer the reader to Zhdanov et al. (2014a, 2014b).

The Towed Streamer EM data I inverted comprised seven lines of data at three frequencies between 0.1 and 1.04 Hz. The 8700 m long EM streamer with eleven receivers with offsets between 1860 and 7554 m was towed at 100 m depth. The EM source was towed at 10m depth. Figure 5.6 shows the survey configuration for the seven-line data over the true locations of the TWOP and TWGP in the local coordinate system. The inversion domain was selected from -16 km to 16 km, -4 km to 4 km, and 400 m to 2400 m in the x , y , and z directions. The inversion domain was discretized using a uniform grid with a cell size of 250 m x 250 m x 50 m. The starting model for the inversion consists of 320 m seawater with a resistivity of 0.27 ohm-m and a 2 ohm-m half-space. The inversion was run without any a priori information. The process of

iterative inversion was terminated after 49 iterations when the normalized misfit reached 2.5%. Figure 5.7 presents the inversion results at this misfit level. As one can see, the inversion results correlate very well with the true positions of the TWOP and TWGP reservoirs. Also, the recovered images agree well with those recovered by Zhdanov et al. (2014a).

5.5 Conclusions

I have developed an algorithm of 3D EM inversion based on the novel hybrid FD-IE modeling method introduced in Chapter 4. The implementation of the hybrid FD-IE modeling method to the inversion algorithm enables us to calculate the predicted data very accurately without mesh refinements near the receiver positions. Also, in order to make the inversion algorithm more efficient, I have applied two advanced techniques to the inversion algorithm. First, I have applied the Quasi-Born (QB) approximation on the staggered grid to calculate the Fréchet derivatives matrix. The QB approximation on the staggered grid enables us to calculate the Fréchet matrix using the precomputed Green's tensors for the hybrid FD-IE modeling method. Therefore, the Green's tensors are computed only once, and reused for the fields and the Fréchet calculations at every iteration of the inversion. Also, to reduce the memory requirements for the storage of the Fréchet matrix, the concept of the moving sensitivity domain approach has been applied to the inversion algorithm. The model studies and the case studies of MCSEM data and Towed Streamer EM data demonstrate the efficiency of the developed inversion algorithm.

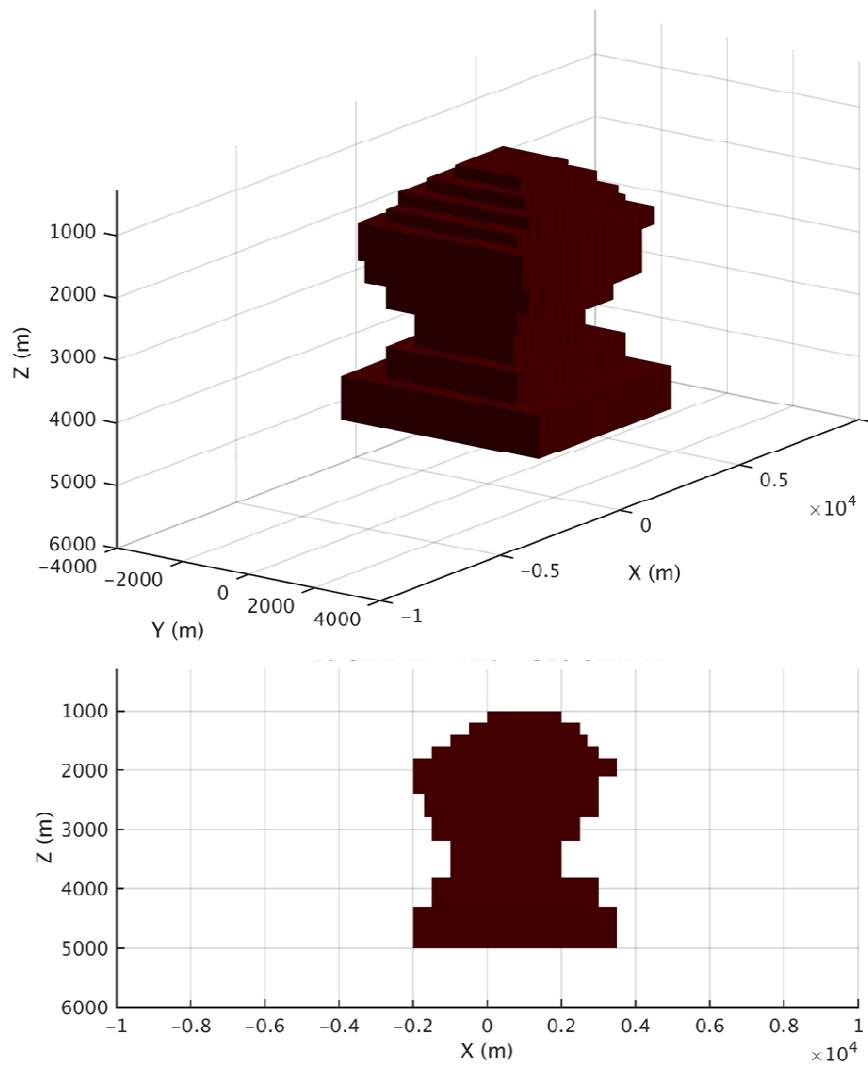


Figure 5.1. Model 1: a salt dome structure within the sea-bottom sediments. The top panel shows a 3D view of the model; the bottom panel presents a vertical section at $y = 0$ m.

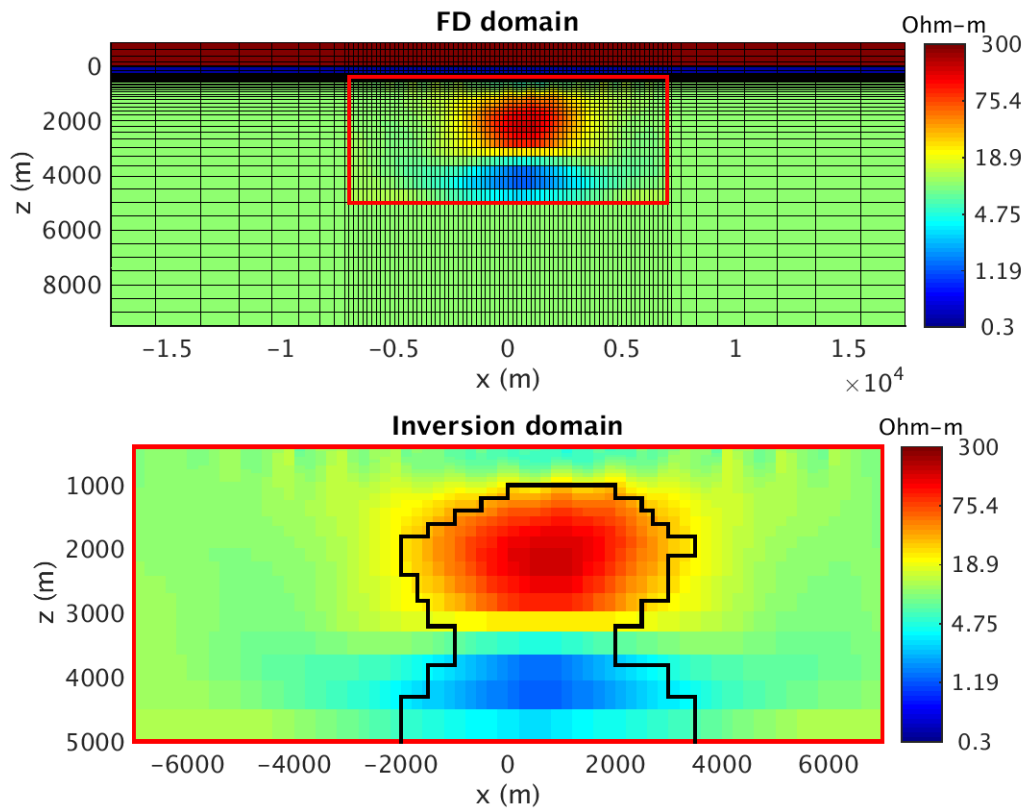


Figure 5.2. Model 1: the resistivity distribution recovered by the inversion of MCSEM data based on a salt dome model. The top panel shows the FD modeling domain and the corresponding discretization grid overlapped with the inversion result. The bottom panel shows the inversion result within the inversion domain only.

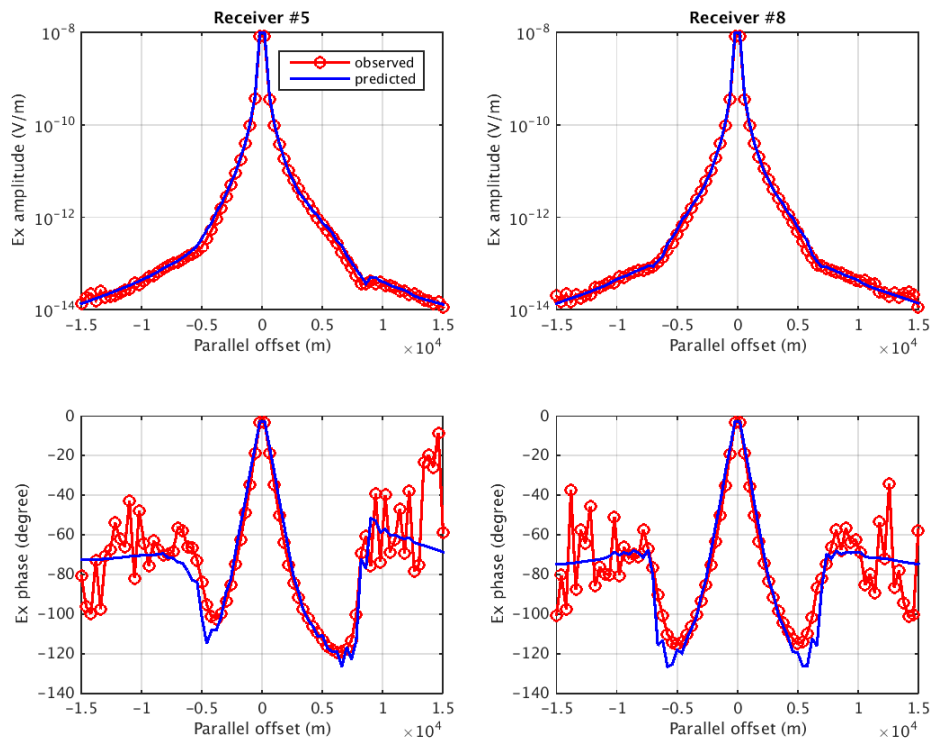


Figure 5.3. Model 1: examples of the data fit by the MCSEM inversion. The top panels present the AVO plots of in-line electric field data at a frequency of 0.2 Hz for receivers #5 (left) and #8 (right), respectively. The bottom panels show the corresponding PVO plots.

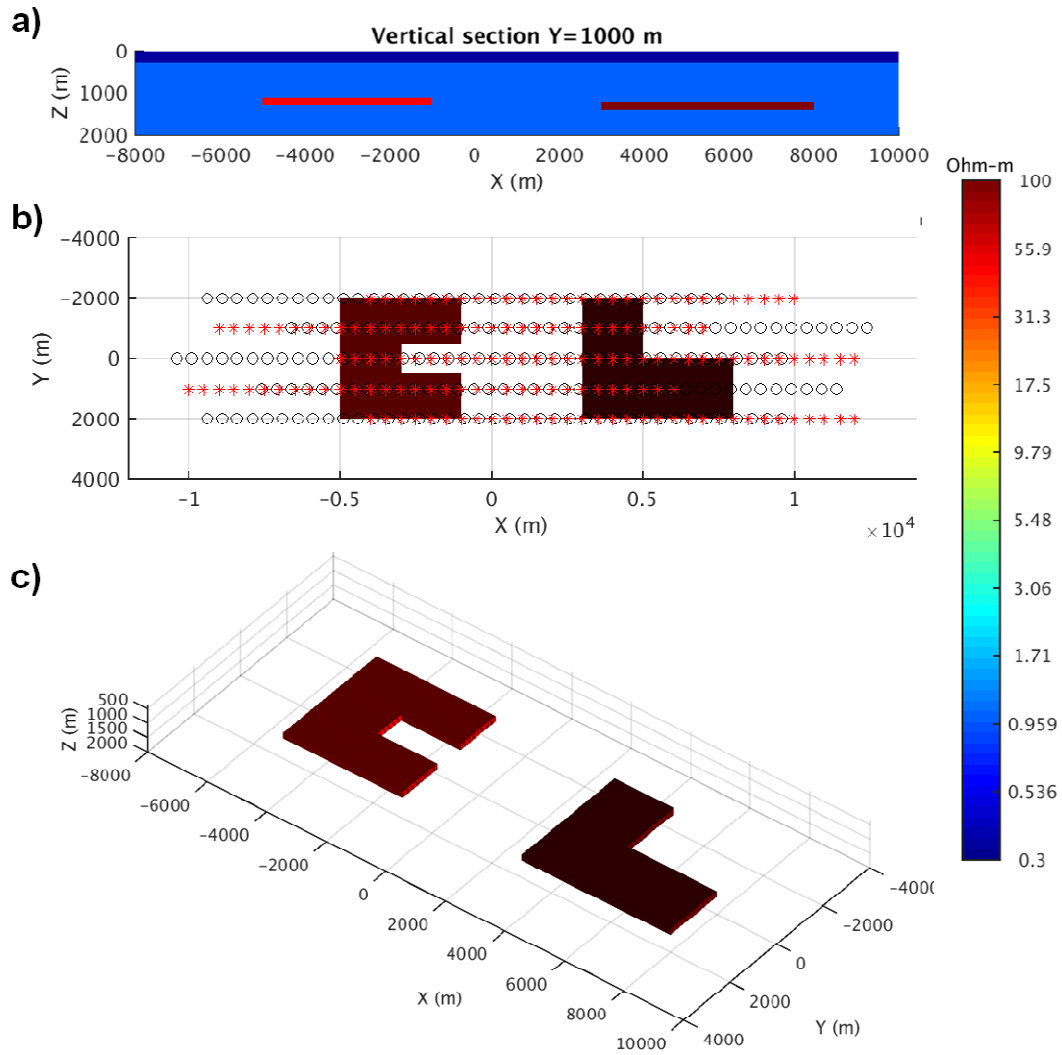


Figure 5.4. Model 3. (a) vertical section at $y=1000$ m, (b) top view with transmitter (star) and receiver (circle) positions, and (c) 3D resistivity distributions

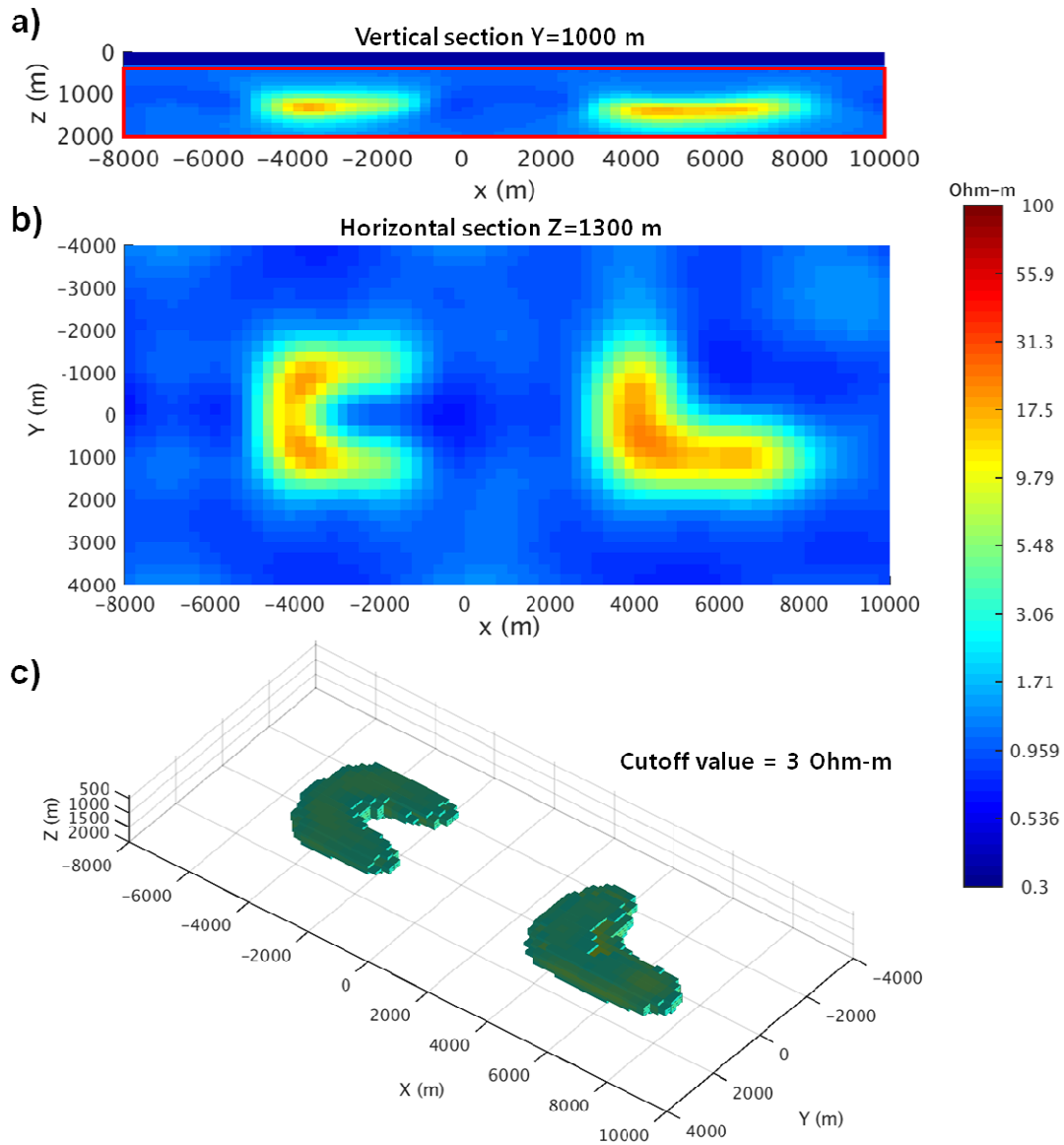


Figure 5.5. The resistivity distribution recovered by the inversion of the synthetic Towed Streamer EM data on Model 3. (a) vertical section at $y=1000$ m, (b) horizontal section at a depth of 1300 m, and (c) 3D resistivity distributions with a cutoff value of 3 ohm-m.

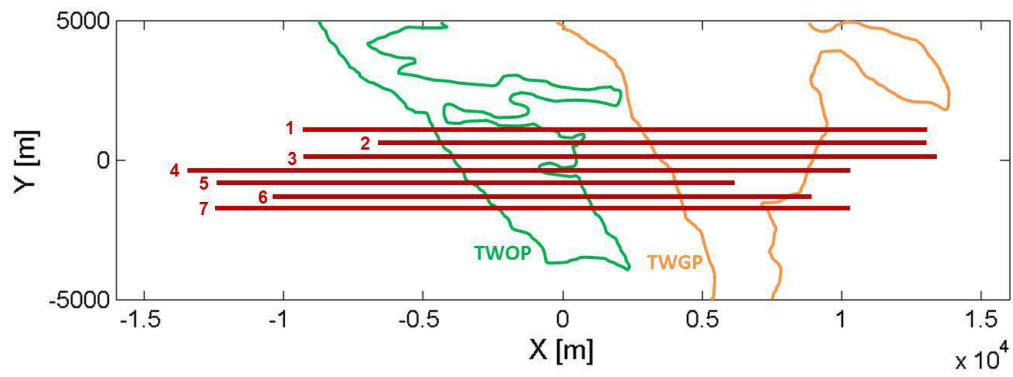


Figure 5.6. The survey configuration for seven-line data inversion in the local coordinate system.

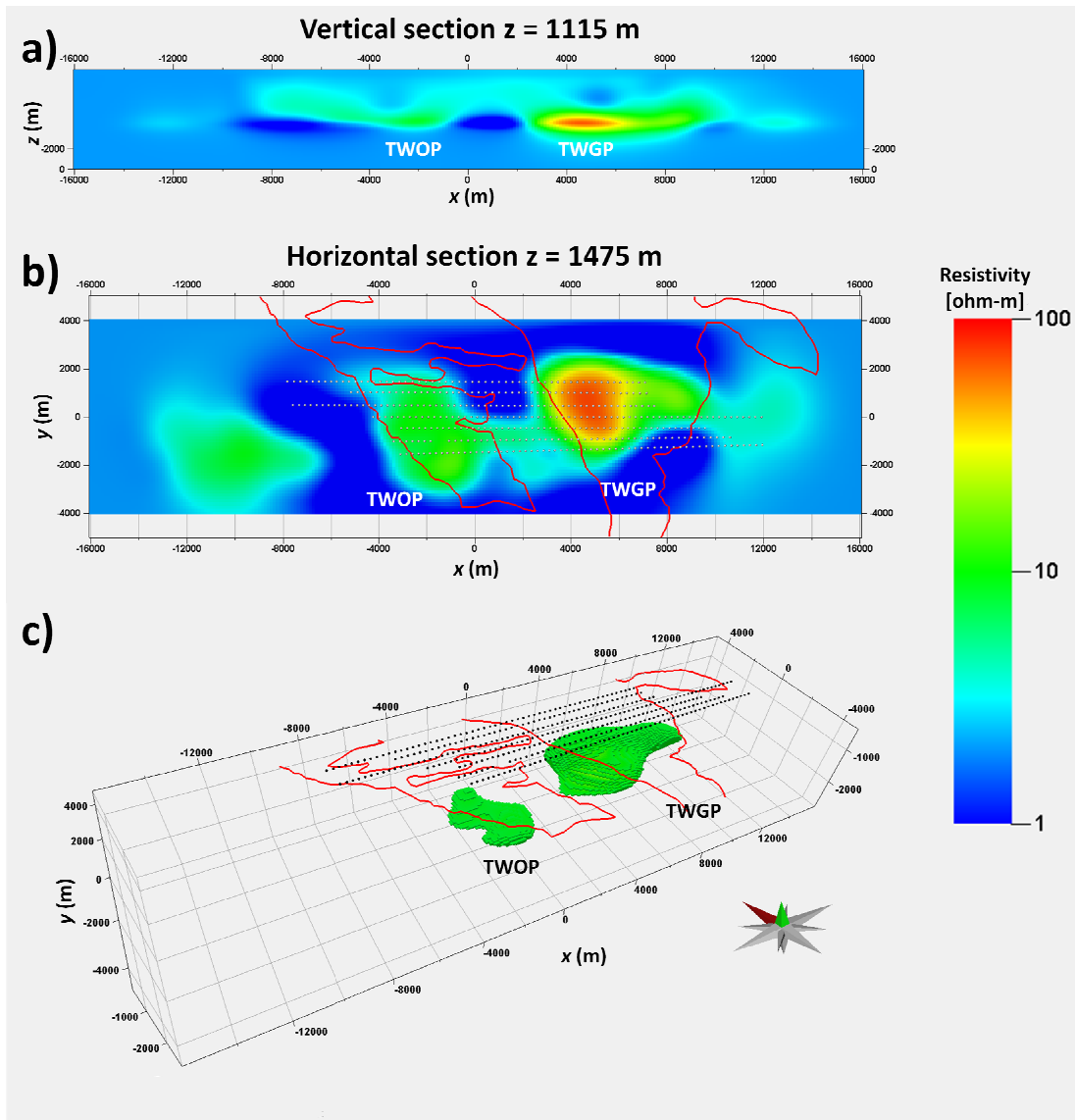


Figure 5.7. The resistivity distribution recovered by the inversion of the Towed Streamer EM data from Troll field. (a) vertical section at $y=1115$ m below the survey line 1, (b) horizontal section at a depth of 1475 m (white dots represent transmitter positions), and (c) 3D resistivity distributions with a cutoff value of 8 ohm-m.

CHAPTER 6

GENERAL CONCLUSIONS

As marine EM surveys have been extensively used for offshore exploration, the needs for efficient techniques to interpret the EM data have grown as well. There are two major types of marine EM surveys. One is aimed in conducting a reconnaissance study of the large survey area with the purpose of locating the prospective zones of hydrocarbons (HC) accumulation. Another type of the EM surveys is used for a detailed study of these prospective zones with the goal to determine a specific position of the potential HC reservoirs. In this dissertation, I introduce two new techniques for solving these two important problems — optimal synthetic aperture method for analysis of the reconnaissance surveys and a hybrid finite difference (FD) and integral equation (IE) method for rigorous 3D inversion of the EM data collected by exploration surveys. Those developed methods are applied to two different configurations of the marine EM surveys, which are widely used in industry. The first one is the conventional MCSEM survey, consisting of a set of fixed sea-bottom receivers and a towed electric bipole transmitter. Another one is the Towed Streamer EM survey, which involves a system of electric bipole transmitter and electric receivers towed behind the vessel at some depth.

In Chapter 2, I applied the optimal synthetic aperture method to the conventional MCSEM data. I demonstrated that the developed method could be used for increasing the

corresponding ratio between total and background fields within the area of an expected reservoir anomaly, as well as reducing the distorting airwave effect from the MCSEM data collected in shallow water. Scanning scheme with moving window was proposed for the practical application of the optimal synthetic aperture method to the MCSEM data. The proposed scheme enables us to detect the strongest electric anomaly, which can be associated with the HC prospective zones, over the survey area in a very efficient way. The optimal synthetic aperture method is expanded to the Towed Streamer EM data in Chapter 3. A case study of Towed Streamer EM data collected in the Troll field demonstrated that this method could be used for finding the horizontal locations of targets, mapping the strong anomalies over the target areas. The optimal synthetic aperture method was demonstrated being a very effective and efficient technique for analysis of the reconnaissance surveys to detect the prospective HC reservoirs, before applying time consuming EM inversion.

Once the strong EM anomaly has been detected over the survey area by the optimal synthetic aperture method, the EM inversion can be applied to produce a detailed geoelectrical image of the sea-bottom formations. 3D EM inversion is of utmost important method in practical applications because of the 3D nature of the geological structure. At the same time, however, this problem is very challenging because of large computational time and memory requirements. Especially, the forward modeling algorithms should be powerful and fast enough to be suitable for repeated use in tens or hundreds of iterations of the inversion. To this end, I developed a novel 3D EM modeling and inversion algorithms based on hybrid finite difference (FD) and integral equation (IE) method.

In Chapter 4, I introduced a 3D EM modeling algorithm based on hybrid FD-IE method, which combines the advantages of the conventional FD and IE methods. In the framework of the developed approach, the FD system is solved using a direct solver, MUMPS, and the electric and magnetic fields at the receiver positions are calculated using the Green's tensor approach. Numerical model studies demonstrated that the hybrid FD-IE provides more accurate solutions than the conventional FD method, even without mesh refinement near receiver positions, and faster solutions than the conventional IE method in the case of the multisource data such as MCSEM and Towed Streamer EM data.

In Chapter 5, I introduced a 3D EM inversion algorithm based on the developed hybrid FD-IE modeling method. In the inversion algorithm, the Fréchet derivative matrix is calculated based on Quasi-Born (QB) approximation on the staggered grid, which enables us to reuse the Green's tensors used for the EM fields calculation in the forward modeling. The Moving Sensitivity Domain (MSD) approach is also applied to reduce the memory requirements for storing the Fréchet derivative matrix. Those implementations make the inversion algorithm very powerful for inverting multisource data with a large number of cells. Synthetic model studies and case study using Towed Streamer EM data collected by PGS over the Troll field in the North Sea demonstrated the accuracy and the efficiency of the developed inversion algorithm.

The practical use of the developed two techniques is well demonstrated by numerical model studies and case studies. However, there are still several aspects not considered in this dissertation. The first one is related to the bathymetry or topography effects. In the numerical and case studies for the developed techniques, I assumed flat bathymetry. If

the effect of the bathymetry is strong, one should take into account the bathymetry to reduce the false anomaly caused by it.

Second, the developed techniques can be applied to other types of the EM surveys. For example, marine electromagnetic remote-sensing (MEMRS) survey is designed for EM exploration in the near-shore zones, and consists of onshore electric bipole source and a large array of offshore receivers (Yoon and Zhdanov, 2013). Interpreting the MEMRS data is challenging because of weak and distorted EM responses from the target, which caused by relatively large offsets between onshore transmitter and offshore receivers as well as distorting airwave effect in the shallow water environment (tens of meters). Those problems could be overcome by applying the optimal synthetic aperture method to MEMRS data, constructing a virtual source with a combination of different sources onshore to steer the generated EM fields toward the target direction. The developed hybrid FD-IE method is general, so it can be applied to any other EM surveys.

Another important aspect not considered in this thesis is multiple frequencies for the optimal synthetic aperture method. Considering the fact that frequency is related to the skin depth of electromagnetic fields, the application of the optimal synthetic aperture method for different frequency could provide a valuable information of the target depth and optimal frequency range for EM inversion. Alternatively, one can solve the synthetic aperture method with respect to the EM responses from multiple frequencies, instead of multiple sources. In this way, depth resolution could be obtained instead of the lateral resolution enhanced by the optimal synthetic aperture method in this thesis.

Last one is the application of the synthetic aperture weights to the EM inversion. In Chapter 2, it has been demonstrated that the synthetic aperture weights can be

mathematically described as the data weighting. By replacing the conventional data weights in the EM inversion algorithm to the synthetic aperture weights, one could see how the synthetic aperture affects to the results of the EM inversion. To fully understand the impact of the synthetic aperture on EM inversion, the optimal synthetic aperture weights should be applied to the developed inversion algorithm in future.

APPENDIX A

WEIGHTED AVERAGING CONDUCTIVITY AND THE CORRESPONDING VOLUME

In the staggered grid scheme, the anomalous electric fields are assigned to the edges of the cells. The conductivities where the electric fields are located are represented by a weighted average of conductivities of the four adjoining cells based on Ampere's law (Wang and Hohmann, 1993; Alumbaugh et al., 1996).

For example, the x-directional conductivity, $\Delta\sigma_{x(i,j-1/2,k-1/2)}$, located at the edge-center is averaged by the areas of the four adjoining cells (see panels a and b of Figure A.1) as follows:

$$\Delta\sigma_{x(i,j-1/2,k-1/2)} = \frac{\Delta\sigma_{x(i,j,k)}A_{(i,j,k)} + \Delta\sigma_{x(i,j-1,k)}A_{(i,j-1,k)} + \Delta\sigma_{x(i,j,k-1)}A_{(i,j,k-1)} + \Delta\sigma_{x(i,j-1,k-1)}A_{(i,j-1,k-1)}}{A_{(i,j,k)} + A_{(i,j-1,k)} + A_{(i,j,k-1)} + A_{(i,j-1,k-1)}}. \quad (\text{A.1})$$

The volume for the corresponding imaginary cell with respect to the averaged conductivity, $\Delta\sigma_{x(i,j-1/2,k-1/2)}$, is calculated (see panel c of Figure A.1) as follows:

$$v_{(i,j-1/2,k-1/2)} = \left(A_{(i,j,k)} + A_{(i,j-1,k)} + A_{(i,j,k-1)} + A_{(i,j-1,k-1)} \right) \cdot \Delta x_i. \quad (\text{A.2})$$

where Δx_i is the length of the corresponding edge, which determines the dimension of the cell in the x direction. Similar considerations are valid for the y and z components of the average conductivities and the corresponding volumes. This volume of the imaginary cell is used to solve the volume integral of the Green's function in equation (4.19) based on the Gaussian quadrature method.

APPENDIX B

CALCULATION OF FRÉCHET DERIVATIVES

To derive the Fréchet derivatives based on the QB approximation on the staggered grid, I start with a discrete form of the equation (4.12) at inversion iteration (n) as follows:

$$\begin{aligned}
 E_{\alpha}^{a(n)}(r_l) &= \sum_{i=1}^{N_x} \sum_{j=1}^{N_y+1} \sum_{k=1}^{N_z+1} \Gamma_{\alpha x}^{l(i,j-1/2,k-1/2)} \Delta\sigma_{x(i,j-1/2,k-1/2)}^{(n)} E_{x(i,j-1/2,k-1/2)}^{(n)} \\
 &+ \sum_{i=1}^{N_x+1} \sum_{j=1}^{N_y} \sum_{k=1}^{N_z+1} \Gamma_{\alpha y}^{l(i-1/2,j,k-1/2)} \Delta\sigma_{y(i-1/2,j,k-1/2)}^{(n)} E_{y(i-1/2,j,k-1/2)}^{(n)} \\
 &+ \sum_{i=1}^{N_x+1} \sum_{j=1}^{N_y+1} \sum_{k=1}^{N_z} \Gamma_{\alpha z}^{l(i-1/2,j-1/2,k)} \Delta\sigma_{z(i-1/2,j-1/2,k)}^{(n)} E_{z(i-1/2,j-1/2,k)}^{(n)}. \tag{B.1}
 \end{aligned}$$

where $E_{\alpha}^{a(n)}(r_l)$ is the α component of a predicted anomalous electric field at the receiver position; r_l , $\Delta\sigma_{\beta}^{(n)}$ and $E_{\beta}^{(n)}$ are anomalous conductivity and electric fields in the β direction within the inversion domain on the staggered grid.

By substituting equation (A.1) into equation (B.1), one can find the Fréchet derivatives based on QB approximation with respect to the β directional conductivity, $\Delta\sigma_{\beta}$. For example, the Fréchet derivative of the α component of the electric fields, receiver position, r_l , and n iteration with respect to the x directional conductivity,

$\Delta\sigma_{x(i,j,k)}^{(n)}$ is

$$\begin{aligned}
\mathbf{F}_{\alpha}^{(n)}(r_l) \big|_{\Delta\sigma_{x(i,j,k)}} = \mathbf{F}_{\alpha x}^{(n)}(r_l) &= \frac{A_{(i,j,k)} \Gamma_{\alpha x}^{l(i,j-1/2,k-1/2)} \mathbf{E}_{x(i,j-1/2,k-1/2)}^{(n)}}{A_{(i,j,k)} + A_{(i,j-1,k)} + A_{(i,j,k-1)} + A_{(i,j-1,k-1)}} \\
&+ \frac{A_{(i,j,k)} \Gamma_{\alpha x}^{l(i,j+1/2,k-1/2)} \mathbf{E}_{x(i,j+1/2,k-1/2)}^{(n)}}{A_{(i,j,k)} + A_{(i,j+1,k)} + A_{(i,j,k-1)} + A_{(i,j+1,k-1)}} \\
&+ \frac{A_{(i,j,k)} \Gamma_{\alpha x}^{l(i,j-1/2,k+1/2)} \mathbf{E}_{x(i,j-1/2,k+1/2)}^{(n)}}{A_{(i,j,k)} + A_{(i,j-1,k)} + A_{(i,j,k+1)} + A_{(i,j-1,k+1)}} \\
&+ \frac{A_{(i,j,k)} \Gamma_{\alpha x}^{l(i,j+1/2,k+1/2)} \mathbf{E}_{x(i,j+1/2,k+1/2)}^{(n)}}{A_{(i,j,k)} + A_{(i,j+1,k)} + A_{(i,j,k+1)} + A_{(i,j+1,k+1)}}.
\end{aligned} \tag{B.2}$$

In the case of a cell-center based grid such as in the IE method, the Fréchet derivative based on QB approximation with respect to $\Delta\sigma_{x(i,j,k)}^{(n)}$ can be represented as follows:

$$\mathbf{F}_{\alpha}^{(n)}(r_l) \big|_{\Delta\sigma_{x(i,j,k)}} = \Gamma_{\alpha x}^{l(i,j,k)} \mathbf{E}_{x(i,j,k)}^{(n)}. \tag{B.3}$$

Comparing equations (B.2) and (B.3), one can see that the Fréchet derivative at a point (i,j,k) is a weighted average of the Fréchet derivatives at the four points of the edge-centers of the cell (i,j,k) . The Fréchet derivatives with respect to the y and z directional conductivity can be derived in a similar way.

In matrix notation, equation (B.2) can be generalized as follows:

$$\mathbf{F}_{\beta}^{(n)} = \mathbf{F}^{(n)} \big|_{\Delta\sigma_{\beta}} = \hat{\mathbf{G}}_{\beta}^{\mathbf{E}} \mathbf{E}_{\beta}^{(n)} \mathbf{C}_{\beta} = \begin{bmatrix} \mathbf{G}_{x\beta}^{\mathbf{E}} \\ \mathbf{G}_{y\beta}^{\mathbf{E}} \\ \mathbf{G}_{z\beta}^{\mathbf{E}} \end{bmatrix} \mathbf{E}_{\beta}^{(n)} \mathbf{C}_{\beta} \tag{B.4}$$

where $\mathbf{F}_\beta^{(n)}$ is a $3L \times N$ matrix of the Fréchet derivatives with respect to the β directional conductivity, $\Delta\sigma_\beta$, $\widehat{\mathbf{G}}_\beta^{\text{E}}$ is a $3L \times N_\beta^{\text{c}}$ matrix containing electric Green's tensor integrals with respect to the β directional conductivity; $\mathbf{E}_\beta^{(n)}$ is a $N_\beta^{\text{c}} \times N_\beta^{\text{c}}$ diagonal matrix with β components of the electric fields; and \mathbf{C}_β is a $N_\beta^{\text{c}} \times N$ weighted averaging matrix. For representation purposes, I introduce the weighted averaging matrix, \mathbf{C}_β , but the actual calculation of the weighted average of $\widehat{\mathbf{G}}_\beta^{\text{E}} \mathbf{E}_\beta^{(n)}$ can be easily made in a 3D matrix array.

In the case of isotropy, the Fréchet matrix can be represented as

$$\mathbf{F}^{(n)} \big|_{\Delta\sigma} = \begin{bmatrix} \mathbf{G}_{xx}^{\text{E}} \\ \mathbf{G}_{yx}^{\text{E}} \\ \mathbf{G}_{zx}^{\text{E}} \end{bmatrix} \mathbf{E}_x^{(n)} \mathbf{C}_x + \begin{bmatrix} \mathbf{G}_{xy}^{\text{E}} \\ \mathbf{G}_{yy}^{\text{E}} \\ \mathbf{G}_{zy}^{\text{E}} \end{bmatrix} \mathbf{E}_y^{(n)} \mathbf{C}_y + \begin{bmatrix} \mathbf{G}_{xz}^{\text{E}} \\ \mathbf{G}_{yz}^{\text{E}} \\ \mathbf{G}_{zz}^{\text{E}} \end{bmatrix} \mathbf{E}_z^{(n)} \mathbf{C}_z = \mathbf{F}_x^{(n)} + \mathbf{F}_y^{(n)} + \mathbf{F}_z^{(n)}. \quad (\text{B.5})$$

The Fréchet derivatives for the magnetic field can be found by replacing the electric Green's tensors in equation (B.5) with the magnetic Green's tensors.

As one can see, the Green's tensors used for field calculations in equation (B.1) are the same as those used for Fréchet calculation in equation (B.2). Therefore, one can precompute the Green's tensors on the staggered grid only once, and reuse them for the Fréchet calculation as well as the field calculation, which results in a very efficient inversion method.

REFERENCES

Alumbaugh, D. L., G. A. Newman, L. Prevost, and J. N. Shadid, 1996, Three-dimensional wideband electromagnetic modeling on massively parallel computers: *Radio Science*, **31**, no. 1, 1-23, doi: 10.1029/95RS02815.

Amestoy, P. R., I. S. Duff, J.-Y. L'Excellent, and J. Koster, 2001, A fully asynchronous multifrontal solver using distributed dynamic scheduling: *SIAM Journal on Matrix Analysis and Applications*, **23**, no. 1, 15-41, doi: 10.1137/S0895479899358194.

Amestoy, P. R., A. Guermouche, J.-Y. L'Excellent, and S. Pralet, 2006, Hybrid scheduling for the parallel solution of linear systems: *Parallel Computing*, **32**, no. 2, 136-156, doi: 10.1016/j.parco.2005.07.004.

Amundsen, L., L. Løseth, R. Mittet, S. Ellingsrud, and B. Ursin, 2006, Decomposition of electromagnetic fields into upgoing and downgoing components: *Geophysics*, **71**, no. 5, G211-G223.

Anderson, C., and J. Mattsson, 2010, An integrated approach to marine electromagnetic surveying using a towed streamer and source: *First Break*, **28**, no. 5, 71-75

Andreis, D., and L. MacGregor, 2007, Controlled-source electromagnetic sounding in shallow water: Principles and applications: *Geophysics*, **73**, no. 1, F21-F32.

Avdeev, D., and S. Knizhnik, 2009, 3D integral equation modeling with a linear dependence on dimensions: *Geophysics*, **74**, no. 5, F89-F94, doi: 10.1190/1.3190132.

Avdeev, D. B., 2005, Three-dimensional electromagnetic modelling and inversion from theory to application: *Surveys in Geophysics*, **26**, no. 6, 767-799.

Cetin, M., and W. C. Karl, 2001, Feature-enhanced synthetic aperture radar image formation based on nonquadratic regularization: *IEEE Transactions on Image Processing*, **10**, no. 4, 623-631.

Cheney, M., 2001, A mathematical tutorial on synthetic aperture radar: *SIAM review*, **43**, no. 2, 301-312.

Chung, Y., J. S. Son, T. J. Lee, H. J. Kim, and C. Shin, 2014, Three-dimensional

modelling of controlled-source electromagnetic surveys using an edge finite-element method with a direct solver: *Geophysical Prospecting*, **62**, no. 6, 1468-1483, doi: 10.1111/1365-2478.12132.

Constable, S., and C. J. Weiss, 2006, Mapping thin resistors and hydrocarbons with marine EM methods: Insights from 1D modeling: *Geophysics*, **71**, no. 2, G43-G51.

Constable, S., 2010, Ten years of marine CSEM for hydrocarbon exploration: *Geophysics*, **75**, no. 5, 75A67-75A81, doi: 10.1190/1.3483451.

Cox, C. S., 1981, On the electrical conductivity of the oceanic lithosphere: *Physics of the Earth and Planetary Interiors*, **25**, no. 3, 196-201.

Cox, L. H., and M. S. Zhdanov, 2007, Large-scale 3D inversion of HEM data using a moving footprint: 77th Annual International Meeting, SEG, Expanded Abstracts.

Cox, L. H., G. A. Wilson, and M. S. Zhdanov, 2010, 3D inversion of airborne electromagnetic data using a moving footprint: *Exploration Geophysics*, **41**, no. 4, 250-259.

da Silva, N. V., J. V. Morgan, L. MacGregor, and M. Warner, 2012, A finite element multifrontal method for 3D CSEM modeling in the frequency domain: *Geophysics*, **77**, no. 2, E101-E115, doi: 10.1190/geo2010-0398.1.

DeGraaf, S. R., 1998, SAR imaging via modern 2-D spectral estimation methods: *IEEE Transactions on Image Processing*, **7**, no. 5, 729-761.

Ellingsrud, S., T. Eidesmo, S. Johansen, M. Sinha, L. MacGregor, and S. Constable, 2002, Remote sensing of hydrocarbon layers by seabed logging (SBL): Results from a cruise offshore Angola: *The Leading Edge*, **21**, no. 10, 972-982.

Endo, M., M. Čuma, and M. S. Zhdanov, 2008, A multigrid integral equation method for large-scale models with inhomogeneous backgrounds: *Journal of Geophysics and Engineering*, **5**, no. 4, 438, doi: 10.1088/1742-2132/5/4/007.

Engelmark, F., J. Mattsson, and J. Linfoot, 2012, Marine CSEM with A Novel Towed Acquisition System: PGCE 2012.

Fan, Y., R. Snieder, E. Slob, J. Hunziker, J. Singer, J. Sheiman, and M. Rosenquist, 2010, Synthetic aperture controlled source electromagnetics: *Geophysical Research Letters*, **37**, no. 13, L13305, doi: 10.1029/2010GL043981.

Fan, Y., R. Snieder, E. Slob, J. Hunziker, J. Singer, J. Sheiman, and M. Rosenquist, 2012, Increasing the sensitivity of controlled-source electromagnetics with synthetic aperture: *Geophysics*, **77**, no. 2, E135-E145, doi: 10.1190/geo2011-0102.1.

Filloux, J., 1967, An ocean bottom, D component magnetometer: *Geophysics*, **32**, no. 6, 978-987.

Grayver, A., R. Streich, and O. Ritter, 2013, Three-dimensional parallel distributed inversion of CSEM data using a direct forward solver: *Geophysical Journal International*, **193**, no. 3, 1432-1446, doi: 10.1093/gji/ggt055.

Gribenko, A., and M. S. Zhdanov, 2007, Rigorous 3D inversion of marine CSEM data based on the integral equation method: *Geophysics*, **72**, no. 2, WA73-WA84, doi: 10.1190/1.2435712.

Hesthammer, J., A. Stefatos, M. Boulaenko, S. Fanavoll, and J. Danielsen, 2010, CSEM performance in light of well results: *The Leading Edge*, **29**, no. 1, 34-41.

Hokstad, K., B. Fotland, G. Mackenzie, V. Antonsdottir, S. K. Foss, C. Stadtler, C. Fichler, M. Haverl, B. M. T. Waagan, E. A. Myrlund, L. Masnaghetti, F. Ceci, and P. Y. Raya. 2011, Joint imaging of geophysical data: Case history from the Nordkapp Basin, Barents Sea, 81th Annual International Meeting, SEG, Expanded Abstracts. 1098-1102.

Holten, T., E. G. Flekkøy, B. Singer, E. M. Blixt, A. Hanssen, and K. Måløy, 2009, Vertical source, vertical receiver, electromagnetic technique for offshore hydrocarbon exploration: *First Break*, **27**, no. 5.

Hursán, G., and M. S. Zhdanov, 2002, Contraction integral equation method in three-dimensional electromagnetic modeling: *Radio Science*, **37**, no. 6, 1089, doi: 10.1029/2001ES002513.

Jaysaval, P., D. Shantsev, and S. de la Kethulle de Ryhove, 2014, Fast multimodel finite-difference controlled-source electromagnetic simulations based on a Schur complement approach: *Geophysics*, **79**, no. 6, E315-E327, doi: 10.1190/geo2014-0043.1.

Kaputerko, A., A. Gribenko, and M. S. Zhdanov, 2007, Sensitivity analysis of marine CSEM surveys: Society of Exploration Geophysicists Annual Meeting. 77th, Society of Exploration Geophysicists. doi: 10.1190/1.2792493.

Knaak, A., R. Snieder, Y. Fan, and D. Ramirez-Mejia, 2013, 3D synthetic aperture and steering for controlled-source electromagnetics: *The Leading Edge*, **32**, no. 8, 972-978, doi: 10.1190/tle32080972.1.

Korobov, A. I., M. Y. Izosimova, and S. A. Toschov, 2010, Development of ultrasound focusing discrete array for air-coupled ultrasound generation: *Physics Procedia*, **3**, no. 1, 201-207.

MacGregor, L., and J. Tomlinson, 2014, Marine controlled-source electromagnetic methods in the hydrocarbon industry: A tutorial on method and practice: *Interpretation*, **2**, no. 3, SH13-SH32.

Mattsson, J., P. Lindqvist, R. Juhasz, and E. Björnemo, 2012, Noise reduction and error analysis for a towed EM system: 82th Annual International Meeting, SEG, Expanded Abstracts.

Mckay, A., J. Mattson, and Z. Du, 2015, Towed Streamer EM—reliable recovery of sub-surface resistivity: *First Break*, **33**, no. 4, 75-85.

Newman, G. A., and D. L. Alumbaugh, 1995, Frequency-domain modelling of airborne electromagnetic responses using staggered finite differences: *Geophysical Prospecting*, **43**, no. 8, 1021-1042.

Novysh, V., and G. Fonarev, 1966, The results of the electromagnetic study in the Arctic Ocean: *Geomagnetizm i Aèronomia*, **6**, no., 406-409.

Portniaguine, O., and M. S. Zhdanov, 1999, Focusing geophysical inversion images: *Geophysics*, **64**, no. 3, 874-887.

Schwarzbach, C., and E. Haber, 2013, Finite element based inversion for time-harmonic electromagnetic problems: *Geophysical Journal International*, **193**, no. 2, 615-634, doi: 10.1093/gji/ggt006.

Soumekh, M. 1999, Synthetic aperture radar signal processing: New York: Wiley.

Stadtler, C., C. Fichler, K. Hokstad, E. A. Myrlund, S. Wienecke, and B. Fotland, 2014, Improved salt imaging in a basin context by high resolution potential field data: Nordkapp Basin, Barents Sea: *Geophysical Prospecting*, **62**, no. 3, 615-630.

Streich, R., 2009, 3D finite-difference frequency-domain modeling of controlled-source electromagnetic data: Direct solution and optimization for high accuracy: *Geophysics*, **74**, no. 5, F95-F105, doi: 10.1190/1.3196241.

Tikhonov, A. N., and V. I. A. k. Arsenin. 1977, Solutions of ill-posed problems: Vh Winston.

Trofimov, I., and G. Fonarev. 1972, Some Results of Magnetotelluric Profiling in the Arctic Ocean: National Technical Information Service.

Um, E. S., and D. L. Alumbaugh, 2007, On the physics of the marine controlled-source electromagnetic method: *Geophysics*, **72**, no. 2, WA13-WA26.

Wang, T., and G. W. Hohmann, 1993, A finite-difference, time-domain solution for three-dimensional electromagnetic modeling: *Geophysics*, **58**, no. 6, 797-809, doi: 10.1190/1.1443465.

Ward, S. H., and G. W. Hohmann, 1988, Electromagnetic theory for geophysical applications: *Electromagnetic Methods in Applied Geophysics*, **1**, no., 131-311.

Yang, D., and D. W. Oldenburg, 2012, Three-dimensional inversion of airborne time-domain electromagnetic data with applications to a porphyry deposit: *Geophysics*, **77**, no. 2, B23-B34, doi: 10.1190/geo2011-0194.1.

Yee, K. S., 1966, Numerical solution of initial boundary value problems involving Maxwell's equations in isotropic media: *IEEE Trans. Antennas Propagation*, **14**, no. 3, 302-307, doi: 10.1109/TAP.1966.1138693.

Yoon, D., and M. S. Zhdanov, 2011, Controlled sensitivities for marine CSEM surveys: 81th Annual International Meeting, SEG, Expanded Abstracts.

Yoon, D., and M. S. Zhdanov, 2013, Feasibility Study of the Marine Electromagnetic Remote Sensing (MEMRS) Method for Near-Shore Exploration: 83th Annual International Meeting, SEG, Expanded Abstracts.

Yoon, D., and M. S. Zhdanov, 2014, An optimal synthetic aperture method for the creation of directional sensitivity and removal of the airwave effect in MCSEM data: 84th Annual International Meeting, SEG, Expanded Abstracts.

Yoon, D., and M. S. Zhdanov, 2015, Optimal Synthetic Aperture Method for Marine Controlled-Source EM Surveys: *IEEE Geoscience and Remote Sensing Letters*, **12**, no. 2, 414-418.

Yoon, D., M. S. Zhdanov, H. Cai, and A. Gribenko. 2015, A hybrid finite difference and integral equation method for modeling and inversion of marine CSEM data, 85th Annual International Meeting, SEG, Expanded Abstracts. 823-827.

Yuan, J., and R. Edwards, 2000, The assessment of marine gas hydrates through electrical remote sounding: hydrate without a BSR?: *Geophysical Research Letters*, **27**, no. 16, 2397-2400.

Zhdanov, M. S., and L. H. Cox. 2012, Method of subsurface imaging using superposition of sensor sensitivities from geophysical data acquisition systems. U. S. Patent US20130173163 A1.

Zhdanov, M. S. 2015, *Inverse theory and applications in geophysics*: Elsevier.

Zhdanov, M. S., C. Anderson, M. Endo, L. Cox, M. Čuma, G. Wilson, N. Black, and A. Gribenko, 2012, 3D inversion of towed streamer EM data: A model study of the Harding field with comparison to CSEM: *First Break*, **30**, no. 4, 71-74.

Zhdanov, M. S., and G. V. Keller. 1994, *The geoelectrical methods in geophysical exploration*: Elsevier.

Zhdanov, M. S. 2002, *Geophysical inverse theory and regularization problems*: Elsevier.

Zhdanov, M. S., S. K. Lee, and K. Yoshioka, 2006, Integral equation method for 3D modeling of electromagnetic fields in complex structures with inhomogeneous background conductivity: *Geophysics*, **71**, no. 6, G333-G345, doi: 10.1190/1.2358403.

Zhdanov, M. S., A. Gribenko, and M. Cuma, 2007, Regularized focusing inversion of marine CSEM data using minimum vertical support stabilizer: *77th Annual International Meeting, SEG, Expanded Abstracts*.

Zhdanov, M. S. 2009, *Geophysical electromagnetic theory and methods*: Elsevier.

Zhdanov, M. S., 2010, Electromagnetic geophysics: Notes from the past and the road ahead: *Geophysics*, **75**, no. 5, 75A49-75A66.

Zhdanov, M. S., 2013, Focusing controlled sensitivity of geophysical data: *Journal of Geology & Geosciences*, **10**, no., 2.

Zhdanov, M. S., L. Cox, and J. Rudd, 2013, Paradigm change in 3D inversion of airborne EM surveys: case study for oil sands exploration near Fort McMurray, Alberta: *First Break*, **31**, no. 4.

Zhdanov, M. S., M. Endo, L. H. Cox, M. Čuma, J. Linfoot, C. Anderson, N. Black, and A. V. Gribenko, 2014a, Three-dimensional inversion of towed streamer electromagnetic data: *Geophysical Prospecting*, **62**, no. 3, 552-572, doi: 10.1111/1365-2478.12097.

Zhdanov, M. S., M. Endo, D. Yoon, M. Čuma, J. Mattsson, and J. Midgley, 2014b, Anisotropic 3D inversion of towed-streamer electromagnetic data: Case study from the Troll West Oil Province: *Interpretation*, **2**, no. 3, SH97-SH113, doi: 10.1190/INT-2013-0156.1.

Ziolkowski, A., R. Parr, D. Wright, V. Nockles, C. Limond, E. Morris, and J. Linfoot, 2010, Multi-transient electromagnetic repeatability experiment over the North Sea Harding field: *Geophysical Prospecting*, **58**, no. 6, 1159-1176.